# Ordered Mesoporous Materials as Model Supports to Study Catalyst Preparation

Jelle R.A. Sietsma

ISBN 978-90-393-4660-0

Drukkerij Ponsen & Looijen, Wageningen

# Ordered Mesoporous Materials as Model Supports to Study Catalyst Preparation

Geordend mesoporeuze materialen als modeldragers voor het bestuderen van katalysatorbereiding

(met een samenvatting in het Nederlands)

Proefschrift

ter verkrijging van de graad van doctor aan de Universiteit Utrecht op gezag van de rector magnificus, prof. dr. W.H. Gispen, ingevolge het besluit van het college voor promoties in het openbaar te verdedigen op maandag 24 september 2007 des middags te 4.15 uur

door

Jelle Rudolf Anne Sietsma

geboren op 14 juni 1978 te Laren

Promotor: Prof. Dr. Ir. K.P. de Jong
Faculteit Bètawetenschappen, Departement Scheikunde,
Universiteit Utrecht

Co-promotor: Dr. P.E. de Jongh
Faculteit Bètawetenschappen, Departement Scheikunde,
Universiteit Utrecht

# Contents

# 1

# General introduction

## Catalysis

In 1835, Jöns Jakob Berzelius was the first to rationalise a series of isolated observations of several researchers by the concept of a 'catalytic power' and, he defined substances that by 'their mere presence evoke chemical reactions that would not otherwise take place' as catalysts.[1,2]

Since that time catalysts have become indispensable to our society as they are used for the production of fuels and chemicals, and the reduction of environmental pollution. World-wide catalyst sales in 2005 were estimated at US$ 11 billion, however, their economical impact is much higher because of their central role in petroleum refining and, bulk and fine chemical processing.[3] It has been estimated that about 80% of all the processes in the chemical industry rely on the application of one or more catalysts. In the United States of America for instance, about one-third of the Gross Domestic Product (GDP) that is generated involves a catalytic process somewhere along the production chain.[4] In 2006, this concurred with an excess of US$ 4300 billion in goods and services, which accounted for about 7% of the world-wide GDP.[5,6] Also within the Netherlands, catalysis is economically important as a contribution of the chemical sector to the Dutch GDP of no less than 10% has been estimated.[7]

Catalysts can be divided into three classes, that of biocatalysts, homogeneous catalysts and heterogeneous catalysts. The latter category of catalysts is active in processes where the catalyst resides in a phase different from that of the reactants and products. These catalysts are most abundantly used in industry and typically comprise of supported metal (oxide) particles. Since catalytic processes take place at the metal (oxide) surface, high surface-to-volume ratios are often important for the catalysts efficiency and hence, much research is devoted to master the processes that control the final metal (oxide) particle size.

## Impregnation and drying

Commercial catalysts are typically shaped into extrudates, spheres or pellets to meet the technical requirements of pressure drop and mechanical strength necessary for application. The specific shape and size of the catalyst body depends on the application and type of reactor used. As support material typically metal oxides such as $SiO_2$ and $Al_2O_3$ are used because of their stability at high temperatures. Usually, the catalysts are prepared by impregnation of the pre-shaped support body with a precursor-containing solution, followed by drying.[8-10] The volume of precursor solution impregnated generally equals the pore volume of the support and, therefore, is referred to as incipient wetness, pore volume or dry impregnation. Subsequently, the dried impregnate is given thermal treatment in air, called calcination, to convert the precursor into the desired metal oxide, optionally followed by high-temperature reduction to obtain the metal in question. The final dispersion and distribution

over the support of the active phase is largely affected by the type of precursor and support used, and the experimental conditions of the treatments applied during each successive step in the preparation.

Upon impregnation, precursor solution is readily absorbed by the support body due to capillary forces. However, the rate at which the precursor complex is distributed throughout the support body depends on its interaction with the support.[11-14] When interaction is relatively weak like for instance between a silica support and $[Ni(OH_2)_6]^{2+}$ complexes in a nickel nitrate solution with a pH of ~2, the complex is transported rapidly into the support body, and a homogeneous distribution is obtained. However, when nickel is introduced using a solution containing $[Ni(NH_3)_6]^{2+}$ complexes and with a pH of ~8, interaction is much stronger and transport of the complex can be slowed down, resulting in a non-uniform concentration profile over the silica support body. When the system is not allowed to equilibrate completely in the latter case, the inhomogeneous distribution can be retained upon drying and further treatments, resulting in a so-called egg-shell distribution of the active component over the catalyst body. This type of distribution is advantageous for processes that display diffusion limitations as the active phase is located near the periphery of the catalyst body. Besides egg-shell and uniform distributions other types such as egg-yolk and egg-white can be obtained.[9,12] Recently, Bergwerff *et al.*[15] demonstrated the large impact that the impregnation and ageing steps can have on the final distribution by probing precursor complex distributions real-time with spectroscopy techniques such as Raman[16] and Uv-Vis[17] microspectroscopy.

When relatively weak precursor-support interactions are present and sufficient equilibration time is allowed, it might be expected that the final distribution of the active component of the final catalyst is uniform. However, more often than not this is not the case due to redistribution processes that occur during drying and subsequent activation treatments. In particular the drying step is often assigned as being most detrimental to the final distribution over the catalyst body. Several models have been developed that describe the physico-chemical processes that take place during drying.[12,18-21] Evaporation of the solvent during drying starts with evaporation from the largest pores present at the external surface of the support body. The smaller pores at the periphery remain filled and form the evaporation front as they are replenished with solution from larger pores present in the interior of the support body. Hence, an outward convective flow is developed that enables transfer of precursor complexes on a microscopic scale (1 - 2000 μm) to the periphery of the support body, resulting in precursor precipitation when these domains become supersaturated. Due to the concentration gradient of the precursor complex over the support body, the convective flow is accompanied by back-diffusion of precursor complex towards the center of the support body. Transport of solution to the periphery continues until isolated patches form inside the support body. Consequently, the liquid-linked system breaks up and isolated domains are formed that dry independently. Hence, redistribution of precursor during drying over large distances due to the convective flow takes place only as long as the filled pores are

connected to the evaporation front at the periphery.

Redistribution due to convective flow is reduced when the catalyst support consists of agglomerated clusters of particles with pores much smaller than those present between the clusters. Powders fulfil these conditions as they consist of primary particles that are agglomerated into secondary particles with sizes usually varying from 1 to 100 μm. The pores formed by the voids between the primary particles typically range from 2 to 150 nm and hence are much smaller than the interstitial pores between the secondary particles. On the left-hand side of Figure 1 a Transmission Electron Microscopy (TEM) image is shown of a silica gel powder support. The image shows the aggregated structure of the primary particles of about 10 to 30 nm that form the secondary particles. Upon drying of an impregnated powder, any solution present in the large voids between the secondary particles will evaporate rapidly and consequently, the secondary particles dry independently limiting redistribution of precursor complex to within these domains. Hence, with powders the impact of redistribution during drying can be limited, which makes it possible to focus the impact of precursor migration on a mesoscopic scale (1 - 1000 nm) during the following activation treatments to obtain the the final catalyst.

Information on the size and distribution of the metal (oxide) or its precursor over powder supports can be obtained from electron microscopy. In particular TEM is a powerful technique for characterisation as it can give direct information on the distribution and particle size distribution. In Figure 2, two TEM images are shown of a conventional silica gel powder that was impregnated with an aqueous $[Ni(OH_2)_6](NO_3)_2$ solution followed by drying (left) and subsequent calcination in air (right) to yield NiO on silica at a loading of 28 wt%.

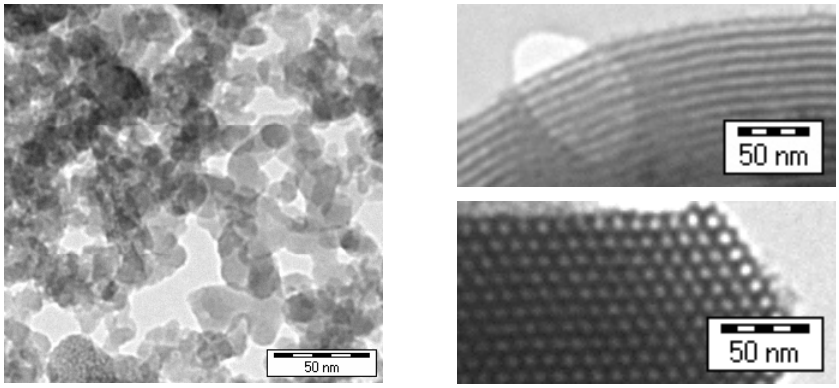


*Figure 1.* TEM images of conventional silica gel powder showing the primary particles of the support (left) and of ordered mesoporous material SBA-15 (right) showing the straight pores when viewed edge-on (top-right) and showing the hexagonal arrangement of the pores when viewed on-top (bottom-right).

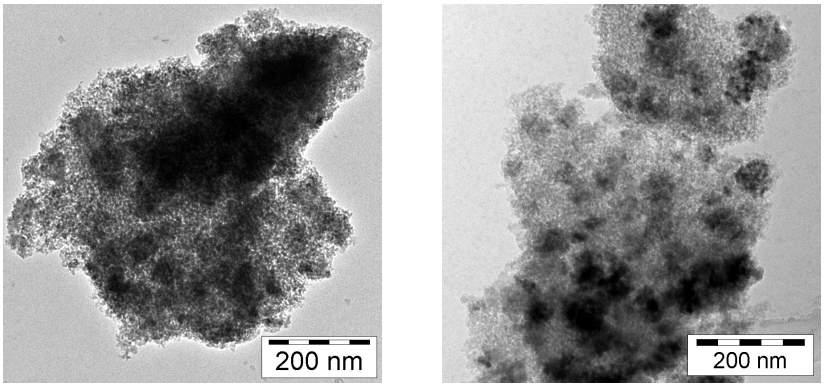


*Figure 2.* TEM images of a conventional silica gel powder that was impregnated with aqueous $[Ni(OH_2)_6](NO_3)_2$ solution followed by drying at 120 °C (left) and after subsequent calcination in air at 450 °C (right) to yield 28 wt% $NiO/SiO_2$.

The two images demonstrate that it is cumbersome to derive detailed information on the impact of each step on possible precursor redistribution due to the heterogeneity of the silica gel support. Better differentiation between precursor and support could improve identification of the impact of preparation treatments on the precursor phase when the support displays an ordered mesopore structure. These support materials are at hand since the discovery of ordered mesoporous supports.[22-25] Example TEM images of an ordered mesoporous support named SBA-15 (*vide infra*) have been given in the right-frame of Figure 1. They display the straight pores of the support particles when viewed edge-on and the hexagonal arrangement of the pores when viewed on-top. Comparison of these images with the TEM image of silica gel shown in the left-frame suggests the beneficial effect that ordered mesoporous materials may have on identifying the location of the active phase or its precursor. Especially, combination of ordered supports with electron tomography, sometimes referred to as 3D-TEM, can yield valuable information is as this technique allows three-dimensional imaging of the interior of porous structures.[26-28] Hence, the limitations of TEM that always shows a two-dimensional projection of the three-dimensional structure are overcome. Furthermore, the uniform pore system enables one to derive more detailed information from $N_2$-physisorption experiments. Particle growth inside the mesoporous channels during preparation can be monitored as the degree of (partial) pore blocking by these guest phase particles is displayed in the desorption branch of the isotherm.[28-30] Hence, we decided to employ ordered mesoporous support materials as model support systems to gain fundamental insight into the preparation of supported metal (oxide) catalysts by the impregnation and drying method.

## Ordered mesoporous supports

In 1992 researchers of the Mobil Oil Corporation discovered that ordered mesoporous silicas could be obtained using ionic surfactants as structure directing agents.[22-25] These materials were categorised as M41S materials and consisted of MCM-41, short for Mobil Composition of Matter No. 41, MCM-48 and MCM-50. In particular the former got much attention because of its relatively robust synthesis and hexagonally arranged unidimensional pores. It was soon identified by researchers working in the field of catalysis that the well-defined pores adjustable from 2 to 10 nm in diameter opened up many opportunities for new applications.[31-33] Next to the well-defined ordered structure that may provide uniform active sites with well-controlled steric effects[34,35], the high surface area of MCM-41 (~1,000 $m^2.g^{-1}$) offers the possibility to obtain high catalyst loadings. Unfortunately, the (hydro)thermal stability of the material showed to be relatively poor due to the thin amorphous pore walls of MCM-41 of about 0.5 to 1.5 nm. Methods were published to increase the hydrothermal stability[36,37], but these improvements were modest compared to the breakthrough in 1998 brought about by Zhao and co-workers.[38,39] These researchers obtained ordered mesoporous silicas labelled SBA-15, short for Santa Barbara No. 15, that contained pore walls with a thickness of 3 to 7 nm, hence resulting in a much higher (hydro)thermal stability than that of MCM-41. As a result, SBA-15 is usually preferred over MCM-41 when stability of the support is important. For this reason, the research described in this thesis was primarily conducted using SBA-15. Similar to MCM-41, the pores of SBA-15 are arranged in a honeycomb-like structure. The pore diameters are adjustable between about 6 to 15 nm depending on the synthesis temperature and type of structure directing agent used. Because copolymers are used as template, the pore walls are microporous and, hence the mesopores are connected contrary to those of MCM-41.[40] Although researchers recently claimed synthesis routes to obtain alumina-based ordered mesoporous supports[41], currently high-quality materials can only be obtained with silica.

Besides the attractive higher (hydro)thermal stability of SBA-15 for application as catalyst support material, the connectivity between the mesopores of SBA-15 opened up possibilities to obtain negative replica structures using the support as a hard template and hence this has become an important area of research too. The research groups of Ryoo, Schüth, Zhao and Davidson have significantly contributed to the development of techniques that allow preparation of carbon-based ordered mesoporous supports[42,43] and metal[44] or metal oxide[45-48] nanowires. The latter studies on obtaining nanowires by complete filling of SBA-15 with a metal (oxide) precursor have also yielded valuable insight into phenomena associated with the preparation of ordered mesoporous supported metal (oxide) catalysts. An example of this is the non-uniform distribution of metal (oxide) particles over pores that is often observed. Impéror-Clerc *et al.* reported for the preparation of $MnO_2$ that up to 97% of the mesopore volume could be filled when a 'two solvent' impregnation technique was used instead of incipient wetness impregnation.[48]

**Scope and outline of this thesis**

Aim of the research described in this thesis focussed on increasing the understanding of how the individual steps in the preparation of catalysts affect the final distribution of the active component and its performance during catalysis. To this end ordered mesoporous materials were used as model support systems. As a case study, we focussed on the preparation of Ni and Co-based catalysts by the impregnation and drying method with metal nitrate precursors. These metals and precursor salts were chosen as Ni and Co are amongst the most abundantly used metals in catalysis. They play, amongst others, an important role in food industry as catalyst for the hydrogenation of edible oils[50] and the Fischer-Tropsch synthesis of hydrocarbons from synthesis gas[51]. Nitrate salts highly soluble in water were selected since pure metals at high loadings can be obtained with these precursors, but unfortunately often only with poor metal dispersions.[52,55]

In **chapter 2** phenomena of impregnation and drying of ordered mesoporous supports with aqueous nickel nitrate solution were investigated. Using cryo-STEM it was shown that many pores were not filled after incipient wetness impregnation and remaining solution was present outside the mesopores. After drying $Ni_3(NO_3)_2(OH)_4$ precursor was exclusively found inside the pores, which could be explained by transport of precursor at the exterior surface into the filled pores during drying, resulting in a higher loading than anticipated. It was shown that filling of virtually all the pores could be accomplished by applying more than twice the volume of solution than that of the pore volume of the support. In **chapter 3** the impact of the gas atmosphere during thermal treatment of the dried impregnate usually applied to decompose the nickel nitrate precursor into NiO was studied using again SBA-15 as model support system. It was shown that during the air calcination step severe sintering and redistribution of precursor took place, resulting in large NiO particles outside and rod-like NiO particles inside the mesopores. Sintering and redistribution were favoured by a high local concentration of the $NO_2/O_2$ gaseous decomposition products and hence maintaining low concentrations of $NO_2/O_2$ was advocated. It was demonstrated that formation of $NO_2/O_2$ could be prevented by carrying out the thermal treatment in $H_2$, and small NiO particles of 3 nm were obtained. It was argued that the role of $H_2$ is related to its moderating effect on the decomposition of $Ni_3(NO_3)_2(OH)_4$ and consequently the type of gaseous products formed rather than direct reduction of the nitrate into Ni metal. In **chapter 4** a novel heat treatment in NO/He of dried SBA-15 supported nitrate precursor was presented that allowed preparation of NiO and $Co_3O_4$ particles that displayed high dispersions (3 to 5 nm particles) at loadings of 24 to 37 wt% and 16 to 23 wt%, respectively. Using conventional silica gel powder and carbon nanofibers as support the validity of this method for other systems was investigated. Moreover, it was shown that the final metal (oxide) crystal size depended on the amount of NO used and applied gas-hourly-space-velocity. Finally, using catalytic results of the hydrogenation of Soybean oil over $Ni/SiO_2$ catalysts prepared by NO/He treatment or traditional

air calcination, the relevance of the NO treatment for catalysis was discussed. In **chapter 5** the study on how NO affects the thermal decomposition to form small NiO particles from SBA-15 supported $Ni_3(NO_3)_2(OH)_4$ was presented. Firstly, it was demonstrated that combining electron tomography with bulk $N_2$-physisorption and XRD characterisation provided structural insight into the NiO size and distribution inside the mesopores as a function of the gas atmosphere. Secondly, the impact of air, He and NO/He gas atmospheres on the thermal decomposition was discussed. It was demonstrated that NO moderated the decomposition rate proceeded much slower than in air. It was proposed that the role of NO on the decomposition rate involves scavenging of oxygen radicals. In **chapter 6** the impact of air, $H_2$/He or NO/He gas atmosphere used during thermal decomposition of silica supported cobalt nitrate impregnate to obtain the $Co_3O_4$ phase on the final activity of the Co metal (18 wt%) in the Fischer-Tropsch synthesis was discussed. It was shown that the activity of the NO/He treated catalysts was superior compared to the catalysts treated with air of $H_2$/He atmospheres. However, the activity of the former largely depended on the applied reduction temperature and an explanation for this behaviour was presented. In **chapter 7** the results of our study on the immobilisation of functionalised homogeneous PCP and SCS-pincer Pd catalysts on SBA-15 and MCM-41 were presented. It was shown that the complexes could be tethered to the support via a trialkoxysilane moiety without destruction of the ordered mesoporous support. The activity of the SBA-15 modified with PCP-pincer Pd-complex as Lewis acid in the aldol condensation between methyl isocyanoacetate and benzaldehyde was discussed together with recycling results that showed the true heterogeneous nature of the catalyst in this reaction. Finally, in **chapter 8** the main conclusions derived from the previous chapters were summarised together with some concluding remarks.

**References**


1. Berzelius, J.J. *Jahresberichte* **1835**, *15*, 237.
2. Roberts, M.W. *Catal. Lett.* **2000**, *67*, 1-17.
3. Naber, J.E.; De Jong, K.P.; Stork, W.H.J.; Kuipers, H.P.C.E.; Post, M.F.M. *Stud. Surf. Sci. Catal.* **1994**, *84*, 2197.
4. Baker, R.T. in: *Energy and Transportation: Challenges for the Chemical Sciences in the 21st Century*, National Research Council **2003**, chapter 12, 70.
5. International Monetary Fund, *World Economic Outlook Database* April **2007**.
6. U.S. Department of Commerce, Bureaus of Economic Analysis, *GDP news release* April **2007**.
7. Regiegroep Chemie, *Businessplan*, ed. A. Piersma, July **2006**.
8. Bourikas, K.; Kordulis, C.; Lycourghiotis, A. *Catal. Rev.* **2006**, *48*, 363-444.

9 Van Santen, R.A.; Van Leeuwen, P.W.N.M.; Moulijn, J.A.; Averill, B.A. (ed.), *Catalysis: An Integrated Approach, Second, Revised and Enlarged Edition*, Elsevier, Amsterdam **1999**.

10. Ertl, G.; Knözinger, H.; Weitkamp, J. *Preparation of solid catalysts* Weinheim, Germany, Wiley-VCH **1999**.

11. Clause, O.; Kermarec, M.; Bonnevoit, L.; Villain, F.; Che, M. *J. Am. Chem. Soc.* **1992**, *114*, 4709-4717.

12. Neimark, A.V.; Kheifez, L.I.; Fenelonov, V.B. *Ind. Eng. Chem. Prod. Res. Dev.* **1981**, *20*, 439-450.

13. Mang, T.; Breitscheidel, B.; Polanek, P.; Knözinger, H. *Appl. Catal. A: General* **1993**, *106*, 239-258.

14. Galarraga, C.; Peluso, E.; De Lasa, H. Chem. Eng. J. 2001, 82, 13-20.

15. Bergwerff, J.A. *Spatially Resolved Spectroscopy on the Preparation of $CoMo/Al_2O_3$ Hydrodesulphurization Catalysts*, PhD Thesis, Utrecht University, **2007**.

16. Bergwerff, J.A.; Visser, T.; Leliveld, B.R.G.; Rossenaar, B.D.; De Jong, K.P.; Weckhuysen, B.M. *J. Am. Chem. Soc.* **2004**, *126*, 14548-14556.

17. Van de Water, L.G.A.; Bergwerff, J.A.; Nijhuis, T.A.; De Jong, K.P.; Weckhuysen, B.M. *J. Am. Chem. Soc.* **2005**, *127*, 5024-5025.

18. Lekhal, A.; Glasser, B.J.; Khinast, J.G. *Chem. Eng. Sci.* **2001**, *56*, 4473-4487.

19. Lekhal, A.; Glasser, B.J.; Khinast, J.G. *Chem. Eng. Sci.* **2004**, *59*, 1063-1077.

20. Knijff, L.M. *The Application of Active Components into Catalyst Support Bodies*, PhD Thesis, Utrecht University, **1993**.

21. Van Den Brink, P.J. *The Selective Oxidation of Hydrogen Sulfide to Elemental Sulfur on Supported Iron-Based Catalysts*, PhD Thesis, Utrecht University, **1992**.

22. Kresge, C. T.; Leonowicz, M. E.; Roth, W. J.; Vartuli. J. C.; Beck, J. S. *Nature* **1992**, *359*, 710-712.

23. Beck, J.S.; Vartuli, J.C.; Roth, W.J.; Leonowicz, M.E.; Kresge, C.T.; Schmitt, K.D.; Chu, C.T- W.; Olson, D.H.; Sheppard, E.W.; McCullen, S.B.; Higgins, J.B.; Schlenker, J.L. *J. Am. Chem. Soc.* **1992**, *114*, 10834-10843.

24. Beck, J.S. U.S. Patent No. 5,057,296 **1991**.

25. Kresge, C.T.; Leonowicz, M.E.; Roth, W.J.; Vartuli, J.C. U.S. Patent No. 5,098,689 **1992**.

26. Koster, A. J.; Ziese, U.; Verkleij, A. J.; Janssen, A. H.; De Jong, K. P. *J. Phys. Chem. B.* **2000**, *104*, 9368-9370.

27. Ziese, U.; De Jong, K.P.; Koster, A.J. *Appl. Catal. A: General* **2004**, *260*, 71.

28. Janssen, A.H.; Yang, C.-M.;Wang, Y.; Schüth, F.; Koster, A.J.; De Jong, K.P. *J. Phys. Chem B* **2003**, *107*, 10552-10556.

29. Van der Voort, P.; Ravikovitch, P.I.; De Jong, K.P.; Benjeloun, M.; Van Bavel, E.; Janssen, A.H.; Neimark, A.V.; Weckhuysen, B.M.; Vansant, E.F. *J. Phys. Chem. B* **2002**, *106*, 5873-5877.

30. Vradman, L.; Landau, M.V.; Kantorovich, D.; Koltypin, Y.; Gedanken, A. *Micropor. Mesopor. Mater.* **2005**, *79*, 307 – 318.
31. Corma, A. *Chem. Rev.* **1997**, *97*, 2373-2419.
32. Ciesla, U.; Schüth, F. *Micropor. Mesopor. Mater.* **1999**, *27*, 131-149.
33. Taguchi, A.; Schüth, F. *Micropor. Mesopor. Mater.* **2005**, *77*, 1-45.
34. Maschmeyer, T., Rey, F., Sankar, G., Thomas, J. M., *Nature* **1995**, 378, 159-162.
35. Maschmeyer, T. *Curr. Opin. Solid State Mater. Sci.* **1998**, *3*, 71-78.
36. Kim, J.M.; Kwak, J.H.; Jun, S.; Ryoo, R. *J. Phys. Chem.* **1995**, *99*, 16742-16747.
37. Ryoo, R.; Jun, S. *J. Phys. Chem. B* **1997**, *101*, 317-320.
38. Zhao, D.; Feng, J.; Huo, Q.; Melosh, N.; Fredrickson, G. H.; Chmelka, B. F.; Stucky, G. D. *Science* **1998**, *279*, 548-552.
39. Zhao, D.; Feng, J.; Huo, Q.; Feng, J.; Bradley, F.; Chmelka, B. F.; Stucky, G.D. *J. Am. Chem. Soc.* **1998**, *120*, 6024-6036.
40 Impéror-Clerc, M.; Davidson, P.; Davidson, A. *J. Am. Chem. Soc.* **2000**, *122*, 11925-11933.
41. Niesz, K.; Yang, P.; Somorjai, G.A. *Chem. Commun.* **2005**, 1986-1987.
42. R. Ryoo,R.; Joo, S.H.; Jun, S. *J. Phys. Chem. B* **1999**, *103*, 7743-7746.
43. Lu, A-H.; Li, W-C.; Schmidt, W.; Schüth, F. *Micropor. Mesopor. Mater.* **2005**, *80*, 117-128.
44. Attard, G.S.; Corker, J.M.; Göltner, C.G.; Henkde, S.; Templer, R.H. *Angew. Chem. Int. Ed.* **1997**, *36*, 315-317.
45. Rumplecker, A.; Kleitz, F.; Salabas, E-L.; Schüth, F. *Chem. Mater.* **2007**, *19*, 485-496.
46. Tian, B.; Liu, X.; Yang, H.; Xie, S.; Yu, C.; Tu, B.; Zhao, D. *Adv. Mater.* **2003**, *15*, 1370-1374.
47. Tian, B.; Liu, X.; Solovyov, L.A.; Liu, Z.; Yang, H.; Zhang, Z.; Xie, S.; Zhang, F.; Tu, B.; Yu, C.; Terasaki, O.; Zhao, D. *J. Am. Chem. Soc.* **2004**, *126*, 865-875.
48. Impéror-Clerc, M.; Bazin, D.; Appay, M-D. ; Beaunier, P.; Davidson, A. *Chem. Mater.* **2004**, *16*, 1813-1821.
49. Moreno, S.M.; Weyland, M.; Midgley, P.A.; Bengoa, J.F.; Cagnoli, M.V.; Gallegos,N.G.; Alvarez, A.M.; Marchetti, S.G. *Micron* **2006**, *37*, 52-56.
50. Balakos, M. W.; Hernandez, E.E. *Catal. Today* **1997**, *35*, 415-425.
51. Iglesia, E. *Appl.Catal. A* **1997**, *161*, 59-78.
52. Van Dillen, A.J.; Terörde, R.J.A.M.; Lensveld, D.J.; Geus, J.W.; de Jong, K.P. *J. Catal.* **2003**, *216*, 257-264.
53. Van den Brink, P.J.; Scholten, A.; Van Wageningen, A.; Lamers, M.D.A.; Van Dillen, A.J.; Geus, J.W. *Stud. Surf. Sci. Catal.* **1991**, *63*, 527-537.
54. Wang, Y.; Noguchi, M.; Takahashi, Y.; Ohtsuka, Y. *Catal. Today* **2001**, *68*, 3-9.
55. Louis, C.; Cheng, Z.X.; Che, M. *J. Phys. Chem.* **1993**, *97*, 5703-5712.

# 2

# Aqueous metal nitrate solutions with ordered mesoporous supports: impregnation and drying phenomena

The impregnation and drying of ordered mesoporous silica (SBA-15) using $[Ni(OH_2)_6](NO_3)_2$ precursor solution was investigated. The impregnation step was studied using the cryo-TEM technique that is often used for studying biological systems, and to our best knowledge has now been used for the first time to study precursor solution distributions inside SBA-15 support particles. The cryo results showed that a significant number of mesopores had remained empty after impregnation, and patches supposedly containing precursor solution were found outside the mesopores. Analysis of the freeze-dried impregnate showed that the remaining precursor solution indeed was present at the exterior surface of the SBA-15 particles. Upon thermal drying of the impregnate 9 nm $Ni_3(NO_3)_2(OH)_4$ crystallites formed that were non-uniformly distributed as many empty pores were observed. However, agglomerates of precursor were no longer found outside the mesopores. This could be explained by transport of precursor present at the exterior surface into the filled pores during drying, resulting in a higher loading than anticipated. Finally, we show the impact of the well-defined pore structure of ordered mesoporous supports as well as conventional silica gel supports on confinement of crystal growth of $Ni_3(NO_3)_2(OH)_4$ during drying.

## Introduction

In the early seventies Chiola *et al.* patented a method to prepare ordered mesoporous silicas using ionic surfactants as structure directing agents.[1] However, at that time the ordered nature of the pores was not recognised and only the high porosity was noted. The breakthrough came in 1992 when researchers of the Mobil Oil Corporation synthesised similar materials, and discovered the ordered structure using low-angle powder X-ray diffraction.[2-5] The synthesis parameters such as reaction conditions, silica source, and type of surfactant offered many possibilities to obtain ordered mesoporous supports with diverse pore geometries and pore sizes. Hence, a family of M41S materials abbreviated as MCM-41, which denotes Mobil Composition of Matter No. 41, MCM-48 and MCM-50 were developed that displayed hexagonal, cubic or lamellar pore symmetry, respectively. The former became most popular because of its relatively robust synthesis and well-defined unidimensional pores arranged in a honeycomb-like structure. It opened up many opportunities for application, for instance as molecular sieve[6], drug-delivery system[7], host material for enzymes[8], and as support material for catalysts[9-11]. Next to the well-defined pores that could be varied from diameters of 2 to 10 nm, and that may provide uniform active sites with well-controlled steric effects, the high surface area of MCM-41 is attractive for heterogeneous catalysts[12,13] as this offers the possibility to apply high loadings of the active metal (oxide) component. However, due to the relatively thin amorphous pore walls of about 0.5 to 1.5 nm of MCM-41, the (hydro)thermal stability of the material soon showed to be a limiting factor for application. Although papers were published that described methods to increase the hydrothermal stability[14,15], the improvements were modest compared to the breakthrough in 1998 brought about by Zhao and co-workers.[16,17] These researchers reported that with triblock copolymers as structure directing agents, materials could be obtained with pore walls of 3 to 7 nm, resulting in a high (hydro)thermal stability compared to that of MCM-41. The structured material was labelled SBA-15, short for Santa Barbara No. 15, and contained hexagonal pores with a diameter adjustable between 6 to about 15 nm depending on the synthesis temperature applied during gel ageing or type of block copolymer used. As a consequence of the copolymer template, the mesopore walls of SBA-15 are microporous and hence the mesopores are interconnected.[18] Because of this connection between the mesopores, SBA-15 is also often used as a hard template to obtain carbon[19], metal[20] or metal oxide[21,22] replica structures by the so-called nanocasting technique.

The ordered pore structures of MCM-41 and SBA-15 offer many opportunities for new catalytic processes and several strategies have been reported for introduction of catalytic functions and subsequent exploitation of the ordered structure.[9-11] The catalytically active component is either introduced during synthesis of the support or post-synthesis. The latter is often preferred as incorporation of the active phase during synthesis is generally cumbersome due to the complexity of achieving simultaneous condensation of both phases and retention of the formation of an

ordered pore symmetry. The impregnation and drying technique is by far the most frequently used post-synthesis method, and involves impregnation of the support with a precursor-containing solution and subsequent evaporation of the solvent. Next, the dried impregnate is heat treated in air, referred to as calcination, to bring about the respective metal oxide. When the metal is the desired component, the treatment is followed by high-temperature reduction with $H_2$. The properties of the precursor solution largely affect the final dispersion of the active component and can cause structural collapse of the ordered pore system, especially for MCM-41 due to its relatively thin pore walls.[23-25]

Metal nitrate salts are highly soluble in water and thereby enable high loadings via single-step impregnation, while pure metal oxides can be obtained by subsequent thermal decomposition of the nitrate. A wide variety of MCM-41 and SBA-15 supported metal (oxide) catalysts have been prepared, characterised and catalytically tested that were based on impregnation with aqueous metal nitrate solutions. However, few papers have shown systematic data on the impact of the preparation steps on the uniformity of the distribution of the final metal (oxide) particles throughout individual mesopores.[26-28] Moreno *et al.* studied Fe on MCM-41 catalysts, whereas Janssen *et al.* and Impéror-Clerc and co-workers reported findings on SBA-15 supported Au and $ZrO_2$, and $MnO_2$ systems, respectively. Consensus amongst these studies was the observation of many empty mesopores in the final catalysts. These findings are in line with quantitative electron tomography (ET) results that we recently obtained for NiO/SBA-15 catalysts, prepared via the impregnation and drying method using aqueous $[Ni(OH_2)_6](NO_3)_2$ precursor solution.[29] The ET results demonstrated that NiO was non-uniformly distributed over the pores and it was speculated that this was related to the impregnation and drying steps. On the one hand uniform wetting upon impregnation might be hampered due to the ordered pore symmetry, but on the other hand redistribution of precursor during drying is often observed with conventional supports.[30,31] Identification of which of these processes is responsible for non-uniform distribution of the active phase is important because complete filling of all the pores could yield catalysts with much higher loadings.

Generally, Transmission Electron Microscopy (TEM) is used to gain insight into the distribution of the active phase or its precursor. Unfortunately, only dry samples can be studied with conventional TEM due to the poor stability of the wet samples. From the field of biology it is known that the stability of beam-sensitive samples such as tissue can be improved by studying the specimen under cryogenic conditions using liquid $N_2$.[32] We used this methodology for the first time to image of the distribution of precursor solution inside porous support bodies after impregnation. Insight into the influence of the drying step was further gained by characterisation of the dried impregnates using TEM, XRD and $N_2$-physisorption. Finally, we show the impact of the pore structure of ordered mesoporous supports as well as conventional silica gel supports on confinement of the crystal growth of $Ni_3(NO_3)_2(OH)_4$.

## Experimental

*Sample preparation*

For the preparation of MCM-41 the procedure of Kresge *et al.*[2] was followed and MCM-41 supports with varying pore diameters were obtained using surfactants with different alkyl chain lengths: tetradecyltrimethyl ammonium bromide ($C_{14}$), cetyltrimethyl ammonium bromide ($C_{16}$) and octadecyltrimethylammonium bromide ($C_{18}$). Surfactants $C_{14}$ and $C_{16}$ were ordered from Acros, whereas $C_{18}$ was obtained from Aldrich. 5.46 g of 25 wt% tetramethylammoniumhydroxide basic solution (Acros) was diluted with 50 g (for $C_{14}$ and $C_{16}$) or 100 g (for $C_{18}$) of demineralised water in a 500 ml polypropylene flask. Then surfactant was added, and the mixture was stirred at 40 °C (for $C_{14}$ and $C_{16}$) or 60 °C (for $C_{18}$) till the solution was clear and all surfactant had dissolved. Next, 4.51 g of Aerosil380 silica powder was added under vigorous stirring for another hour at 40 °C (for $C_{18}$ at 60 °C), and a molar gel composition of 1 $SiO_2$ : 0.25 surfactant : 0.20 base : 40 $H_2O$ was obtained for $C_{14}$ and $C_{16}$. As more water was used with the $C_{18}$ synthesis, the molar composition of this mixture was 1 $SiO_2$ : 0.25 surfactant : 0.20 base : 55 $H_2O$. The stirring was turned off after 1 hour, and the reaction mixture was aged for 20 hours at 40 °C (for $C_{18}$ at 60 °C). The reaction mixture was then transferred to a teflon-lined steel autoclave and kept at 150 °C for 48 hours under autogeneous pressure. After quenching, the sample was filtered and the solid was thoroughly washed with demineralised water. The solid was dried for 6 hours at 60 °C and for 6 hours at 120 °C in static air. After mild grinding the solid was heated in static air (ramp= 2 °C.min$^{-1}$) for 2 hours at 120 °C, and then for 6 hours at 550 °C. The calcined products prepared with the $C_{14}$, $C_{16}$ and $C_{18}$ surfactants were labelled MCM-$C_{14}$, MCM-$C_{16}$ and MCM-$C_{18}$, respectively.

SBA-15 was prepared following the procedure of Zhao and co-workers.[16] 8 g of $PEO_{20}PPO_{70}PEO_{20}$ (PEO= poly(ethylene oxide) and PPO= poly(propylene oxide)) tri-block copolymer (Aldrich) was dissolved in 250 ml demineralised water of 40 °C. After the solution had become clear, 48 g of concentrated HCl was added, followed by the addition of 21.5 ml of tetraethyl orthosilicate (Acros). The mixture was stirred for 20 hours at 40 °C and then transferred to an oven for further reaction at 80 °C for 48 hours. The solid product was collected from the suspension by filtration, washed, dried in air for 12 hours at 80 °C and calcined for 6 hours at 550 °C. Grace-Davison Davicat 1404, 1452 and 1351 silica gel powders with average pore diameters of about 7, 11 and 14 nm were labelled G7, G11 and G14, respectively, and used as received.

The 4.2 M $[Ni(OH_2)_6](NO_3)_2$ and 3.6 M $[Cu(OH_2)_6](NO_3)_2$ precursor solutions were prepared by dissolving $Ni(NO_3)_2.6H_2O$ and $Cu(NO_3)_2.3H_2O$ (Acros) in demineralised water. A quantity of 0.25 g (for MCM-41 and SBA-15) or 1.00 g (for silica gel) of support was brought into a round bottom flask with two outer joints. One of the joints was sealed with a septum and the second one was connected to a vacuum pump. Then dynamic vacuum (~20 mbar) was applied and the support was dried at 80 °C for 2 hours to remove physisorbed water. After switching to static vacuum, the support was impregnated by adding precursor solution drop-wise over a period of about 2

minutes using a syringe. During impregnation and subsequent equilibration, the support powder was continuously stirred to improve wetting of the support particles with the precursor solution. For the MCM-$C_{14}$, MCM-$C_{16}$ and MCM-$C_{18}$ supports 0.9, 1.2 and 1.6 ml.g$^{-1}$ of $[Ni(OH_2)_6](NO_3)_2$ precursor solution were used, respectively, whereas SBA-15 was impregnated with 1.0 ml.g$^{-1}$ or 1.8 ml.g$^{-1}$ of the same solution. The Cu impregnate was prepared by impregnating SBA-15 with 1.0 ml.g$^{-1}$ of the $[Cu(OH_2)_6](NO_3)_2$ precursor solution to yield a $Cu_2(OH)_3NO_3$ loading of 30 wt%. After equilibration for 45 minutes, the impregnates were dried in static air by increasing the temperature at a rate of 1 °C.min$^{-1}$ to 120 °C for the Ni samples and to 70 °C for the Cu impregnate. The final drying temperature was kept for 12 hours. The Ni/MCM-41 products were labelled MCM-$C_{14}$/D, MCM-$C_{16}$/D and MCM-$C_{18}$/D and displayed $Ni_3(NO_3)_2(OH)_4$ loadings of 32, 39 and 45 wt%, respectively. The SBA-15 impregnates prepared with 1.0 ml.g$^{-1}$ or 1.8 ml.g$^{-1}$ were denoted SBA-15/D1.0 and SBA-15/D1.8 and contained 34 and 49 wt% $Ni_3(NO_3)_2(OH)_4$, respectively.

Freeze-drying of the SBA-15 impregnate (0.25 g support) was carried out by cooling the sample to -40 °C using a mixture of dry ice and acetone, followed by evacuation using a mechanical vacuum pump (~8 mbar) and a cold trap (-196 °C). The sample was dried for 8 hours at that temperature and the sample was allowed to slowly warm-up to +7 °C.

*Characterisation*

$N_2$-physisorption measurements were performed at -196 °C, using a Micromeritics Tristar 3000 apparatus. The samples were dried in He flow for 14 hours at 120 °C prior to analysis. The pore size distributions of the MCM-41 and SBA-15 samples were derived from the adsorption branch of the isotherm using non-local density functional theory (NL-DFT). A model developed by Jaroniec *et al.*[33] for ordered mesoporous silica supports with cylindrical pore geometry was used as this model seemed to provide a reliable representation of the data. The pore size distributions of the silica gel powders were calculated from the desorption branch using BJH theory[34] with the Harkins and Jura[35] thickness equation. The pore diameter was defined by the value at which the maximum in differential pore volume was observed. The micro- and meso-porosity were defined as the volume present in pores ≤2 nm, and between 2-50 nm, respectively. Mesopore and external surface areas were determined with the t-method[36] using thickness ranges of 0.35-0.55 and 1.00-1.41 nm, respectively. The t-method was also used to calculate the micro- and mesopore volumes of the silica gel supports.

Powder X-ray diffraction (XRD) patterns were obtained at room temperature from 10 to 85° 2θ with a Bruker-AXS D8 Advance X-ray Diffractometer setup using Co-K$\alpha_{12}$ radiation. The average $Ni_3(NO_3)_2(OH)_4$ and $Cu_2(OH)_3NO_3$ crystallite size were calculated according to the Scherrer equation ($k$= 1) using the most intense (001) peak at 2θ = 14.9°.

Scanning transmission electron microscopy (STEM) images were obtained using a Tecnai 20 microscope operating at 200 kV and equipped with High-Angle

Annular Dark-Field (HAADF) (camera length: 120 mm) and Energy Dispersive X-ray Spectrometer (EDX). We used a High-Angle Annular Diffraction detector for imaging as this dark-field mode yields Z-contrast images[37] and hence was expected to allow better differentiation between precursor solution and support. HAADF-STEM tilt series were obtained by recording images from -70° to +65° with 1° intervals. Alignment of the tilt series was carried out using FEI Inspect3d software. For the cryo experiments a Gatan cryoholder Model 626 was used, and the freshly impregnated SBA-15 sample was cooled to -196 °C with liquid $N_2$.

## Results and Discussion

*Incipient wetness impregnation*

The impregnation step was studied by imaging the $[Ni(OH_2)_6](NO_3)_2$ precursor solution distribution in the porous support bodies of SBA-15 with cryo-TEM. A HAADF-STEM image of pristine SBA-15 has been given in the top-left frame of Figure 1. The bright areas reflect the amorphous $SiO_2$ pore walls, and the on-top view shows the hexagonal arrangement of the mesopores. The other images shown in Figure 1 are typical cryo HAADF-STEM images that were obtained from SBA-15 that was impregnated to incipient wetness with 1.0 $ml.g^{-1}$ of $[Ni(OH_2)_6](NO_3)_2$ precursor solution. The bottom-frame images show SBA-15 particles viewed on-top and display the hexagonal arranged pores. These images indicated that precursor solution was non-uniformly distributed over the pores as a large number of dark dots corresponding to empty pores were observed. Moreover, the filled pores appeared clustered in groups. The observation that many pores had remained empty while the amount of solution offered was higher than the mesopore volume (see Table 1) implied that precursor solution had to be present outside the mesopores. The top-right image in Figure 1 recorded at lower magnification revealed indeed, as indicated by the arrows, precursor solution patches present at the exterior surface of the SBA-15 support particles. To address whether these patches originated from the precursor solution or deposition of ice from freezing of ambient water vapour, we attempted to determine the Ni content that was present in these patches. Hence, we carried out elemental analysis using an EDX detector. As the patches were present on-top of the SBA-15 particles, we could only derive information from the relative increase of the Ni peak of the spectra of agglomerate-containing domains with those of 'clean' domains. Higher Ni concentrations were observed for these agglomerate domains. However, it should be noted that interpretation of these results was complicated as variations in the local sample thickness were apparent, which may have affected the outcome of the results. Nevertheless, we could conclude from the cryo-TEM results that precursor solution was non-uniformly distributed and that precursor solution patches appeared at the exterior surface.

In order to gain more insight into the presence of precursor solution at the exterior surface, and to verify the conclusions from the cryo-TEM results, we carried out

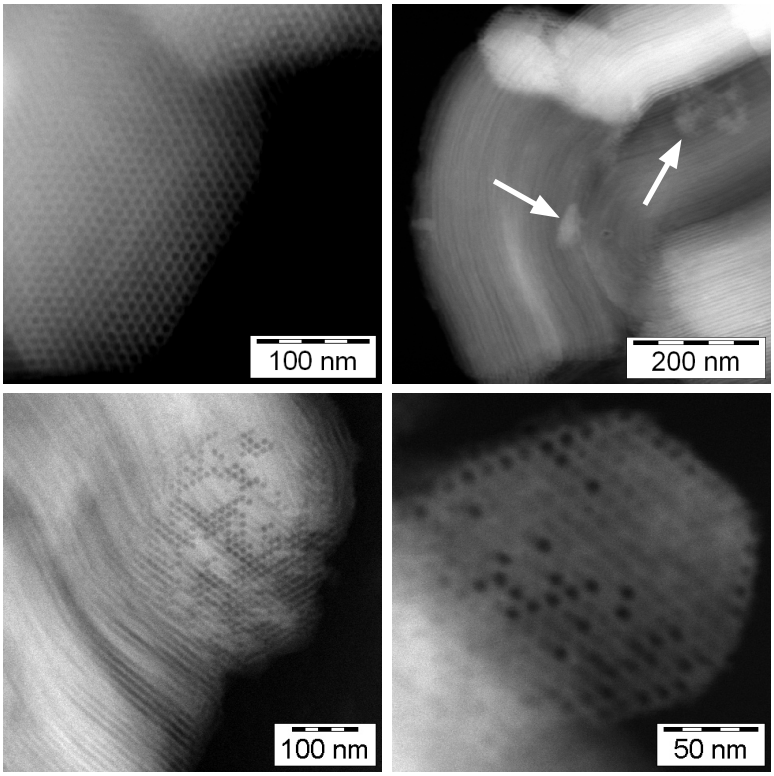


*Figure 1.* (cryo) HAADF-STEM images of pristine SBA-15 (top-left) and SBA-15 that was impregnated with 1.0 ml.g$^{-1}$ of aqueous $[Ni(OH_2)_6](NO_3)_2$ solution. The dark dots in the bottom images reveal empty pores and bright spots filled ones. The arrows (top-right) indicate frozen liquid patches outside of the pores.

an additional experiment that involved freeze-drying of SBA-15 that had been impregnated with the same amount of $[Ni(OH_2)_6](NO_3)_2$ precursor solution. The freeze-drying technique, often used in the food industry, is a dehydration process in which the material is frozen, followed by reducing the pressure. As a result sublimation of water takes place and the material is dehydrated. Advantage of this drying technique for our study was that no mobility of precursor solution was expected and hence, the distribution of precursor present after impregnation was quenched. In Figure 2, electron micrographs are given of the SBA-15 product that was thus obtained. The two top-frame images show SBA-15 particles viewed on-top (left) and along the mesopores (right), the image in the bottom-frame displays an enlargement of the rectangle region A indicated in the top-left image. The contrast between filled and empty pores was somewhat less pronounced than with the

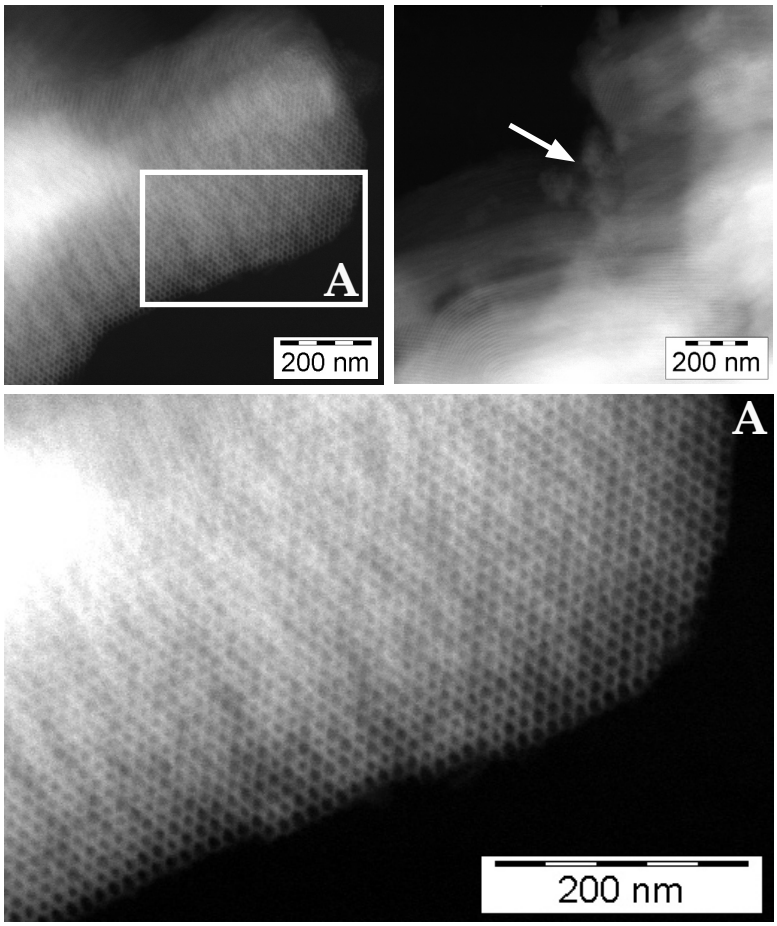


*Figure 2.* HAADF-STEM images of SBA-15 obtained after impregnation with $[Ni(OH_2)_6](NO_3)_2$ solution and subsequent freeze drying. The top-left image indicates non-uniform filling, which is better observed in the enlarged image of region A (bottom-frame). The top-right image shows the presence of precursor agglomerates outside the pores, as indicated by the arrow.

cryo results due to removal of water, but the results showed that the non-uniform distribution of precursor over the pores had been retained, as expected. The cryo TEM finding that filled pores were present in domains was confirmed too. The image displayed on the right-hand side of Figure 2 showed that agglomerates were present outside the SBA-15 support particles, as indicated by the arrow. We conclude that not all precursor solution had entered the pores upon impregnation, and that part of the solution was present at the exterior surface of the support particles. The non-uniform filling of the pores could be related to insufficient contact between the

support and precursor solution or to the relatively low hydroxyl density[38-43] of about 1 to 3 OH.nm$^{-2}$ of ordered mesoporous supports compared to that of conventional silicas[44] (4 to 6 OH.nm$^{-2}$). Considering the relatively hydrophobic character, it is not unlikely that this could have resulted in non-uniform wetting of pores and, hence partial filling of all the pores with $[Ni(OH_2)_6](NO_3)_2$ solution.

*Drying*

After adding precursor solution to the support and equilibration for 45 minutes, impregnates were heated slowly (1 °C.min$^{-1}$) to 120 °C to evaporate the solvent and to induce deposition of the precursor onto the support. With conventional supports, the drying step induces more often than not redistribution of precursor due to capillary flow brought about by their broad pore size distributions. Because of the well-defined pore sizes of ordered mesoporous SBA-15 this type of migration is not expected. However, precursor solution transport from the exterior of the particles into the pores perhaps could take place. In addition, the microporous connections between the mesopores could facilitate migration of precursor solution between pores during drying. Therefore, we studied the drying step in more detail. The SBA-15 impregnate was prepared using the same impregnation procedure as in the above-mentioned experiments. The obtained dried impregnate was labelled SBA-15/D1.0. Low-angle XRD measurement showed that the ordered structure of SBA-15 had been retained upon impregnation and drying as the typical diffraction lines for SBA-15[16] were observed. XRD analysis at higher angles showed that a layered nickel nitrate hydroxide[45-47] had formed, also referred to as basic nickel nitrate, with composition $Ni_3(NO_3)_2(OH)_4$ and an average crystal size of 9 nm. This value was in good agreement with the mesopore diameter of 9 nm and suggested confinement of the $Ni_3(NO_3)_2(OH)_4$ crystallites by the pore walls of SBA-15. Unfortunately, the XRD diffraction pattern did not allow us to estimate the aspect ratio of the $Ni_3(NO_3)_2(OH)_4$ crystallites as only the (001) peak was suitable for line-broadening analysis. Subsequently, the sample was characterised using $N_2$-physisorption (Table 1). It should be noted that the data were corrected for the contribution of the $Ni_3(NO_3)_2(OH)_4$ to the total weight of the sample. The physisorption results suggested that precursor had been deposited predominantly inside the pores as the mesoporosity ($V_{meso}$) had lowered from 0.68 to 0.42 $cm^3.g_{SiO2}^{-1}$. Moreover, the total porosity of 0.47 $cm^3.g_{SiO2}^{-1}$ was considerably lower than expected (0.63 $cm^3.g_{SiO2}^{-1}$), supposedly due to partial blocking of mesopore volume by the $Ni_3(NO_3)_2(OH)_4$ crystallites. Finally, the $Ni_3(NO_3)_2(OH)_4$ distribution was monitored with TEM. A selected HAADF-STEM image from a tilt series has been given in the left frame of Figure 3. The image shows the hexagonal array of pores of an SBA-15 particle and demonstrated that $Ni_3(NO_3)_2(OH)_4$ was non-uniformly distributed over the pores as many dark dots pointed to empty pores. The tilt series obtained for this particle as well as other particles confirmed that many pores were empty. The presence of the empty pores could be caused by a more hydrophobic character of these pores due to the relatively low silanol density (*vide supra*) or perhaps they had been physically blocked by incompletely removed template or

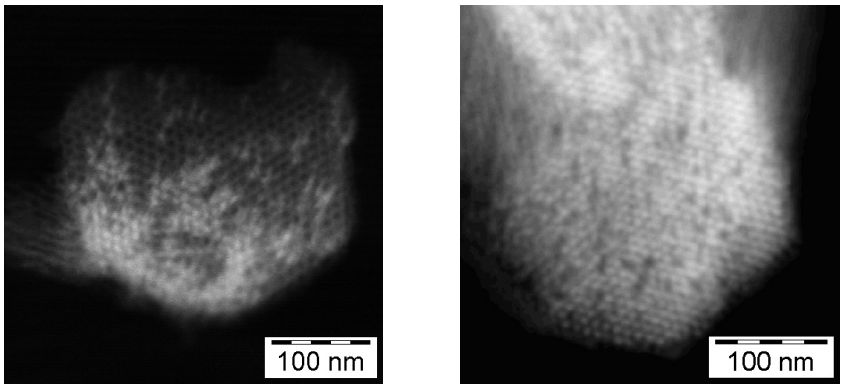


*Figure 3.* HAADF-STEM images of SBA-15 samples dried at 120 °C after impregnation with either 1.0 ml.g$^{-1}$ (SBA-15/D1.0) or 1.8 ml.g$^{-1}$ (SBA-15/D1.8) of $[Ni(OH_2)_6](NO_3)_2$ precursor solution.

*Table 1.* Overview of $N_2$-physisorption results of pristine supports and dried impregnates.

| Sample | $d_{pore}$ (nm) | Surface area ($m^2.g_{SiO2}^{-1}$) | | Porosity ($cm^3.g_{SiO2}^{-1}$) | | | |
|---|---|---|---|---|---|---|---|
| | | $S_t$ [a] | $S_{t,ext}$ [b] | $V_{tot,calc}$ [c] | $V_{tot,exp}$ [d] | $V_{meso}$ [e] | $V_{micro}$ [f] |
| SBA-15 | 8.7 | 516 | 38 | 0.78 | 0.78 | 0.68 | 0.05 |
| SBA-15/D1.0 | 8.7 | 293 | 33 | 0.63 | 0.47 | 0.42 | 0.01 |
| SBA-15/D1.8 | 8.7 | 342 | 32 | 0.50 | 0.42 | 0.33 | 0.06 |
| MCM-41$_{C14}$ | 3.5 | 1091 | 50 | 0.76 | 0.76 | 0.73 | 0.00 |
| MCM-41$_{C14}$/D | 3.2 | 554 | 28 | 0.63 | 0.39 | 0.36 | 0.00 |
| MCM-41$_{C16}$ | 4.0 | 908 | 46 | 0.76 | 0.76 | 0.72 | 0.00 |
| MCM-41$_{C16}$/D | 4.0 | 557 | 31 | 0.58 | 0.45 | 0.42 | 0.00 |
| MCM-41$_{C18}$ | 4.5 | 938 | 98 | 0.99 | 0.99 | 0.82 | 0.00 |
| MCM-41$_{C18}$/D | 4.4 | 541 | 83 | 0.76 | 0.67 | 0.47 | 0.00 |
| G7 | 6.9 | 512 | 25 | 0.89 | 0.89 | 0.84 | 0.00 |
| G11 | 10.8 | 358 | 10 | 1.02 | 1.02 | 1.00 | 0.00 |
| G14 | 14.1 | 287 | 21 | 1.19 | 1.19 | 1.15 | 0.01 |

[a]mesopore surface area; [b]external surface area; [c]expected total pore volume based on contribution of $Ni_3(NO_3)_2(OH)_4$ precursor to volume decrease; [d]total pore volume derived from amount of $N_2$ adsorbed at $p/p_o$=0.995; [e]mesopore volume; [f]micropore volume.

defects formed during synthesis of the SBA-15. To verify whether it was possible to fill all the pores with precursor solution, we increased the amount of precursor solution offered to pristine SBA-15 during impregnation from 1.0 to 1.8 ml.g$^{-1}$. The impregnate was dried at 120 °C and labelled SBA-15/D1.8. XRD analysis showed that $Ni_3(NO_3)_2(OH)_4$ had formed and with line-broadening an average crystal size of 9 nm was found, again suggesting confinement. Surprisingly, offering the quantity of precursor solution well-above the pore volume of the support had not led to an increase of the average crystallite size. $N_2$-physisorption (Table 1) also supported that more precursor had been deposited inside the pores as the mesoporosity had lowered to 0.33 cm$^3$.$g_{SiO2}^{-1}$. A typical electron micrograph of this sample is depicted on the right-hand side in Figure 3. The image of the SBA-15 particle indicated that a substantially larger fraction of all the pores now contained $Ni_3(NO_3)_2(OH)_4$ precursor. Hence, the results suggest that there was no physical barrier for the precursor solution to enter the pores during impregnation. Therefore, we propose that the non-uniform filling is rather associated with inadequate contact between precursor solution and all the support particles during the impregnation process than with the presence of fully hydrophobic pockets. However, the non-uniform contacting might be brought about by the more hydrophobic properties of SBA-15.

STEM analysis of both the SBA-15/D1.0 and SBA-15/D1.8 dried impregnates also had revealed that no agglomerates or large particles of $Ni_3(NO_3)_2(OH)_4$ were present outside the mesopores. $Ni_3(NO_3)_2(OH)_4$ formation from aqueous $[Ni(OH_2)_6](NO_3)_2$ solution by heating involves precipitation of $Ni(NO_3)_2.6H_2O$ and subsequent hydrolysis of this component. The absence of $Ni_3(NO_3)_2(OH)_4$ outside the pores could be explained by transport of solute from the solvent present at the exterior into the mesopores during the drying process. In Figure 4 a schematic representation is given to illustrate this hypothesis. Upon drying solvent present at the exterior of the support particles is expected to evaporate first.[30,48,49] The $[Ni(OH_2)_6](NO_3)_2$ complex present in this solution could precipitate as $Ni(NO_3)_2.6H_2O$, but it is proposed that the solute diffuses into the solution present inside the filled pores. The latter implies that the external solution is in contact with the solution inside the mesopores, as illustrated in Figure 4. Moreover, the solubility of the salt should be high enough to prevent precipitation upon evaporation during drying. Alternatively, migration could have occurred after initial precipitation of $Ni(NO_3)_2.6H_2O$ outside the mesopores. Subsequent infiltration upon melting of the precipitated $Ni(NO_3)_2.6H_2O$ at temperatures above 57 °C could then enable mobility of precursor. The latter hypothesis is supported by a recently reported simple and effective method for the preparation of rodlike metal oxide particles.[50,51] The method comprises of physical mixing of a metal (i.e. Co, Ni, Ce and Cr) nitrate precursor with a silica template such as SBA-15, followed by heating of the mixture above the melting point of the nitrate, resulting in migration of the liquid phase into the pores.

The hypothesis that precursor transported from extra-porous precursor patches into the mesopores that were in contact with these patches, implicated that the final loading of these pores should be higher than the 34 wt% $Ni_3(NO_3)_2(OH)_4$ expected

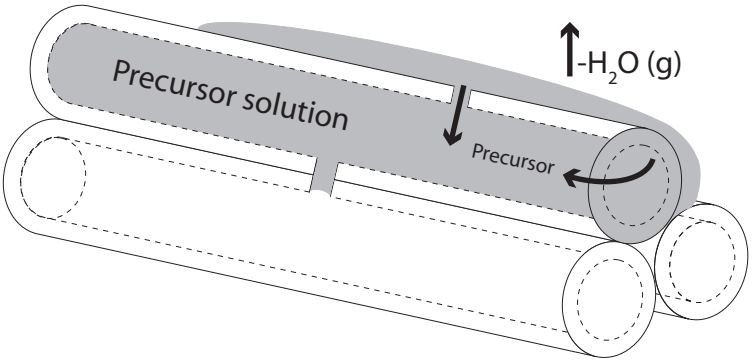


*Figure 4.* Proposed transport of extra-porous nickel nitrate precursor into the mesopores of SBA-15 during drying. Solvent evaporation is expected to start from the exterior liquid and precursor complex diffusion from this solution into the filled pores can take place during this stage, or during the following drying stage when $Ni(NO_3)_2.6H_2O$ melts to decompose into $Ni_3(NO_3)_2(OH)_4$.

based on the concentration and amount of precursor solution that was impregnated. Recently, using ET, we developed a nanoscale loading model for a NiO/SBA-15 *ex* nitrate catalyst that provided the average NiO loading in individual pores and the percentage of filled pores. These results were obtained using a novel heat treatment[52] (see chapters 4 and 5) that allowed conversion of the $Ni_3(NO_3)_2(OH)_4$ of sample SBA-15/D1.0 into NiO without redistribution. Hence, the $Ni_3(NO_3)_2(OH)_4$ loadings in the filled pores could be determined from these results and were found to vary between 44 wt% and 59 wt%. These findings concur with our proposed hypothesis that transport into the filled pores took place during drying.

The amount of $[M(OH_2)_6](NO_3)_2$ solution (M=metal) that can transfer into the pores during drying will depend on its solubility as a function of the temperature. The migration could be hampered if hydrolysis of the metal aqua complex takes place, resulting in precipitation of a metal nitrate hydroxide outside the pores. Copper is well-known for its low solubility due to formation of $Cu(OH)_2$, or $Cu_2(OH)_3NO_3$ when precipitating from a nitrate-containing solution.[53-57] In Figure 5 a bright-field TEM image (left) and electron diffraction pattern (right) thereof are shown of SBA-15 that was impregnated with a 3.6 M $[Cu(OH_2)_6](NO_3)_2$ precursor solution, followed by slowly heating to 70 °C to evaporate the solvent. The TEM image demonstrated that large hexagonally shaped particles were found at the exterior of the support particles as indicated by the arrow. More detailed analysis showed that precursor was present inside the pores too. Electron diffraction confirmed that the hexagonal particles were crystalline and EDX analysis demonstrated that they contained Copper. XRD analysis (Figure 6) showed that copper nitrate hydroxide with composition $Cu_2(OH)_3NO_3$ had formed.[58] The broadening of the diffraction peaks was close to the instrumental

line-broadening, indicating that the average crystal size was larger than 25 nm.

Based on aforementioned results we propose that the observed absence of precursor agglomerates outside of the mesopores after drying when a 4.2 M $[Ni(OH_2)_6](NO_3)_2$ precursor solution is used, can be attributed to transport of precursor at the exterior surface into the filled mesopores during drying.

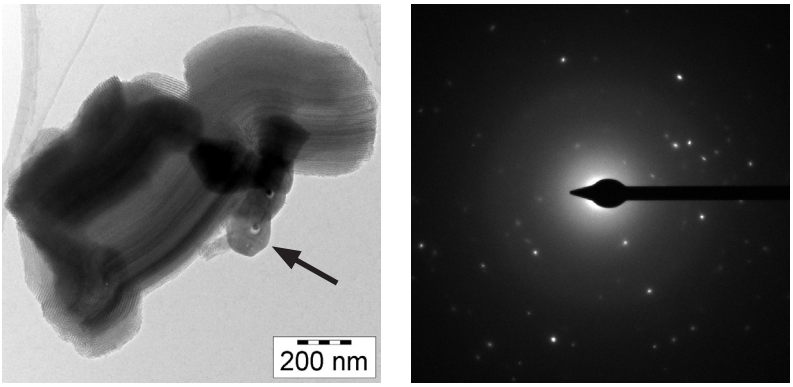


*Figure 5.* Bright-field STEM image (left) of $Cu_2(OH)_3NO_3$/SBA-15 obtained after impregnation with 3.6 M $[Cu(OH_2)_6](NO_3)_2$ solution, and drying at 70 °C. Large hexagonal-shaped particles were observed outside the pores, as indicated by the arrow. On the right-hand side an electron-diffraction image obtained from this area is given.

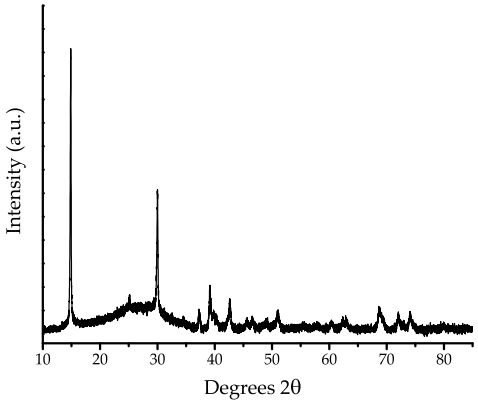


*Figure 6.* XRD pattern obtained after impregnation of SBA-15 with 3.6 M $[Cu(OH_2)_6](NO_3)_2$ solution, followed by drying at 70 °C. The observed diffraction lines originate from $Cu_2(OH)_3NO_3$.

*Confined crystallisation of $Ni_3(NO_3)_2(OH)_4$*

XRD analysis of the SBA-15/D1.0 and SBA-15/D1.8 dried impregnates showed that the $Ni_3(NO_3)_2(OH)_4$ average crystal sizes in these samples were similar to the average mesopore diameter of 9 nm. To find out if the crystal size depended on the pore diameter, we carried out a series of experiments with ordered mesoporous silicas MCM-41 as these supports have the same hexagonal pore symmetry as SBA-15. However, MCM-41 has unidimensional pores as it does not contain intra-wall micropores that connect the mesopores like with SBA-15. The pore diameter of MCM-41 can be varied relatively easy when surfactants with different alkyl chain lengths are used. Three supports were synthesised that were labelled MCM-$41_{C14}$, MCM-$41_{C16}$ and MCM-$41_{C18}$. Low-angle XRD patterns of the materials contained peaks that could be indexed as the (100), (110), (200) and (210) diffraction lines of the hexagonal *p6mm* symmetry of MCM-41. $N_2$-physisorption analysis (see Table 1) of the supports showed that they contained all the features typical for MCM-41 materials.[2] The pore size distribution plots calculated from $N_2$-physisorption results have been plotted in the left-hand side of Figure 7. The obtained pore size distributions showed that high-quality supports had been synthesized as narrow pore size distributions were present with maxima at 3.5, 4.0 and 4.5 nm for MCM-$41_{C14}$, MCM-$41_{C16}$ and MCM-$41_{C18}$, respectively.

The MCM-41 supports were impregnated to incipient wetness with the $[Ni(OH_2)_6](NO_3)_2$ precursor solution, dried at 120 °C, and analysed with $N_2$-physisorption and XRD. The physisorption isotherms and low-angle XRD measurements (not depicted) showed that the ordered structure of the samples had been retained upon impregnation and drying. Moreover, the mesoporosity values of the samples, given in Table 1, displayed a considerable decrease indicating that precursor was predominantly present inside the mesopores. XRD patterns recorded at higher angles are shown in the left-hand side of Figure 8. The patterns showed

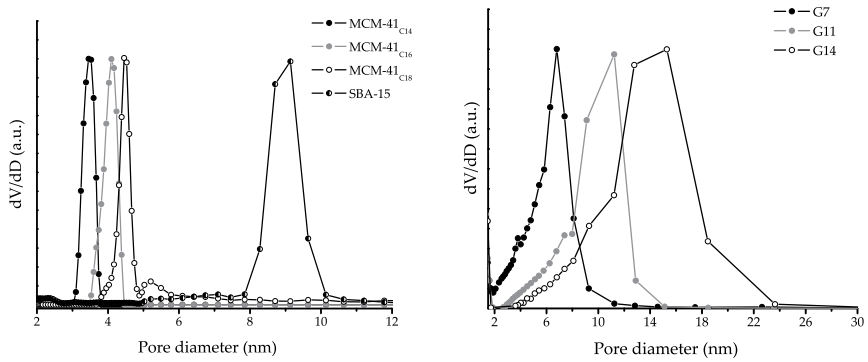


*Figure 7.* Pore size distributions calculated from $N_2$-physisorption results of MCM-41 C14 to C18 and SBA-15 supports (left) and those of conventional silica gel powders G7, G11 and G14 (right) .

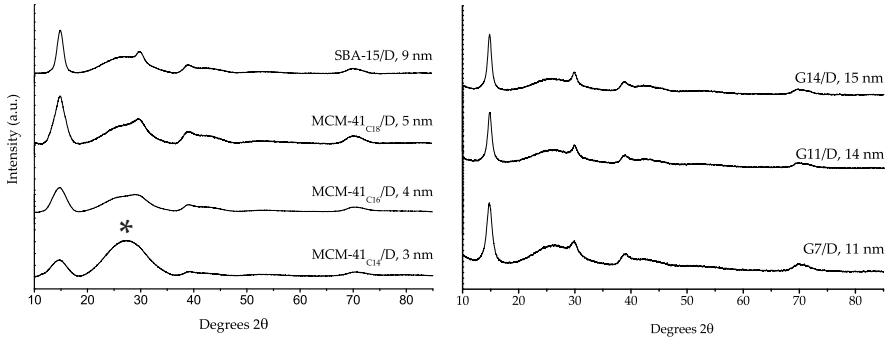


*Figure 8.* XRD patterns of ordered (left) and conventional (right) silica-supported $Ni_3(NO_3)_2(OH)_4$ samples obtained after incipient wetness impregnation with aqueous $[Ni(OH_2)_6](NO_3)_2$ precursor solution, and drying at 120 °C. *broad peak originating from the amorphous $SiO_2$ support.

that $Ni_3(NO_3)_2(OH)_4$ had formed in all cases, but that the line-width varied. In Figure 9, the average crystal sizes obtained from XRD have been plotted as a function of the average pore diameter, as calculated from $N_2$-physisorption. The error bars indicate the pore size distribution of the supports at full-width-at-half-maximum (FWHM). For comparison reasons sample SBA-15/D1.0 has been included too. The graph demonstrated for all samples that the obtained average $Ni_3(NO_3)_2(OH)_4$ crystal size was in close agreement with the average pore diameter and hence we concluded that ordered mesoporous supports confine the final crystal size obtained after impregnation and drying.

To gain insight into the importance of the nature of the pores on crystal size confinement, we benchmarked the results obtained with MCM-41 and SBA-15 with three conventional silica gel powders. The $N_2$-physisorption pore size distribution plots of the selected silicas are shown in the right-hand side of Figure 7, and an overview of the physisorption results are given in Table 1. Figure 7 showed that the silica gel supports had broad pore size distributions. Based on the maxima average pore sizes of 7, 11 and 14 nm were determined and the support materials were denoted G7, G11 and G14, respectively. Subsequently, these supports were impregnated to incipient wetness using the same precursor solution and dried at 120 °C. The XRD patterns obtained for the dried impregnates are given in the right frame of Figure 8. Similar as to the ordered mesoporous supports, the obtained average $Ni_3(NO_3)_2(OH)_4$ crystal sizes varied as a function of the pore size. In Figure 9, the relation between the average crystal size and average pore diameter is shown. The plot showed that confinement took place with these supports too, but the correlation between average crystal size and average pore diameter was less well-defined than with the ordered mesoporous supports. Hence, we concluded that both ordered mesoporous support and conventional silica gel supports confined crystal growth of $Ni_3(NO_3)_2(OH)_4$. With the unidimensional pores of the ordered mesoporous supports, the average crystal size is close to the average pore diameter, while with the three-dimensional

pore system of silica gel crystals grow larger than the average pore diameter albeit still within the broad pore size distribution at FWHM.

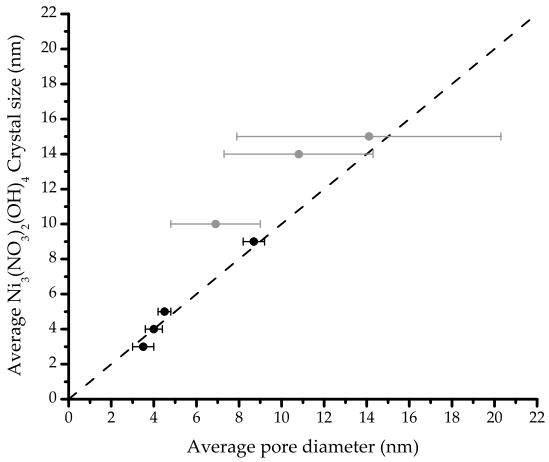


*Figure 9.* Relation between the average pore diameter and the average $Ni_3(NO_3)_2(OH)_4$ crystal size obtained after impregnation, and drying at 120 °C for ordered mesoporous (black) and conventional (grey) silica-supports. The error bars indicate the FWHM of the pore size distribution.

## Conclusions

Impregnation and drying of ordered mesoporous SBA-15 with $[Ni(OH_2)_6](NO_3)_2$ precursor solution was investigated. The impregnation step was studied using the cryo-TEM technique as this allowed imaging of the precursor solution in the wet impregnate. Many pores had remained empty after impregnation and patches were found outside the mesopores that pointed to extra-porous precursor solution. Freeze-drying of wet impregnate confirmed that the remaining precursor solution was present at the external surface of the SBA-15 particles.

After impregnation and drying at 120 °C, $Ni_3(NO_3)_2(OH)_4$ crystals with an average size of 9 nm were observed. TEM showed that many pores had not been filled with $Ni_3(NO_3)_2(OH)_4$, but agglomerates of precursor were no longer found outside the pores. By increasing the amount of impregnated precursor solution filling of almost all the pores could be reached without formation of large particles outside the pores. The absence of large exterior $Ni_3(NO_3)_2(OH)_4$ particles could be explained by transport of precursor during drying from the exterior into mesopores that were brought in contact with precursor upon impregnation. This resulted in filled pores with a higher loading than the anticipated 34 wt% as confirmed by quantitative electron tomography results.[29] Additional results with the less soluble and hydrolysis

sensitive $Cu(NO_3)_2.3H_2O$ salt also agreed with the proposed hypothesis as with this precursor large $Cu_2(OH)_2NO_3$ particles were found outside the pores. Supposedly due to the low solubility of copper nitrate hydroxide, transport into the pores was prevented.

Finally, experiments with both MCM-41 and conventional silica gel supports showed that crystal growth of $Ni_3(NO_3)_2(OH)_4$ was confined by the pore walls. Because of the narrow pore size distributions of the former supports, the crystallites in these systems had an average size that closely matched with the average pore diameter, whereas the latter led to an average crystal size slightly larger than the average pore diameter.

## Acknowledgments

Jos van Dillen is kindly thanked for his guidance and support. Hans Meeldijk is acknowledged for assistance with (cryo) STEM analysis.

## References

1. Chiola, V.; Ritsko, J.E.; Vanderpool, C.D. *U.S. Patent* No. 3,556,725 **1971**.
2. Kresge, C. T.; Leonowicz, M. E.; Roth, W. J.; Vartuli. J. C.; Beck, J. S. *Nature* **1992**, *359*, 710-712.
3. Beck, J.S.; Vartuli, J.C.; Roth, W.J.; Leonowicz, M.E.; Kresge, C.T.; Schmitt, K.D.; Chu, C.T- W.; Olson, D.H.; Sheppard, E.W.; McCullen, S.B.; Higgins, J.B.; Schlenker, J.L. *J. Am. Chem. Soc.* **1992**, *114*, 10834-10843.
4. Kresge, C.T.; Leonowicz, M.E.; Roth, W.J.; Vartuli, J.C. *U.S. Patent* No. 5,098,689 **1992**.
5. Beck, J.S. *U.S. Patent* No. 5,057,296 1991.
6. Grün, M.; Kurganov, A.A.; Schacht, S.; Schüth, F.; Unger, K.K. *J. Chromatogr. A.* **1996**, *740*, 1-9.
7. Mal, N.K.; Fuijwara, N.; Tanaka, Y. *Nature* **2003**, *421*, 350-353.
8. Díaz, J.F.; Balkus Jr, K.J. *J. Mol. Catal. B.* **1996**, *2*, 115-126.
9. Corma, A. *Chem. Rev.* **1997**, *97*, 2373-2419.
10. Ciesla, U.; Schüth, F. *Micropor. Mesopor. Mater.* **1999**, *27*, 131-149.
11. Taguchi, A.; Schüth, F. *Micropor. Mesopor. Mater.* **2005**, *77*, 1-45.
12. Maschmeyer, T., Rey, F., Sankar, G., Thomas, J. M., *Nature* **1995**, *378*, 159-162.
13. Maschmeyer, T. *Curr. Opin. Solid State Mater. Sci.* **1998**, *3*, 71-78.
14. Kim, J.M.; Kwak, J.H.; Jun, S.; Ryoo, R. *J. Phys. Chem.* **1995**, *99*, 16742-16747.
15. Ryoo, R.; Jun, S. *J. Phys. Chem. B* **1997**, *101*, 317-320.
16. Zhao, D.; Feng, J.; Huo, Q.; Melosh, N.; Fredrickson, G. H.; Chmelka, B. F.; Stucky, G. D. *Science* **1998**, *279*, 548-552.

17. Zhao, D.; Feng, J.; Huo, Q.; Feng, J.; Bradley, F.; Chmelka, B. F.; Stucky, G. D. *J. Am. Chem. Soc.* **1998**, *120*, 6024-6036.
18. Impéror-Clerc, M.; Davidson, P.; Davidson, A. *J. Am. Chem. Soc.* **2000**, 122, 11925-11933.
19. Ryoo, R.; Joo, S.H.; Jun, S. J. *Phys. Chem. B* **1999**, *103*, 7743-7746.
20. Attard, G.S.; Corker, J.M.; Göltner, C.G.; Henkde, S.; Templer, R.H. *Angew. Chem. Int. Ed.* **1997**, *36*, 315-317.
21. Tian, B.; Liu, X.; Yang, H.; Xie, S.; Yu, C.; Tu, B.; Zhao, D. *Adv. Mater.* **2003**, *15*, 1370-1374.
22. Tian, B.; Liu, X.; Solovyov, L.A.; Liu, Z.; Yang, H.; Zhang, Z.; Xie, S.; Zhang, F.; Tu, B.; Yu, C.; Terasaki, O.; Zhao, D. *J. Am. Chem. Soc.* **2004**, *126*, 865-875.
23. Bengoa, J.F.; Cagnoli, M.V.; Gallegos, N.G.; Alvarez, A.M.; Mogni, L.V.; Moreno, M.S.; Marchetti, S.G. *Micropor. Mesopor. Mater.* **2005**, *84*, 153-160.
24. Landau, M.V.; Varkey, S.P.; Herskowitz, M.; Regev, O.; Pevzner, S.; Sen, T.; Luz, Z. *Micropor. Mesopor. Mater.* **1999**, *33*, 149-163.
25. Khodakov, A.Y.; Zholobenko, V.L.; Bechara, R.; Durand, D. *Micropor. Mesopor. Mater.* **2005**, *79*, 29-39.
26. Janssen, A.H.; Yang, C.-M.;Wang, Y.; Schüth, F.; Koster, A.J.; De Jong, K.P. *J. Phys. Chem B* **2003**, *107*, 10552-10556.
27. Moreno, S.M.; Weyland, M.; Midgley, P.A.; Bengoa, J.F.; Cagnoli, M.V.; Gallegos,N.G.; Alvarez, A.M.; Marchetti, S.G. *Micron* **2006**, *37*, 52-56.
28. Impéror-Clerc, M.; Bazin, D.; Appay, M-D. ; Beaunier, P.; Davidson, A. *Chem. Mater.* **2004**, *16*, 1813-1821.
29. Friedrich, H.; Sietsma, J.R.A.; De Jongh, P.E.; Verkleij, A.J.; De Jong, K.P. *J. Am. Chem. Soc.* **2007**, *129*, 10249-10254.
30. Neimark, A.V.; Kheifez, L.I.; Fenelonov, V.B. *Ind. Eng. Chem. Prod. Res. Dev.* **1981**, *20*, 439-450.
31. Van Dillen, A.J.; Terörde, R.J.A.M.; Lensveld, D.J.; Geus, J.W.; De Jong, K.P. *J. Catal.* **2003**, *216*, 257-264.
32. Saibil, H.R. *Acta Crystallogr., Sect D: Biol. Crystallogr.* **2000**, **D56**, 1215-1222.
33. Jaroniec, M.; Kruk, M.; Olivier, J.P.; Koch, S. *Stud. Surf. Sci. Catal.* **2000**, *128*, 71-80.
34. Barrett, E.P.; Joyner, L.S.; Halenda, P.P. *J. Am. Chem. Soc.* **1951**, *73*, 373-380.
35. Harkins, W.D.; Jura, G. *J. Am. Chem. Soc.* **1944**, *66*, 1366-1373.
36. Lippens, B.C.; De Boer, J.H. *J. Catal.* **1965**, *4*, 319-323.
37. Thomas, J.M.; Midgley, P.A.; Yates, T.J.V.; Barnard, J.S. Raja, R.; Arslan, I.; Weyland, M. *Angew. Chem. Int. Ed.* **2004**, *43*, 6745-6747.
38. Fujdala, K.L.; Tilley, T.D. *J. Am. Chem. Soc.* **2001**, *123*, 10133-10134.
39. Ek, S.; Root, A.; Peussa, M.; Niinistö, L. *Thermochim. Acta* **2001**, *379*, 201-212.
40. Jentys, A.; Kleestorfer, K.; Vinek, H. *Micropor. Mesopor. Mater.* **1999**, *27*, 321-328.

41. Landmesser, H.; Kosslick, H.; Storek, W.; Fricke, R. *Solid State Ionics* **1997**, *101-103*, 271-277.
42. Llewellyn, P.L.; Schüth, F.; Grillet, Y.; Rouquerol, F.; Rouquerol, J.; Unger, K.K. *Langmuir* **1995**, *11*, 574-577.
43. Ottaviani, M.F.; Galarneau, A.; Desplantier-Giscard, D.; Di Renzo, F.; Fajula, F. *Micropor. Mesopor. Mater.* **2001**, *44-45*, 1-8.
44. Zhuravlev, L.T. *Langmuir* **1987**, *3*, 316-318.
45. Gallezot, P.; Prettre, M. *Bull. Soc. Chim. Fr.* **1969**, *2*, 407-411.
46. Estellé, J.; Salagre, P.; Cesteros, Y.; Serra, M.; Medina, F.; Sueiras, J.E. *Solid State Ionics* **2003**, *156*, 233-243.
47. D'Espinose de la Caillerie, J-B.; Kermarec, M.; Clause, O. *J. Am. Chem. Soc.* **1995**, *117*, 11471-11481.
48. Lekhal, A.; Glasser, B.J.; Khinast, J.G. *Chem. Eng. Sci.* **2001**, *56*, 4473-4487.
49. Knijff, L.M. *The Application of Active Components into Catalyst Support Bodies*, PhD thesis, Utrecht University **1993**.
50. Yue, W.; Zhou, W. *Chem. Mater.* **2007**, *19*, 2359-2363.
51. Yue, W.; Hill, A.H.; Harrison, A.; Zhou, W. *Chem. Commun.* **2007**, 2518-2520.
52. Sietsma, J.R.A.; Meeldijk, J.D.; Den Breejen, J.P.; Versluijs-Helder, M.; Van Dillen, A.J.; De Jongh, P.E.; De Jong, K.P. *Angew. Chem. Int. Ed.* **2007**, *46*, 4547-4549.
53. *HeteroGEneoUS Catalysis*, ed. De Jong, K.P.; Van Dillen, A.J., Department of Inorganic Chemistry, Utrecht University **1998**.
54. Van der Meijden, *Preparation and Carbon Monoxide Oxidation Activity of Supported Copper (oxide) Catalysts*, PhD thesis, Utrecht University **1981**.
55. Candal, R.J.; Regazzoni, A.E.; Blesa, M.A. *J. Mater. Chem.* **1992**, *2(6)*, 657-661.
56. Perelygin, Y.P.; Rashevskaya, I.V. *Russian J. Appl. Chem.* **2006**, *79*, 492-493.
57. Hidmi, L.; Edwards, M. *Environ. Sci. Technol.* **1999**, *33*, 2607-2610.
58. Henrist, C.; Traina, K.; Hubert, C.; Toussaint, G.; Rulmont, A.; Cloots, R. *J. Cryst. Growth* **2003**, *254*, 176-187.

# 3

# Impact of the thermal decomposition of silica supported nickel nitrate on the final NiO particle size and distribution

Although metal nitrates display many attractive properties as precursor, their use for the preparation of supported metal (oxide) catalysts by the impregnation and drying method often yields poor metal (oxide) dispersions. In this chapter we investigated the preparation of $Ni/SiO_2$ catalysts with aqueous $Ni(NO_3)_2.6H_2O$ precursor solutions. Ordered mesoporous silica SBA-15 (mesopore diameter of 9 nm) was used as model support system to study in detail the thermal treatments that are usually applied to convert the nitrate precursor into the desired metal (oxide). After impregnation and drying, 9 nm $Ni_3(NO_3)_2(OH)_4$ crystallites were found exclusively within the mesopores of SBA-15. Severe sintering and redistribution during calcination in air resulted in large NiO crystals outside of the mesopores, and rodlike NiO particles inside the mesopores. The degree of sintering depended on the concentration of $Ni_3(NO_3)_2(OH)_4$ decomposition products ($NO_2$, $N_2O$, $O_2$ and $H_2O$) and in particular $NO_2$ and $O_2$ were found to promote sintering and redistribution. Therefore, maintaining low concentrations of the latter components during the thermal nitrate decomposition is advocated. This was achieved by carrying out the treatment in the presence of $H_2$. The latter moderated that decomposition of $Ni_3(NO_3)_2(OH)_4$ into NiO and consequently the type of gaseous products formed, resulting in NiO particles of 3 nm on average at a loading of 24 wt%.

## Introduction

Supported metal (oxide) catalysts are essential for the production of fuels and chemicals. Nickel-based catalysts are amongst the most widely used because of their activity in many important (de)hydrogenation reactions.[1-3] The metal is deposited onto a support like $SiO_2$ or $Al_2O_3$ to achieve a high and thermally stable dispersion. Preparation techniques are primarily based on deposition of a precursor complex from the liquid phase and involve ion-adsorption[4,5], deposition-precipitation[6-8], and impregnation and drying[9-13]. Often, the latter method is preferred because of its simplicity and the limited production of waste. After impregnation of a porous support with a precursor-containing solution and subsequent drying, the product is typically heat treated in air (i.e. calcined) to convert the precursor into the desired metal oxide, or metal when followed by a high temperature reduction step with $H_2$.

State-of-the-art studies at low Ni loadings and strong precursor-support interactions have revealed much insight into the interplay between metal, ligands, counterions and supports, and their impact on the activity, selectivity and stability of the final catalyst.[8,11,12,14] Moreover, these studies have yielded fundamental insight into the importance of liquid-solid interactions between precursor solution and support on the formation of poorly reducible mixed Ni phases like aluminates[15] or phyllosilicates[16]. However, at Ni loadings well-above the ion-adsorption capacity of the support and with a weak precursor-support interaction, phenomena like redistribution and sintering during the successive (thermal) steps in the preparation can prevail. In this chapter we present a systematic study on the preparation of $Ni/SiO_2$ catalysts with loadings of 20 to 23 wt% prepared by the impregnation and drying method using aqueous $Ni(NO_3)_2.6H_2O$ precursor-solutions.

In principle $Ni(NO_3)_2.6H_2O$ is an attractive precursor of the active phase as its high solubility enables preparation of highly loaded Ni catalysts via a single-step impregnation. Moreover, it is cost-effective and pure NiO can be obtained because of the facile and complete removal of nitrate via thermal decomposition. Unfortunately, at loadings significantly higher than the support ion-adsorption capacity poorly dispersed Ni catalysts are often obtained. Poor metal dispersions and inhomogeneous distributions have been reported for a variety of metal nitrates amongst which that of cobalt[17,18], iron[19] and copper[20]. These results were obtained for both pre-shaped bodies (i.e. extrudates, pellets and sol-gel spheres) and powder supports.

Although $Ni(NO_3)_2.6H_2O$ was already used in 1910 for the preparation of $SiO_2$ and $Al_2O_3$ supported Ni catalysts[21], thus far little is known about the physico-chemical process(es) responsible for its poor metal dispersion when treated through drying, calcination and reduction. Moreover, little consensus is found amongst the reported studies. Some authors have stated that prevention of redistribution during drying is the key to obtain a highly dispersed and homogeneously distributed metal (oxide) phase. These findings are mainly based on comparison of extrudates, spheres or pellets that were impregnated and dried using a metal nitrate (e.g. Ni or Fe) or citrate salt, and on the addition of polysaccharide carbohydrates (e.g. hydroxyethylcellulose)

to $Cu(NO_3)_2.3H_2O$ precursor solutions.[19,22-25] These studies indicated that the use of chelating salts or the addition of viscosity-increasing agents to aqueous nitrate solutions prevented the formation of egg-shell type distributions. Besides homogeneous precursor distributions, the metal dispersion of the final catalyst was also found to increase largely with these chelating precursor salts. Lensveld and others showed that these findings could be transferred to powder supports.[22,23] The effectiveness of these chelating precursors is ascribed to three phenomena. Firstly, a sharp increase in viscosity due to gelation of the precursor solution upon drying inhibits migration. Secondly, the poor crystallization behaviour of these salts presumably limits redistribution due to absence of fast crystal growth, and thirdly, enhanced interaction of the covering layer with the support via hydrogen bonding.[25]

Other studies indicated that with metal nitrates a poor dispersion is obtained due to sintering during calcination at temperatures between 200 – 600 °C.[26-31] Poels *et al.* concluded for $Ni/Al_2O_3$ that a high concentration of $NO_x$ and/or $H_2O$ decomposition products during calcination had a detrimental effect on the ultimate dispersion.[27,28] Reinalda and Kars found similar results for $Co/SiO_2$ and used this property to obtain a more sintered Co metal phase.[29] In addition, van de Loosdrecht *et al.* investigated the air space velocity and heating rate effects during calcination of supported $Co(NO_3)_2.6H_2O$ on the performance of the final Co catalysts in the Fischer-Tropsch synthesis, and observed that a low concentration of gaseous decomposition products led to more active catalysts.[30] On the other hand Louis *et al.* suggested, for $Ni/SiO_2$, that large particles are probably formed due to the partial decomposition during calcination of phyllosilicate anchoring sites for Ni.[31] Unfortunately, these studies have not disentangled the impact of the drying treatment on the dispersion on the one hand, and the influence of specific decomposition product(s) (e.g. $O_2$, $H_2O$, NO, $NO_2$ and $N_2O$) on the sintering process during calcination, on the other hand.

The inconclusiveness regarding identification of the most detrimental process to the ultimate metal dispersion can be largely ascribed to limitations in techniques available to monitor the dispersion and distribution of precursor compounds on conventional supports. Many characterisation techniques require special pre-treatments; for instance insight into the dispersion by chemisorption can only be obtained after reduction of the precursor to the metal phase. Powder X-ray diffraction (XRD) renders an average crystallite size only if the precursor phase is crystalline. Electron microscopy gives direct information on the precursor distribution over the support combined with particle size distributions. Unfortunately, the heterogeneity of conventional supports makes it cumbersome to obtain detailed information with this technique. A possibility to overcome these problems is at hand since the discovery in the early nineties of a new type of materials, namely ordered mesoporous materials prepared via a templating mechanism.[32] Nowadays, a wide variety of ordered mesoporous materials is available. We propose that these supports provide model systems to study the individual steps in catalyst preparation. Especially for mesoporous silicas like MCM-41[32] and SBA-15[33], pore size and geometry are

uniform, well-defined and variable over a wide range. These properties make it possible to obtain much more detailed information from Transmission Electron Microscopy (TEM), as a clear differentiation can be made between precursor and support. Furthermore, the uniform pore system enables one to derive more detailed information from $N_2$-physisorption experiments. Particle growth inside the mesoporous channels during preparation can be monitored as the degree of (partial) pore blocking by these guest phase particles is displayed in the desorption branch of the isotherm.[34-36] An additional advantage of the uniform pore size involves the prevention of extensive migration of precursor during drying because differences in capillary suction between pores are lacking.[37] As a result studies on the separate effect of impregnation, drying and thermal treatments on the ultimate metal dispersion become within reach.

In this chapter, we demonstrate the potential of ordered mesoporous supports as model support systems for studying individual steps in catalyst preparation, but focus on the impact of the thermal treatments used to bring about the active component. We show that using silica-based SBA-15 we can identify the impact of individual treatments on the dispersion and distribution of the active phase or its precursor over the support. Moreover, results obtained with silica gel indicated that these findings are also relevant for conventional supports.

## Experimental

*Sample preparation*

SBA-15 (pore volume= 0.80 ml.g$^{-1}$ and average pore diameter= 9 nm) was prepared following the procedure of Zhao and co-workers.[33] 8 g $PEO_{20}PPO_{70}PEO_{20}$ (PEO= poly(ethylene oxide) and PPO= poly(propylene oxide)) tri-block copolymer (Aldrich) was dissolved in 250 ml demineralised water of 40 °C. After the solution had become clear, 48 g of concentrated HCl (Merck) was added, followed by the addition of 21.5 ml of tetraethyl orthosilicate (Acros). The mixture was stirred for 20 hours at 40 °C and then transferred to an oven for further reaction at 80 °C for 48 hours. The solid product was collected from the suspension by filtration, washed, dried in air for 12 hours at 80 °C and calcined for 6 hours at 550 °C. Davicat 1404 silica gel (pore volume=0.90 ml.g$^{-1}$ and average pore diameter= 7 nm) was used as received from Grace-Davison. The 4.2 M precursor solution was prepared by dissolving $Ni(NO_3)_2.6H_2O$ (Acros) in demineralised water. SBA-15 and silica gel were impregnated to incipient wetness in static vacuum using 1 and 1.25 ml.g$^{-1}$ of the precursor solution to provide 20 wt% and 24 wt% Ni metal loadings, respectively. Prior to impregnation, the supports were dried for 2 hours in dynamic vacuum at 80 °C to remove physisorbed water. SBA-15 was also impregnated using a 1.35 M anhydrous $Ni(NO_3)_2$ solution. This solution was prepared by dissolving $Ni(NO_3)_2.6H_2O$ in dry ethanol. Subsequently, the water present was removed by reaction with ethyl orthoformate to form ethanol and ethyl formate.[38] The latter

component was removed by vacuum distillation. The impregnates were dried in static air by increasing the temperature from room temperature to 120 °C at a controlled rate of 1 °C.min$^{-1}$ and were kept at that temperature for 12 hours. The sample impregnated with the anhydrous $Ni(NO_3)_2$ solution was dried using a dry argon flow (50 ml.min$^{-1}$) instead of static air. Calcination treatments were carried out using a plug flow reactor (length 17 cm and diameter 1 cm) and varying air flows of 0-100 ml.min$^{-1}$ by heating approximately 40 mg of the dried samples from room temperature to 450 °C with a ramp of 1 °C.min$^{-1}$. The samples were kept at 450 °C for 4 hours. Some samples were thermally treated in He with flows of 50 or 100 ml.min$^{-1}$. Thermal treatments in He diluted gas streams of $NO_2/O_2$ (10/3 vol%), or $H_2O$ (15 vol%) were performed with a flow of 50 ml.min$^{-1}$. Calcination under stagnant conditions was carried out by heating 0.25 g of dried impregnate S/D in an oven dish (volume 0.062 dm$^3$) with a loose lid on top to retard removal of the decomposition products. For calcination of the anhydrous $Ni(NO_3)_2$ sample, the applied air flow (100 ml.min$^{-1}$) was dried using a molsieve filter. For calculation of the gas-hourly-space-velocities (GHSV) apparent bulk densities of 0.46 and 0.09 g.cm$^{-3}$ were used for silica gel and SBA-15, respectively.

Reduction treatments were performed by heating the dried samples to 600 °C with a ramp of 5 °C.min$^{-1}$, while a 5 vol% $H_2$/Ar flow of 50 ml.min$^{-1}$ was passed through the sample bed. The reduced samples were passivated via controlled exposure to air.

All samples were labelled using codes. An example of a code is S/D-C-R. The first part denotes the support: S= SBA-15 and G= silica gel support. The second part indicates the heat treatments that were applied: D= dried, C= thermally treated in air (i.e. calcined) and R= reduction treatment.

*Characterisation*

$N_2$-physisorption measurements were performed at -196 °C, using a Micromeritics Tristar 3000 apparatus. The samples were dried in He flow for 14 hours at 120 °C prior to analysis. The pore size distribution was derived from the adsorption branch of the isotherm using non-local density functional theory (NL-DFT). A model developed by Jaroniec *et al.*[39] for ordered mesoporous silica supports with cylindrical pore geometry was used. This model showed to provide a reliable representation as the data depended only slightly on the regularisation constraint. The pore diameter of the mesoporous channels of SBA-15 was defined by the value at which the maximum in differential pore volume was observed. The micro- and meso-porosity were defined as the volume present in pores ≤2 nm, and between 2-50 nm, respectively. There is no standard method yet for the determination of blocked mesopore volume ($V_{meso,bl}$). We used the BJH theory[40] with the Harkins and Jura[41] thickness equation and the Kruk-Jaroniec-Sayari correction[42] for ordered mesoporous siliceous materials to calculate from the desorption branch the cumulative pore volume as a function of the pore size. From this we determined the total amount of $V_{meso,bl}$ considering that the pores with a diameter of 2 to 5 nm are due to volume in (partially) blocked pores.

Finally, mesopore and external surface areas were determined with the t-method[43] using thickness ranges of 0.35-0.55 and 1.00-1.41 nm, respectively.

Powder X-ray diffraction (XRD) patterns were obtained at room temperature from 5 to 90° 2θ with a Bruker-AXS D8 Advance X-ray Diffractometer setup using Co-$K_{\alpha 12}$ radiation. Low-angle diffraction patterns (0.5 – 5° 2θ) were recorded using a zero-background Si sample holder obtained from Bruker-AXS. The average $Ni_3(NO_3)_2(OH)_4$, NiO and Ni crystallite sizes were calculated according to the Scherrer equation using the most intense peaks at 2θ = 14.9°, 50.8° and 52.2°, respectively. *In situ* XRD experiments were carried out to study the thermal decomposition of sample S/D in air or in 5 vol% $H_2$/He flow (100 ml.min$^{-1}$). To this end the diffractometer was equipped with an Anton-Paar XRK reaction chamber. The samples (~20 mg) were heated to 248 °C with a ramp of 1 °C.min$^{-1}$ and kept at 248 °C till decomposition had completed. XRD patterns were recorded from 10 to 65° 2θ.

Scanning transmission electron microscopy (STEM) images were obtained using a Tecnai 20 microscope operating at 200 kV and equipped with a High-Angle Annular Dark-Field (HAADF) detector (camera length: 120 mm). With this technique the precursor phase can be better discriminated from the $SiO_2$ support because of the Z-contrast.[44]

Thermogravimetric analysis (TGA) was carried out using a Perkin-Elmer Pyris 1 apparatus. Typically a quantity of 5 mg sample was heated from room temperature to 500 °C (ramp= 5 °C.min$^{-1}$) in an air, Ar, or 5 vol% $H_2$/Ar gas flow of 100 ml.min$^{-1}$. During the TGA experiments mass spectra of the gaseous products in the off gas were simultaneously recorded with a Pfeiffer Omnistar quadrupole mass spectrometer. The *m*/*z* values (*m* = molar mass of X*z*+ ion, *z*= charge of the ion) for which the ion currents were recorded are: 14, 15, 16, 17, 18, 28, 30, 32, 44, 46, 62 and 63.

## Results and discussion

*Conventional silica gel*

First the impregnation and drying steps in the preparation of conventional Ni/$SiO_2$ catalysts were studied using silica gel powder as support. After incipient wetness impregnation with an aqueous $Ni(NO_3)_2.6H_2O$ solution (4.2 M) the sample was dried in air at 120 °C to yield a light-green product that was labelled G/D. XRD results (Figure 1) showed that nickel nitrate hydroxide with composition $Ni_3(NO_3)_2(OH)_4$ had formed. Formation of these so-called basic nickel nitrates upon heating of $Ni(NO_3)_2.6H_2O$ has been described[45,46] and its structure resembles that of $Ni(OH)_2$. Line-broadening analysis of the (001) diffraction line showed that the crystallites had an average size of 12 nm. The crystal phases and average crystallite sizes found with XRD for all samples are summarised in Table 1 together with the particle size distributions derived from STEM results.

Calcination at 450 °C of the dried impregnate G/D yielded a grey product designated G/D-C with a NiO/$SiO_2$ loading of 28 wt%. Its diffraction pattern

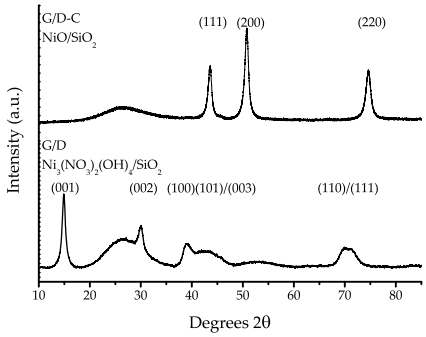


*Figure 1.* XRD patterns of silica gel supported sample obtained after impregnation with $[Ni(OH_2)_6](NO_3)_2$ solution, followed by drying at 120 °C (G/D), and sample G/D-C obtained after subsequent calcination in air at 450 °C.

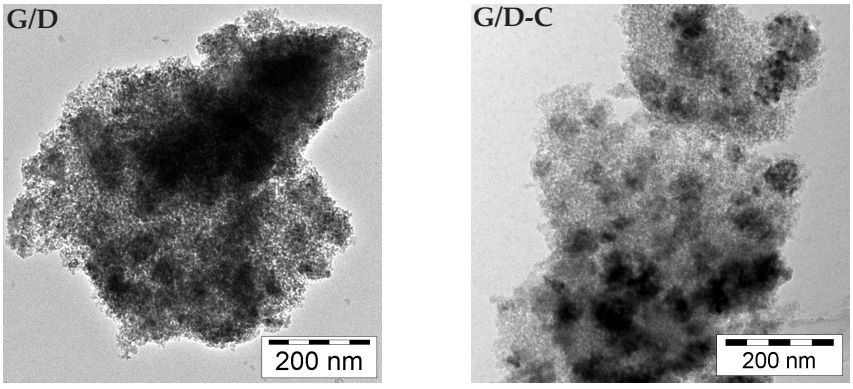


*Figure 2.* STEM images of silica gel supported sample obtained after impregnation with $[Ni(OH_2)_6](NO_3)_2$ solution, followed by drying at 120 °C (G/D), and sample G/D-C obtained after subsequent calcination in air at 450 °C.

(Figure 1) demonstrated that the crystalline $Ni_3(NO_3)_2(OH)_4$ phase had completely decomposed during the thermal treatment to form NiO crystals of 15 nm on average. The grey colour of the sample is most likely due to some deviation from ideal 1:1 stoichiometry of the NiO. Taking into account the density increase upon conversion of $Ni_3(NO_3)_2(OH)_4$ (~3.5 g.cm$^{-3}$) into NiO (6.7 g.cm$^{-3}$), and assuming no change in crystal geometry, the observed increase from 12 to 15 nm was unexpected. This suggested that some sintering had taken place during calcination. Both dried (G/D) and air calcined (G/D-C) samples were characterised using STEM, and typical images are depicted in Figure 2, respectively. The image of the dried sample G/D demonstrated that it is difficult to distinguish the $Ni_3(NO_3)_2(OH)_4$ precursor from the support. This

is due to both the low contrast between precursor and support and the heterogeneity of the support. It was not possible to derive an average $Ni_3(NO_3)_2(OH)_4$ particle size, or to determine its distribution over the support. Figure 2 shows that also after calcination limited information could be obtained despite the enhanced contrast of the NiO over the $SiO_2$ support. NiO domains could be distinguished, and a rough estimate provided 7-70 nm for their size range, which also suggested that severe sintering had taken place. Finally, from the results of sample G/D-C-R collected in Table 1 suggested that the reduction step to bring about the Ni metal phase had little impact on poor dispersion and distribution that was obtained after air calcination.

*Table 1.* Overview of applied thermal treatments and, XRD and STEM results of samples.

| Samples | Thermal treatments | Nickel phase | Loading (wt%) | Size (nm) | |
|---|---|---|---|---|---|
| | | | | $d_{XRD}$ | $d_{TEM}$ |
| **Silica gel** | | | | | |
| G/D | drying | $Ni_3(NO_3)_2(OH)_4$ | 39 | 12 | - |
| G/D-C | drying/calcination | NiO | 28 | 15 | 7-70 |
| G/D-C-R | drying/calcination/reduction | Ni | 23 | 17[a] | 10-35 |
| G/D-R | drying/reduction | Ni | 23 | 4[a] | 3-8 |
| **SBA-15** | | | | | |
| S/D | drying | $Ni_3(NO_3)_2(OH)_4$ | 34 | 9 | - |
| S/D-C | drying/calcination | NiO | 24 | 10 | 10-35 |
| S/D-C-R | drying/calcination/reduction | Ni | 20 | 12[a] | 5-25 |
| S/D-$C_s$ | drying/calcination (stagnant air) | NiO | 24 | 25 | 50-200 |
| S/D-$C_{NC}$ | drying/calcination (natural convection) | NiO | 24 | 11 | 20-100 |
| S/D-R | drying/reduction | Ni | 20 | 3[a] | 3-6 |
| S/D-$C_{air}$ | drying/calcination | NiO | 24 | 9 | 10-40 |
| S/D-$C_{He}$ | drying/heat treatment in He | NiO | 24 | 7 | 10-25 |
| S/D-$C_{anh}$ | drying/calcination (dry air) | NiO | 9 | 8 | 10-25 |
| S/D-$C_{H2O}$ | drying/heat treatment 15 vol% $H_2O$/He | NiO | 24 | 6 | 6-10 |
| S/D-$C_{NO2}$ | drying/heat treatment 10/3 vol% $NO_2/O_2$/He | NiO | 24 | 16 | 20-90 |

[a]underestimated size due to re-oxidation of Ni prior to XRD analysis.

*Ordered mesoporous silica*

Next, an ordered mesoporous $SiO_2$ was employed to address the impact of each step in the preparation on the final Ni metal dispersion and distribution over the support. After incipient wetness impregnation of SBA-15 with an aqueous 4.2 M $Ni(NO_3)_2.6H_2O$ solution and subsequent drying at 120 °C, a greenish product was obtained. Figure 3 shows STEM images of pristine SBA-15 and the dried impregnate labelled S/D, respectively. Comparison between pristine SBA-15 and sample S/D suggested that the $Ni_3(NO_3)_2(OH)_4$ had been deposited exclusively inside the mesopores as no particles or agglomerates were observed outside the mesopores. XRD supported these findings as an average $Ni_3(NO_3)_2(OH)_4$ crystal size of 9 nm was found, which was in good agreement with the mesopore diameter (9 nm) and indicated confinement by the pore walls. Additional HAADF-STEM tilt series of individual SBA-15 particles (not shown) demonstrated that a significant part of the

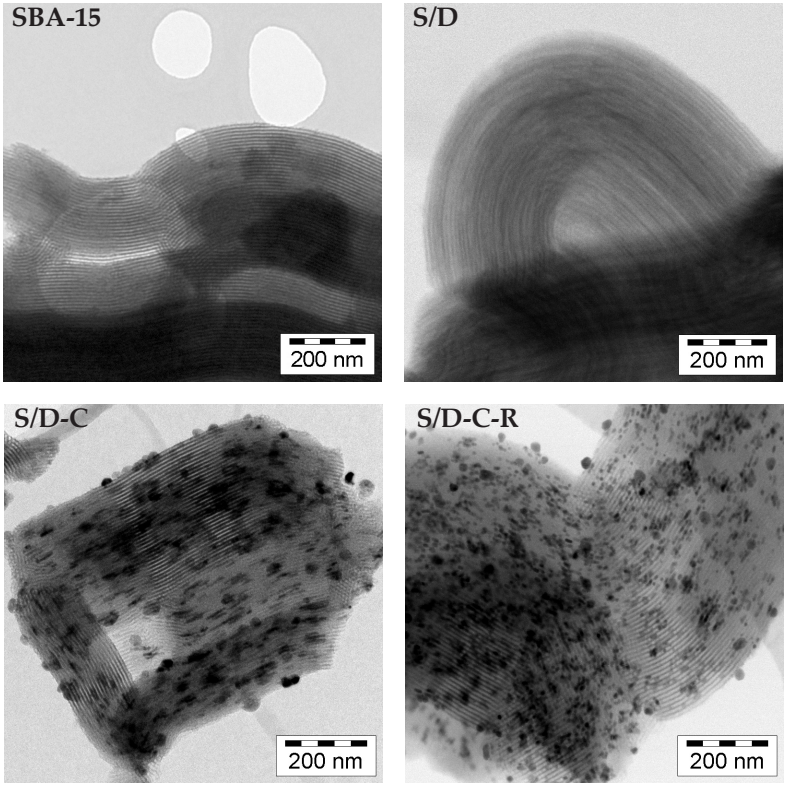


*Figure 3.* STEM images of pristine SBA-15, and SBA-15 after impregnation with $[Ni(OH_2)_6](NO_3)_2$ solution, followed by drying at 120 °C (S/D), subsequent calcination in air at 450 °C (S/D-C) and finally reduction in 5 vol% $H_2$/Ar at 600 °C (S/D-C-R).

mesopores had not been filled with precursor. We refer to chapter 2 for more in depth information on this issue. Hence, after drying incomplete filling of the mesopores was observed, however, the filled pores contained well-dispersed $Ni_3(NO_3)_2(OH)_4$.

In Figure 4 the $N_2$-physisorption isotherms of pristine SBA-15 and samples S/D, S/D-C and S/D-C-R are shown. Details of the textural properties derived from these isotherms are given in Table 2 together with those obtained for the other samples used in this study. The physisorption results were corrected for the contribution of precursor to the total weight of the sample and expressed per gram of $SiO_2$. The isotherm of the unloaded SBA-15 is typical for this material: a high onset at low relative pressures originating from the intra-wall microporosity, and hysteresis at higher values because of the mesoporous channels. The small relative pressure region ($p/p_o$ = 0.69 – 0.71) in which the single-step capillary condensation took place is a consequence of the uniform mesopore diameter of 9 nm. Impregnation of the support with aqueous $Ni(NO_3)_2.6H_2O$ solution followed by drying (Table 2, sample S/D) led to a decrease in total pore volume ($V_{tot,exp}$) to 0.47 $cm^3.g_{SiO2}^{-1}$, while a decrease to 0.63 $cm^3.g_{SiO2}^{-1}$ was expected ($V_{tot,calc}$). The desorption branch of the isotherm contained a new feature in the relative pressure region of 0.45 to 0.6, namely delayed closure of the hysteresis loop. Since the adsorption branch did not show capillary

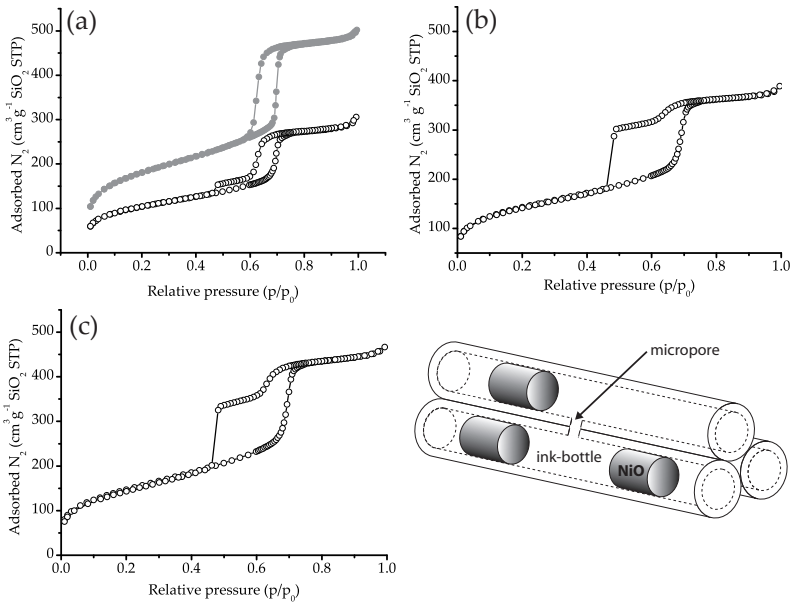


*Figure 4.* $N_2$-physisorption isotherms of pristine SBA-15 (grey) and dried impregnate S/D (a), air calcined product S/D-C (b), reduced sample S/D-C-R (c), and a schematic representation of the ink-bottle pores formed by the rod-like NiO particles inside the mesopores with the intra-wall micropores as pore neck.

*Table 2.* Overview of $N_2$-physisorption results of SBA-15 supported samples.

| Sample | Surface area ($m^2.g_{SiO2}^{-1}$) | | Porosity ($cm^3.g_{SiO2}^{-1}$) | | | | | |
|---|---|---|---|---|---|---|---|---|
| | $S_t$ [a] | $S_{t,ext}$ [b] | $V_{tot,calc}$ [c] | $V_{tot,exp}$ [d] | $V_{micro}$ [e] | $V_{meso}$ [f] | $V_{meso,bl}$ [g] | (%) |
| SBA-15 | 516 | 38 | 0.78 | 0.78 | 0.05 | 0.68 | 0.00 | 0 |
| S/D | 293 | 33 | 0.63 | 0.47 | 0.01 | 0.42 | 0.08 | 19 |
| S/D-C | 409 | 31 | 0.73 | 0.66 | 0.06 | 0.56 | 0.42 | 75 |
| S/D-C-R | 487 | 45 | 0.75 | 0.72 | 0.01 | 0.67 | 0.46 | 69 |
| S/D-$C_s$ | 474 | 40 | 0.75 | 0.64 | 0.03 | 0.57 | 0.24 | 42 |
| S/D-$C_{NC}$ | 388 | 33 | 0.73 | 0.65 | 0.04 | 0.56 | 0.15 | 27 |
| S/D-R | 375 | 32 | 0.73 | 0.61 | 0.05 | 0.53 | 0.24 | 45 |
| S/D-$C_{air}$ | 384 | 30 | 0.73 | 0.60 | 0.06 | 0.50 | 0.40 | 80 |
| S/D-$C_{He}$ | 442 | 34 | 0.73 | 0.59 | 0.03 | 0.51 | 0.29 | 57 |
| S/D-$C_{anh}$ | 304 | 23 | 0.76 | 0.44 | 0.02 | 0.39 | 0.30 | 77 |
| S/D-$C_{H2O}$ | 376 | 34 | 0.73 | 0.53 | 0.04 | 0.46 | 0.21 | 46 |
| S/D-$C_{NO2}$ | 280 | 24 | 0.73 | 0.44 | 0.03 | 0.38 | 0.25 | 66 |

[a]mesopore surface area determined using t-method; [b]external surface area calculated using t-method; [c]expected total pore volume based on contribution of Ni precursor to volume decrease; [d]total pore volume based on amount $N_2$ adsorbed at $p/p_o$=0.995; [e]micropore volume calculated using NL-DFT; [f]mesopore volume calculated using NL-DFT; [g]partially blocked mesopore volume calculated from desorption branch (see experimental section for details).

condensation effects at these values, this feature could be associated with ink-bottle type pores[34-36] formed by filling of the mesopores of SBA-15 with $Ni_3(NO_3)_2(OH)_4$. This partially blocked mesopore volume ($V_{meso,bl}$) was found to be 19% of the total accessible mesoporosity. Since the porosity of sample S/D was significantly lower than expected we investigated the stability of the ordered structure of the SBA-15 support upon impregnation and drying. We compared the long-range order of the mesopores of sample S/D to that of pristine SBA-15 with low-angle XRD (Figure 5). Both patterns contain three well-resolved diffraction lines that could be indexed as the (100), (110) and (200) lattices of a unit cell with a hexagonal symmetry, which is typical for SBA-15.[33] Taking a closer look at the 2θ region from 2.2 up to 4.0 as shown in the insert for sample S/D, the (210) and (300) diffraction lines could be identified too. Especially the presence of the latter diffractions in both patterns, and the relatively high ratio between the (110) and (200), and the (100) lines demonstrated on the one hand that high-quality SBA-15 was synthesised, and on the other hand that the impregnation and drying steps had not significantly affected the long-range

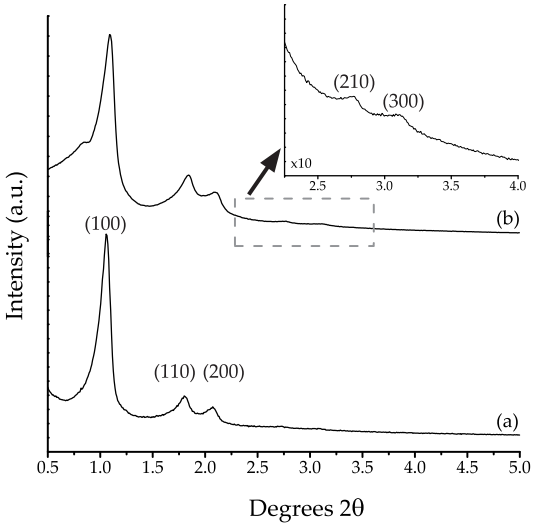


*Figure 5.* Low-angle XRD patterns of pristine SBA-15 (a) and $Ni_3(NO_3)_2(OH)_4$/SBA-15 sample S/D obtained after impregnation and drying (b).

order of the mesopores. Hence, we concluded that the decreased porosity was due to the formation of inaccessible domains in the sample.

XRD results of the air calcined sample S/D-C (Table 1) showed that NiO crystallites with an average size of 10 nm had formed. Similar to the results found with silica gel this suggested sintering as the crystal size did not decrease as expected from the density increase upon conversion of $Ni_3(NO_3)_2(OH)_4$ into NiO. STEM analysis (Figure 3) demonstrated that the precursor phase had severely sintered upon calcination in air. Two types of NiO particles could be distinguished. The first type consisted of large NiO particles of 10-35 nm localised at the exterior surface of the SBA-15 particles, whereas the second type appeared not to have been transported over such large distances and was retained inside the mesopores. The latter particles appeared to have adopted a rodlike geometry suggesting that the diameter of these was restricted by the pore walls. $N_2$-physisorption (Figure 4 and Table 2) showed that the total porosity had increased compared to sample S/D as expected because of the decreased volume and the location of the NiO phase. In addition, the micro porosity was close to its original value. Finally, the quantity of $N_2$ released from ink-bottle type pores during desorption had significantly increased from 19% to 75% going from sample S/D to sample S/D-C due to the formation of rodlike NiO particles inside the mesopores.

The final step in the preparation was carried out by reducing the SBA-15 supported NiO in a stream of 5 vol% $H_2$/Ar to Ni metal (sample S/D-C-R). XRD analysis disclosed that the catalyst had an average Ni crystallite size of 12 nm, which

is a slight underestimation as the outer-shell of the particles had been re-oxidised during passivation. STEM results (Figure 4) demonstrated that little had changed with respect to the distribution of the active phase over the support, and particles with sizes ranging from 7 to 25 nm were observed. $N_2$-physisorption (Table 2) demonstrated that the microporosity decreased, whereas the mesoporosity increased. The percentage of the ink-bottle type of pores (69%) had hardly changed during reduction. The total pore volume (0.72 $cm^3.g_{SiO2}^{-1}$) was close to its expected value of 0.75 $cm^3.g_{SiO2}^{-1}$. Finally, comparison of the pore size distribution plots (not depicted) obtained from the adsorption branch of the isotherms of each dried, calcined and reduced sample with that of pristine SBA-15 demonstrated that the impregnation and drying technique, and thermal treatments used to convert the precursor into the desired Ni metal had little effect on the pore diameter of the accessible mesopores of SBA-15.

After studying the SBA-15 products obtained after each step in the preparation we could unambiguously conclude that the calcination treatment in air had the most detrimental effect on the final metal dispersion and distribution over the silica support. Results obtained with a catalyst prepared via a synthesis route that modified this step further supported our findings. Dried impregnate sample S/D was thermally treated in a diluted stream of 5 vol% $H_2$/Ar to obtain a Ni/SBA-15 catalyst labelled S/D-R. XRD showed an average Ni crystal size of 3 nm had formed. From this it is likely that the Ni crystallites had a size of 4 to 5 nm. STEM results (Figure 6) confirmed that the Ni particles were small (3 to 6 nm) and rather homogeneously distributed throughout the mesopores of SBA-15. No Ni particles were observed at the external surface of the SBA-15 particles. Thus, the homogeneous distribution over the support after drying with sample S/D could be retained by avoiding the air calcination treatment. $N_2$-physisorption showed that the degree of pore blocking was significantly lower (42%) than for the sample S/D-C-R (69%) prepared via the

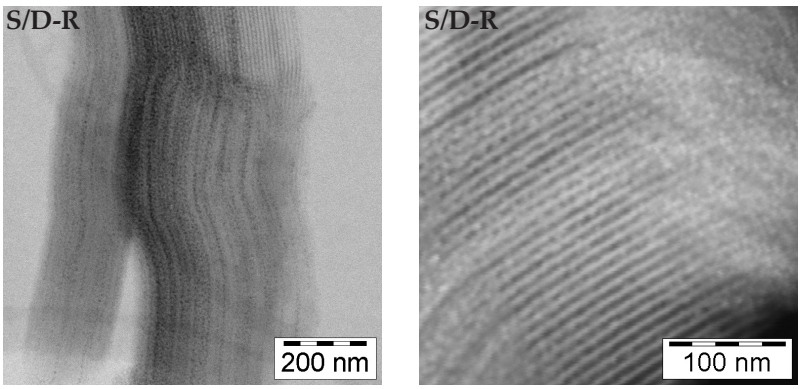


*Figure 6.* STEM (a) and HAADF-STEM (b) images of sample S/D that was heat treated at 600 °C in a 5 vol% $H_2$/Ar flow to yield Ni/SBA-15 sample S/D-R.

route including the calcination step. Also the total porosity was lower compared to that of S/D-C-R, supposedly due to the larger fraction of Ni particles inside the mesopores.

*Detailed investigation of the air calcination treatment*

Since the air calcination step had clearly proven to have an unfavourable impact on the final dispersion of the catalyst we studied this step in more detail. With TGA coupled with mass-spectrometry (MS) we monitored the weight loss and the type of gaseous products formed during air calcination of SBA-15 supported $Ni_3(NO_3)_2(OH)_4$. The measured weight loss curve is shown in Figure 7. The weight loss starting at 40 °C was predominantly caused by the removal of physisorbed water from the surface of the SBA-15 support. Other TGA and solid-state $^1$H-MAS-NMR spectroscopy studies have shown that the removal of physisorbed water is completed at approximately 200 °C.[47,48] At higher temperatures dehydration is predominantly caused by dehydroxylation of the silica surface, although in the $Ni_3(NO_3)_2(OH)_4$/SBA-15 system some dehydration of the precursor phase could take place too. More extensive weight loss started gradually at ~220 °C, which rapidly increased at higher temperatures and was completed at ~310 °C. The weight loss of 13% in this range matched the expected loss due to conversion of the $Ni_3(NO_3)_2(OH)_4$ into NiO. On the one hand this indicated that decomposition had completed at 310 °C, and on the other hand it showed that during the drying treatment of the impregnate, $Ni(NO_3)_2.6H_2O$ had been entirely converted into$Ni_3(NO_3)_2(OH)_4$. Further heating of the sample to the final temperature of 500 °C led to a gradual weight loss of 2% due to dehydroxylation of the support and conversion of non-stoichiometric $NiO_x$ into pure NiO[49]. Experiments with a heating rate of 1 °C.min$^{-1}$ showed similar results, although decomposition had already completed at 280 °C.

The MS signals of gaseous products that were found to evolve during calcination have been plotted as a function of the temperature (Figure 8). It should be noted that signals due to the mass fractions 15 ($NH^+$) and 62/63 ($NO_3^+$/$HNO_3^+$) typical for $NH_3$ and $HNO_3$, respectively, were not observed. The observed mass fraction 18 ($H_2O^+$) originated from $H_2O$. The presence of the $NO_2^+$ fraction ($m/z$ = 46) demonstrated that a significant amount of $NO_2$ evolved. Correction of the $NO_2^+$ (37%) and $NO^+$ (100%) intensities for their relative abundance indicated that the latter fraction also originated from $NO_2$. Finally, $m/z$= 44 could be associated with both $CO_2$ and $N_2O$. With GC analysis (not shown) of the gaseous products we established that $N_2O$ and not $CO_2$ evolved. Recently, Małecki *et al.* reported for bulk $Ni(NO_3)_2.6H_2O$ that $N_2O$ contributes to 5-8 wt% of the total nitrogen content released during decomposition.[50] Although our MS results did not allow quantification, they indicated that the concentration of $N_2O$ was much lower than that of $NO_2$. Next to $H_2O$ and $NO_2$, $O_2$ was expected to form. However, the relatively small amounts of this compound could not be detected since decomposition of the SBA-15 supported $Ni_3(NO_3)_2(OH)_4$ was carried out in air. Therefore, we also decomposed sample S/D through heating in an Ar atmosphere and monitored the evolved gasses with MS (Figure 8). Next to

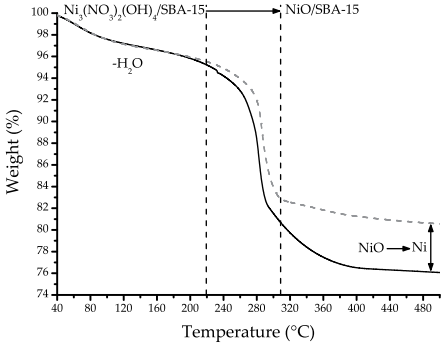


*Figure 7.* TGA results obtained during calcination in air flow (broken line) or heat treatment in 5 vol% $H_2$/Ar flow (black line) of dried impregnate S/D.

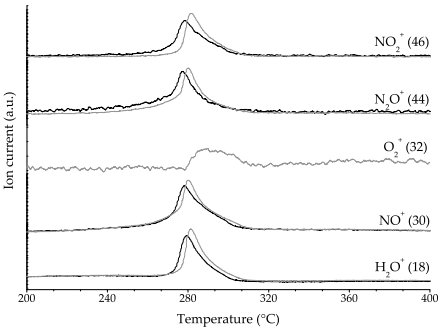


*Figure 8.* MS results of the off gas during calcination in air flow (black lines) or heat treatment in Ar flow (grey lines) of dried impregnate S/D.

the expected products, $O_2$ (*m*/*z*= 32) was detected albeit in low concentrations. Hence, the decomposition products of supported $Ni_3(NO_3)_2(OH)_4$can be largely accounted for by equation 1:

$$Ni_3(NO_3)_2(OH)_4\ (s) \longrightarrow 3NiO\ (s) + 2NO_2\ (g) + 2\ H_2O\ (g) + ½\ O_2\ (g) \qquad (1)$$

*Influence of the gaseous decomposition products*

To study the impact of the gaseous decomposition products on the transformation of $Ni_3(NO_3)_2(OH)_4$ into NiO a series of experiments was carried out using different gas atmospheres and calcination conditions. First, the impact of the concentration of decomposition products was investigated by calcination in air flow of sample S/D using different GHSV values during heating. In Figure 9 the impact of the GHSV on the average and spread in NiO particle sizes found at the exterior surface of the SBA-15 particles as determined by STEM (left axis) is given. Also included are the results for sample S/D-$C_S$ that was obtained by calcination in stagnant air. Moreover, two STEM images of this sample are depicted in Figure 10 that demonstrates the impact on the migration out of the mesopores when maintaining a high partial pressure of the gaseous decomposition products. The results given in Figure 9 showed that going from calcination in stagnant air to natural convection (GHSV= 0 $h^{-1}$) led to decrease of a factor of two in the average NiO particle size. Moreover, the spread in NiO particle sizes had significantly narrowed. Maintaining a GHSV of about 3,300 $h^{-1}$ resulted in a similar NiO particle size reduction. Increasing the GHSV resulted in a further decrease of the average particle size, but the spread in the particle sizes remained rather constant. Also shown in Figure 9 (right axis) is the effect of the applied GHSV on the degree of mesopore blockage by the rodlike NiO particles that retained inside the SBA-15 particles as calculated from $N_2$-physisorption. The results confirmed the

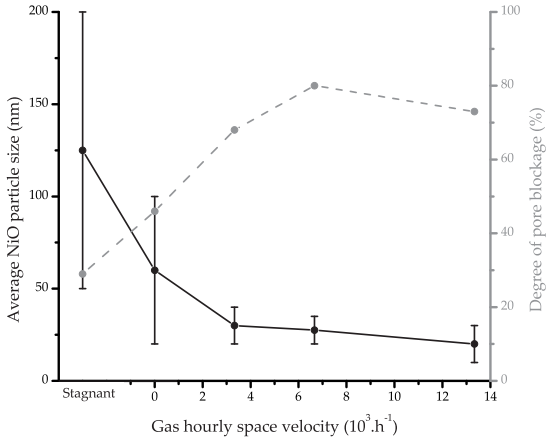


*Figure 9.* Influence of GHSV during air calcination; the black dots and bars indicate the average and spread in NiO particles found outside the mesopores of SBA-15, respectively. The grey dots indicate the degree of mesopore blockage by NiO present inside the mesopores.

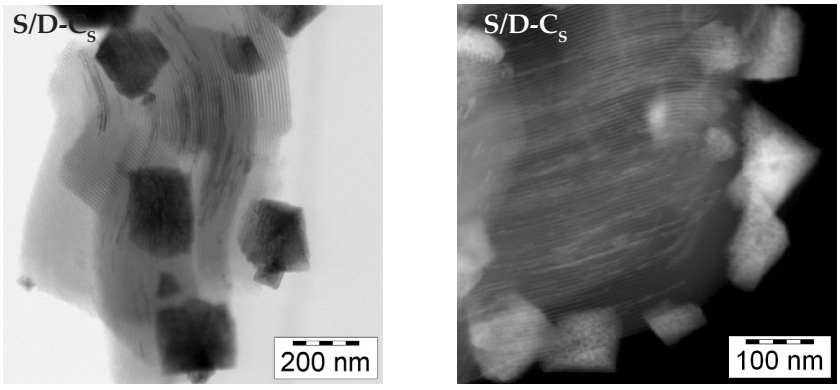


*Figure 10.* Bright-field and HAADF STEM images of sample S/D-$C_S$ that was obtained by calcination in stagnant air of sample S/D.

STEM finding that upon increase of the GHSV precursor mobility to the external surface of the support particles reduced as the degree of pore blockage increased as a consequence of a larger degree of retention of NiO in the mesopores. Thus, we concluded that the decomposition products (i.e. primarily $H_2O$, $NO_2$ and $O_2$) play a crucial role in the sintering and redistribution of NiO. Although mobility could be significantly reduced by applying a GHSV >3,000 $h^{-1}$, the intra-porous migration leading to pore blocking is apparent even at the highest GHSV indicating significant sintering.

*Effects of the individual gaseous decomposition products*

Subsequently, we studied the effects of the individual products, namely $O_2$, $H_2O$ and $NO_2$ by variation of their concentration during the decomposition of sample S/D at a GSHV of about 6,600 $h^{-1}$. The role of $O_2$ was inferred from thermal decomposition of sample S/D in a He flow. The sample was designated S/D-$C_{He}$ for which an average crystal size of 7 nm was found from XRD, which was significantly smaller than had been found with an air flow (10 nm). Comparison of the pattern with that of the air calcined sample S/D-C (Figure 11) revealed that the NiO diffraction lines of sample S/D-$C_{He}$ originated from a bimodal crystal size distribution, also suggesting the presence of crystallites smaller than 7 nm. STEM analysis (Figure 12, top-left) showed that again NiO particles had been deposited inside the mesoporous channels as well as on the external surface of the support particles. However, the size of the latter particles had significantly decreased to 10 to 25 nm. STEM analysis also indicated that less NiO had migrated out of the mesopores. The morphology of the majority of particles inside these pores was similar as observed in air, namely rodlike. $N_2$-physisorption results supported this as significant pore blocking (57%) was observed. However, smaller particles with a spherical geometry were occasionally observed too, which could explain the lower degree of pore blocking. Thus, the results obtained with He indicated that exclusion of $O_2$ from the atmosphere tended to limit the precursor mobility during decomposition of $Ni_3(NO_3)_2(OH)_4$.

Next, the impact of $H_2O$ was investigated by calcination in dry air of a SBA-15 supported anhydrous $Ni(NO_3)_2$ sample, and by thermally treating sample S/D in He containing 15 vol% of $H_2O$ vapour.

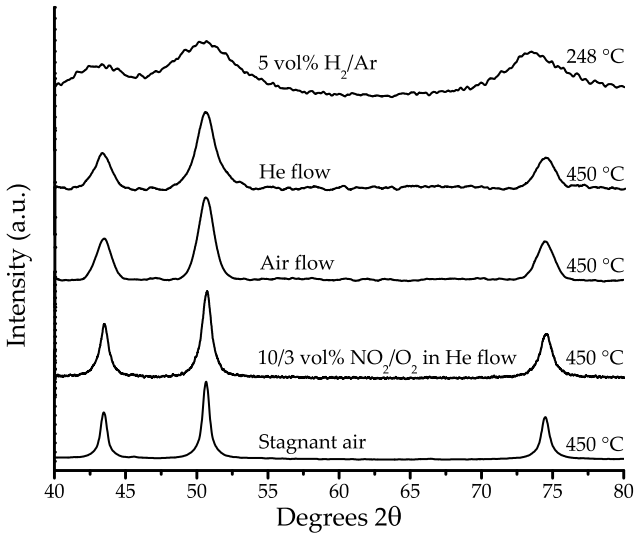


*Figure 11.* XRD patterns of sample S/D after thermal treatment at temperatures and gas atmospheres as indicated.

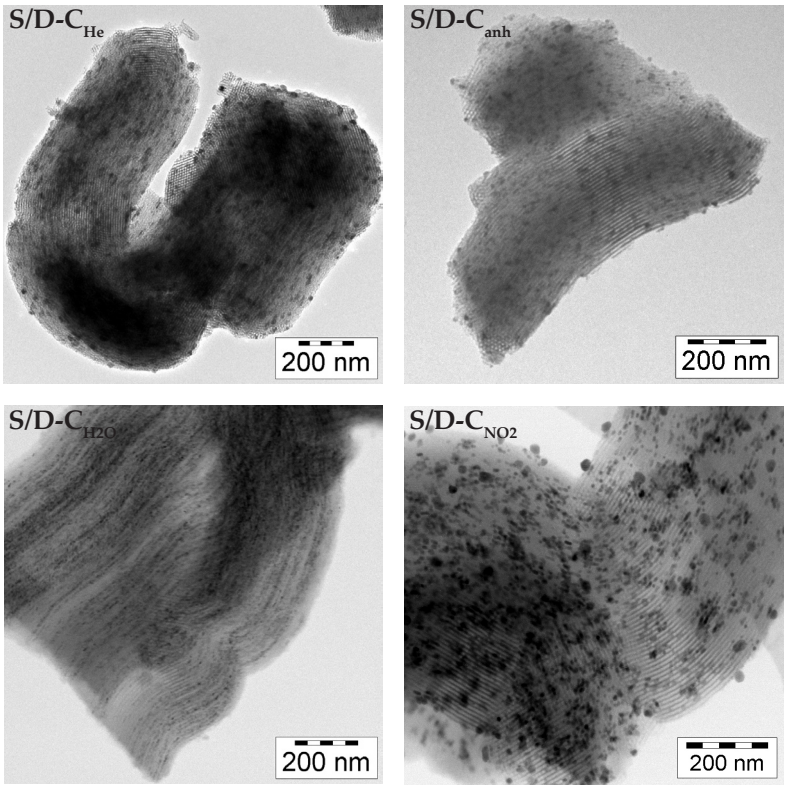


*Figure 12.* STEM images of sample S/D-$C_{He}$ obtained through thermal treatment in pure He flow, sample S/D-$C_{anh}$ heat treated in dry air, sample S/D-$C_{H2O}$ heat treated in a 15 vol% $H_2O$/He flow and sample S/D-$C_{NO2}$ that was obtained after thermal treatment in a 10/3 vol% $NO_2/O_2$ in He flow.

The obtained products were labelled S/D-$C_{anh}$ and S/D-$C_{H2O}$, respectively. It should be noted that the NiO loading of sample S/D-$C_{anh}$ was limited to 9 wt% due to the limited solubility of anhydrous $Ni(NO_3)_2$ in the dry ethanol solvent. Prior to calcination the distribution of the anhydrous $Ni(NO_3)_2$ precursor over the support was checked using HAADF-STEM and found to be similar as observed with sample S/D. Thus, not all pores had been filled with precursor, but those filled appeared to have a homogeneous distribution of precursor within the pore. After calcination of S/D-$C_{anh}$ an average crystal size of 8 nm was found with XRD. NiO particles were observed at the external surface with sizes ranging from 10 to 25 nm (Figure 12, top-right), and also rodlike NiO plugs were found non-uniformly distributed throughout the pores. $N_2$-physisorption showed that these particles blocked 77% of the mesopore volume. Hence, exclusion of $H_2O$ did not prevent sintering. Adding $H_2O$ vapour to the gas atmosphere on the other hand did show a significant impact.

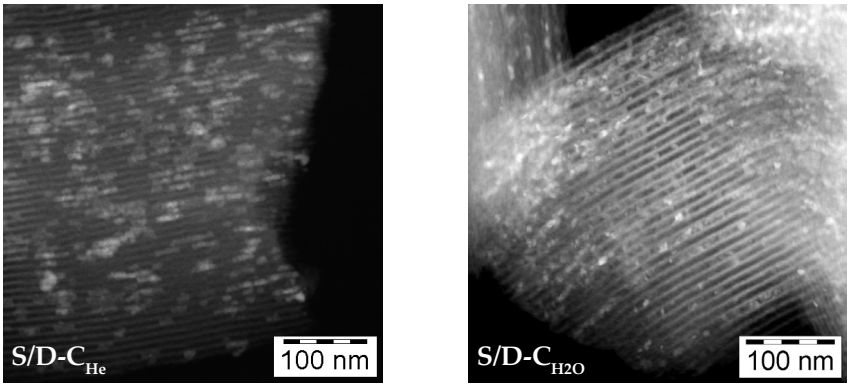


*Figure 13.* HAADF-STEM images obtained after heat treatment at 450 °C of sample S/D in pure He flow (S/D-$C_{He}$) and in 15 vol% $H_2O$/He flow (S/D-$C_{H2O}$).

In the bottom-left frame of Figure 12 a STEM image is included obtained for sample S/D-$C_{H2O}$ that was thermally treated while maintaining a relatively high $H_2O$ vapour partial pressure. The electron micrograph illustrated that addition of 15 vol% $H_2O$ vapour to the He flow led to an inhibiting effect on precursor mobility as the pure He treated sample primarily displayed rod-like particles, whereas the $H_2O$ treated sample showed smaller and more spherical particles inside the mesopores of 6 to 10 nm. This becomes even more apparent when considering the HAADF-STEM images displayed in Figure 13. Using XRD line-broadening for sample S/D-$C_{H2O}$ an average NiO crystal size of 6 nm was found. Partly due to the smaller NiO particles, the degree of pore blocking had somewhat decreased from 57% to 46% compared with the pure He treated sample S/D-CHe. We could derive from these results that thermal decomposition in the presence of steam slightly reduced the degree of precursor sintering and redistribution, but did not prevent it. Finally, the role of $NO_2$/$O_2$ was studied by heating sample S/D in a flow of He that contained 10 vol% $NO_2$ and 3 vol% $O_2$. The obtained product was denoted S/D-$C_{NO2}$ and a typical STEM image is depicted in Figure 12 (bottom-right). The electron micrograph demonstrated that migration out of the mesopores was severe as NiO particles of 20 to 90 nm were observed at the exterior surface of the support particles. Analysis of the XRD diffraction lines (Figure 11) supported the STEM observations as an average NiO crystallite size of 16 nm was found.

In conclusion, the results obtained for the air calcined and He treated samples indicated that $O_2$ plays a role in the sintering process. Moreover, $NO_2$ enhanced sintering too, whereas steam inhibited the precursor transport out of the pores.

*Thermal decomposition in $H_2$ gas atmosphere*

We already showed that omitting the air calcination step significantly reduced the particle size of the final Ni metal phase and improved its distribution over the

support (sample S/D-R, Figure 6). Therefore, we studied the impact of $H_2$ on the decomposition of $Ni_3(NO_3)_2(OH)_4$ in more detail using *in situ* XRD and TGA/MS. With *in situ* XRD the thermal decomposition of the crystalline $Ni_3(NO_3)_2(OH)_4$ phase in a 5 vol% $H_2$/He flow was monitored. Similar experiments using an air flow were carried out too. The normalised peak areas of the $Ni_3(NO_3)_2(OH)_4$ (001) diffraction line obtained during isothermal decomposition at 248 °C in both gas atmospheres have been plotted in Figure 14. Decomposition in air proceeded relatively fast, after an initial slow start, and around 90% of the $Ni_3(NO_3)_2(OH)_4$ had decomposed within five minutes. Decomposition of the $Ni_3(NO_3)_2(OH)_4$ in the $H_2$/He flow was inhibited much longer than in the air flow, but after an incubation time of ~32 minutes decomposition of $Ni_3(NO_3)_2(OH)_4$ started and proceeded during 20 minutes. Decomposition of around 90% of the $Ni_3(NO_3)_2(OH)_4$ in $H_2$/He atmosphere took a factor of 4 longer than in air. Both treatments led to the formation of crystalline NiO, however, the average crystallite size of the air treated sample was significantly larger than that of the $H_2$/He treated sample (3 nm).

In Figure 7, the TGA curve obtained during thermal treatment of sample S/D under a stream of 5 vol% $H_2$/Ar was plotted. The weight loss up to ~200 °C of sample S/D-R was again due to dehydration. At ~220 °C a gradual weight loss was observed that rapidly increased at higher temperatures. This weight loss coincided with decomposition of the $Ni_3(NO_3)_2(OH)_4$ into NiO. The next step in $H_2$/Ar started at ~295 °C, had completed at approximately 400 °C and was accompanied with a weight loss of 4%. This weight loss corresponded with the reduction of NiO into Ni. Thus, TGA demonstrated that reduction of supported $Ni_3(NO_3)_2(OH)_4$ to Ni proceeded via NiO formation. The reduction of a transition metal nitrate also has been described by others to proceed via the formation of a metal oxide prior to reduction to the

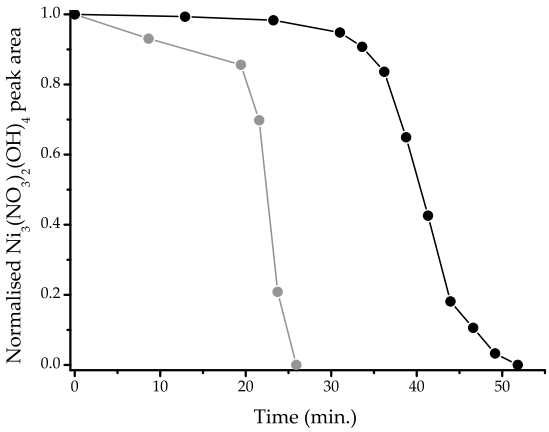


*Figure 14. in situ* XRD results obtained during decomposition of SBA-15 supported $Ni_3(NO_3)_2(OH)_4$ into NiO at a constant temperature of 248 °C either under air flow (grey line) or under 5 vol% $H_2$/He flow (black line).

metal.[51] MS analysis of the predominant gaseous decomposition products showed that $NH_3$ (*m*/*z*= 15), $H_2O$ (*m*/*z*= 18), NO (*m*/*z*= 30) and $N_2O$ (*m*/*z*= 44) were formed. However, $NO_2$ (*m*/*z*= 46) as well as $O_2$ (*m*/*z*= 32) were not detected amongst the gaseous decomposition products. From the effects of the individual decomposition products we had already concluded that $NO_2$ and $O_2$ gaseous decomposition products were detrimental to the final NiO dispersion. Based on the TGA and *in situ* XRD experiments we propose that the beneficial effect of $H_2$ is related to its moderating effect on the decomposition of $Ni_3(NO_3)_2(OH)_4$ and its impact on the type of gaseous decomposition products formed rather than directly reducing the nitrate precursor into the Ni metal phase.

## Conclusions

The use of ordered mesoporous support SBA-15 as model system enabled us to study in detail the individual steps in the preparation of $Ni/SiO_2$ catalysts by the impregnation and drying method using $Ni(NO_3)_2.6H_2O$ as precursor salt.

After the impregnation and drying steps not all the mesopores were filled with precursor, but in the filled pores well-dispersed $Ni_3(NO_3)_2(OH)_4$ was found. $Ni_3(NO_3)_2(OH)_4$ was found exclusively inside the mesopores and its average crystal size of 9 nm was in good agreement with the pore diameter of the mesopores of SBA-15. During the calcination step in air severe sintering and redistribution took place, resulting in deposition of large NiO particles (10-35 nm) outside the mesopores as well as rodlike NiO plugs inside the mesopores. The degree of NiO migration to the exterior surface increased with higher concentrations of evolved gaseous decomposition products. MS results showed that these gaseous decomposition products consisted of $H_2O$, $N_2O$ $NO_2$ and $O_2$. We found that in particular the latter two promoted sintering and redistribution during the thermal treatment, whereas $H_2O$ vapour was found to have an inhibiting effect on the sintering process out of the pores. Furthermore, we showed that sintering during $Ni_3(NO_3)_2(OH)_4$ decomposition could be avoided if carried out in the presence of $H_2$. With $H_2$ formation of the $O_2$ and $NO_2$ decomposition products was prevented. $H_2$ also showed to moderate the rate of $Ni_3(NO_3)_2(OH)_4$ decomposition, resulting in slower decomposition than in air. The 24 wt% NiO/SBA-15 samples treated in a 5 vol% $H_2$/He flow displayed a high NiO dispersion (crystallites of 3 nm on average) contrary to samples treated either in air or in pure He. Hence, when highly dispersed and highly loaded $Ni/SiO_2$ catalysts are desired, use of an $H_2$-containing atmosphere is beneficial.

**Acknowledgements**

Jos van Dillen is kindly thanked for his guidance and support. Hans Meeldijk, Fred Broersma and Marjan Versluijs-Helder are acknowledged for their assistance with TEM, TGA/MS and *in situ* XRD analysis, respectively.

**References**

1. Balakos, M. W.; Hernandez, E.E. *Catal. Today* **1997**, *35*, 415-425.
2. Fouilloux, P. *Appl. Catal.* **1983**, *8*, 1-42.
3. Allen, R.R. *J. Am. Oil Chem. Soc.* **1986**, *63*, 1328-1332.
4. Schreier, M.; Regalbuto, J.R. *J. Catal.* **2004**, *225*, 190-202.
5. Carrier, X.; Lambert, J.F.; Che, M. *J. Am. Chem. Soc.* **1997**, *119*, 10137-10146.
6. Hermans, L.A.M.; Geus, J.W. *Stud. Surf. Sci. Catal.* **1979**, *3*, 113-130.
7. Van der Lee, M.K.; Van Dillen, A.J.; Bitter, J.H.; De Jong, K.P. *J. Am. Chem. Soc.* **2005**, *127*, 13573-13582.
8. Che, M.; Cheng, Z.X.; Louis, C. *J. Am. Chem. Soc.* **1995**, *117*, 2008-2018.
9. Bourikas, K.; Kordulis, C.; Lycourghiotis, A. *Catal. Rev.* **2006**, *48*, 363-444.
10. De Jong, K.P. *Curr. Op. Solid Mat. Sci.* **1999**, *4*, 55-62.
11. Clause, O.; Kermarec, M.; Bonnevoit, L.; Villain, F.; Che, M. *J. Am. Chem. Soc.* **1992**, *114*, 4709-4717.
12. Carriat, J.Y.; Che, M.; Kermarec, M.; Verdaguer, M.; Michalowicz, A. *J. Am. Chem. Soc.* **1998**, *120*, 2059-2070.
13. Lekhal, A.; Glasser, B.J.; Khinast, J.G. *Chem. Eng. Sci.* **2004**, *59*, 1063-1077.
14. Négrier, F.; Marceau, E.; Che, M.; Giraudon, J-M.; Gengembre, G.; Löfberg, A. *J. Phys. Chem. B* **2005**, *109*, 2836-2845.
15. Li, G.; Hu, L.; Hill, J.M. *Appl. Catal. A* **2006**, *301*, 16-24.
16. Burattin, P.; Che, M.; Louis, C. *J. Phys. Chem. B* **1997**, *101*, 7060-7074.
17. Wang, Y.; Noguchi, M.; Takahashi, Y.; Ohtsuka, Y. *Catal. Today* **2001**, *68*, 3-9.
18. Ohtsuka, Y.; Takahashi, Y.; Noguchi, M.; Arai, T.; Takasaki, S.; Tsubouchi, N.; Wang, Y. *Catal. Today* **2004**, *89*, 419-429.
19. Van den Brink, P.J.; Scholten, A.; Van Wageningen, A.; Lamers, M.D.A.; Van Dillen, A.J.; Geus, J.W. *Stud. Surf. Sci. Catal.* **1991**, *63*, 527-537.
20. Chen, H-C.; Anderson, R.B. *J. Catal.* **1976**, *43*, 200-206.
21. Crosfield and Sons, *Patent* No. GB1030282 **1910**.
22. Lensveld, D.J.; Mesu, J.G.; Van Dillen, A.J.; De Jong, K.P. *Micropor. Mesopor. Mater.* **2001**, *44-45*, 401-407.
23. Infantes-Molina, A.; Mérida-Robles, J.; Braos-García, P. ; Rodríguez-Castellón, E.; Finocchio, E.; Busca, G.; Maireles-Torres, P.; Jiménez-López, A. *J. Catal.* **2004**, *225*, 479-488.
24. Kotter, M.; Riekert, L. *Stud. Surf. Sci. Catal.* **1979**, *3*, 51-63.

25. Van Dillen, A.J.; Terörde, R.J.A.M.; Lensveld, D.J.; Geus, J.W.; de Jong, K.P. *J. Catal.* **2003**, *216*, 257-264.
26. Chen, I.; Lin, S-Y.; Shiue, D-W. *Ind. Eng. Chem. Res.* **1988**, *27*, 926-929.
27. Poels, E.K.; Dekker, J.G.; Van Leeuwen, W.A. *Stud. Surf. Sci. Catal.* **1991**, *63*, 205-214.
28. Vos, B.; Poels, E.K.; Bliek, A. *J. Catal.* **2001**, *198*, 77-88.
29. Reinalda, D.; Kars, J. *U.S. Patent* No. 5,021,387 **1991**.
30. Van de Loosdrecht, J.; Barradas, S.; Caricato, E.A.; Ngwenya, N.G.; Nkwanyana, P.S.; Rawat, M.A.S.; Sigwebela, B.H.; Van Berge, P.J.; Visagie, J.L. *Top. Catal.* **2003**, *26*, 121-127.
31. Louis, C.; Cheng, Z.X.; Che, M. *J. Phys. Chem.* **1993**, *97*, 5703-5712.
32. Kresge, C.T.; Leonowicz, M.E.; Roth, W.J.; Vartuli, J.C.; Beck, J.S. *Nature* **1992**, *359*, 710-712.
33. Zhao, D.; Feng, J.; Huo, Q.; Melosh, N.; Fredrickson, G.H.; Chmelka, B.F.; Stucky, G.D. *Science* **1998**, *279*, 548-552.
34. Ravikovitch, P.I.; Neimark, A.V. *Langmuir* **2002**, *18*, 9830-9837.
35. Van der Voort, P.; Ravikovitch, P.I.; De Jong, K.P.; Benjeloun, M.; Van Bavel, E.; Janssen, A.H.; Neimark, A.V.; Weckhuysen, B.M.; Vansant, E.F. *J. Phys. Chem. B* **2002**, *106*, 5873-5877.
36. Janssen, A.H.; Yang, C.-M.; Wang, Y.; Schuth, F.; Koster, A.J.; De Jong, K.P. *J. Phys. Chem. B.* **2003**, *107*, 10552-10556.
37. Neimark, A.V.; Kheifez, L.I.; Fenelonov, V.B. *Ind. Eng. Chem. Prod. Res. Dev.* **1981**, *20*, 439-450.
38. Van Leeuwen, P.W.N.M.; Groeneveld, W.L. *Inorg. Nucl. Chem. Letters* **1967**, *3*, 145-146.
39. Jaroniec, M.; Kruk, M.; Olivier, J.P.; Koch, S. *Stud. Surf. Sci. Catal.* **2000**, *128*, 71-80.
40. Barrett, E.P.; Joyner, L.S.; Halenda, P.P. *J. Am. Chem. Soc.* **1951**, *73*, 373-380.
41. Harkins, W.D.; Jura, G. *J. Am. Chem. Soc.* **1944**, *66*, 1366-1373.
42. Kruk, M.; Jaroniec, M.; Sayari, A. *Langmuir* **1997**, *13*, 6267-6273.
43. Lippens, B.C.; De Boer, J.H. *J. Catal.* **1965**, *4*, 319-323.
44. Thomas, J.M.; Midgley, P.A.; Yates, T.J.V.; Barnard, J.S.; Raja, R.; Arslan, I.; Weyland, M. *Angew. Chem. Int. Ed.* **2004**, *43*, 6745-6747.
45. Gallezot, P.; Prettre, M. *Bull. Soc. Chim. Fr.* **1969**, *2*, 407-411.
46. Estellé, J.; Salagre, P.; Cesteros, Y.; Serra, M.; Medina, F.; Sueiras, J.E. *Solid State Ionics* **2003**, *156*, 233-243.
47. Ek, S.; Root, A.; Peussa, M.; Niinistö, L. *Thermochim. Acta* **2001**, *379*, 201-212.
48. Staszczuk, P.; Jaroniec, M.; Gilpin, R.K. *Thermochim. Acta* **1996**, *287*, 225-233.
49. Wang, C-B.; Gau, G-Y.; Gau, S-J.; Tang, C-W.; Bi, J-L. *Catal. Lett.* **2005**, *101*, 241-247.
50. Małecki, A.; Małecki, B. *Thermochim. Acta* **2006**, *446*, 113-116.
51. Yuvaraj, S.; Fan-Yuan, L.; Tsong-Huei, C.; Chuin-Tih, Y. *J. Phys. Chem. B* **2003**, *107*, 1044-1047.

# 4

# NO calcination: a new method for the preparation of highly dispersed supported NiO and $Co_3O_4$ particles from nitrate precursor

A novel method is described for the preparation of well-dispersed NiO and $Co_3O_4$ nanoparticles (3 to 5 nm) on ordered mesoporous SBA-15, silica gel and carbon nanofibers at loadings between 16 to 37 wt% depending on the support used. The method is based on the impregnation and drying technique using aqueous metal nitrate precursor solutions, and comprises of thermal treatment of the dried impregnate in a flow of NO/He instead of in an air flow (i.e. calcination). The required concentration of NO showed to depend on the applied gas-hourly-space-velocity (GHSV). At an NiO loading of 28 wt% and a GHSV of 24,500 $h^{-1}$ or 6,800 $h^{-1}$, the minimum NO concentration needed was 0.1 or 1 vol%, respectively. Catalytic testing of silica gel supported Ni catalysts in the hydrogenation of soybean oil demonstrated that the NO/He method led to a more active catalyst as the hydrogenation time was reduced by ~30% compared to the traditionally air calcined catalyst.

## Introduction

Supported metal (oxide) catalysts play a crucial role in the production of fuels and chemicals, and environmental protection.[1-3] Since catalytic processes take place at the metal (oxide) surface, high surface-to-volume ratios are important. Preparation techniques, therefore, aim at obtaining a highly dispersed active phase. Preferably, the high dispersion of the active component is combined with high loadings. Supported metal (oxide) particles can be obtained by deposition from the vapour or liquid phase. Although Chemical Vapour Deposition (CVD) and Atomic Layer Deposition (ALD) techniques enable uniform deposition of the active phase or its precursor onto a support, the deposition from gaseous precursors is complicated, relatively expensive and generally limited to low loadings.[4,5] As a result catalyst preparation techniques are typically based on liquid phase processes. Methods comprise of ion-adsorption[6,7], deposition-precipitation[8-11] and impregnation and drying[12-16]. In particular the latter two are used as they enable high metal (oxide) loadings. The Homogeneous Deposition Precipitation (HDP) method studied extensively by Geus and co-workers[8], is based on controlled nucleation of a precursor onto support particles and allows loadings up to 60 wt% while ensuring relatively small particles of 3 to 10 nm depending on the precipitation conditions and type of support used. Although the effectiveness of this method for the preparation of carbon supported Ni particles was recently demonstrated[9], when oxidic supports are used elevated reduction temperatures are often required due to the formation of co-precipitates between support and metal precursor (e.g. phyllosilicates[17] and aluminates[18]).

As an alternative technique impregnation of a support with a precursor-containing solution followed by drying is often used. Subsequently the dried impregnate is treated through calcination in air to convert the precursor into the desired metal oxide, or metal when followed by high-temperature reduction with $H_2$. The composition of the impregnation solution has a large impact on the final metal (oxide). Small particles of 1 to 3 nm typically can be deposited when organic precursor complexes are used such as those from citric acid, nitrilotriacetic acid (NTA) and ethylenediamminetetraacetic acid (EDTA).[19] Upon drying, these precursors tend to form a uniform viscous film over the support finally resulting in a highly dispersed metal phase. Unfortunately, only moderate loadings (≤10 wt%) can be obtained via single-step impregnations due to the limited solubility of the metal complexes. Therefore, solutions of inorganic salts are often used when higher loadings are required. Primarily metal nitrates are used because of complete removal of nitrate, contrary to chlorides, resulting in a pure metal oxide phase. Regrettably, catalysts prepared from nitrate precursor salts often display poor metal dispersions.[20-29] In chapter 3 it was demonstrated for $Ni/SiO_2$ *ex* nitrate catalysts that this originates from sintering and redistribution during the air calcination step. We also identified that in particular the gaseous $NO_2$ and $O_2$ decomposition products had a detrimental role on the final dispersion. We showed that carrying out the thermal treatment in $H_2$ prevented formation of these products, which resulted in small NiO particles.

Both Ni and Co are amongst the most abundantly used metals for catalysis because of their activity in important (de)-hydrogenation processes[30-32] and the Fischer-Tropsch synthesis of liquid fuels.[33-35] In this chapter, we present a novel method based on impregnation with aqueous metal nitrate solutions that allows preparation of uniform NiO and $Co_3O_4$ nanoparticles. The method comprises of thermal decomposition of the dried supported metal nitrate in an NO/He gas atmosphere instead of in air. Using the results obtained for the ordered mesoporous SBA-15 supported NiO samples we demonstrate the advantage of using NO/He instead of air or He gas atmospheres. The relevance of this method for other catalyst systems is explored too. Moreover, the significance for catalysis is illustrated with catalytic results of the $Ni/SiO_2$ catalysts in the hydrogenation of Soybean oil.[36]

## Experimental

*Sample preparation*

SBA-15 (pore volume= 0.78 $ml.g^{-1}$ and average pore diameter= 9 nm) was prepared following the procedure of Zhao *et al.*[37]. 8 g $PEO_{20}PPO_{70}PEO_{20}$ (PEO= poly(ethylene oxide) and PPO= poly(propylene oxide)) tri-block copolymer (Aldrich) was dissolved in 250 ml demineralised water of 40 °C. After the solution had become clear, 48 g of concentrated HCl (Merck) was added, followed by the addition of 21.5 ml of tetraethyl orthosilicate (Acros). Next, the mixture was stirred for 20 hours at 40 °C after which it was transferred to an oven for further reaction at 80 °C for 48 hours. The solid product was collected from the suspension by filtration, washed, dried in air for 12 hours at 80 °C and calcined for 6 hours at 550 °C.

Davicat 1404SI silica gel (BET surface area= 500 $m^2.g^{-1}$, pore volume= 0.90 $ml.g^{-1}$ and average pore diameter= 7 nm) was used as received from Grace-Davison. Carbon nanofibers were prepared and surface-oxidised according to a literature procedure of Toebes *et al.*[38].

Prior to impregnation, the supports were dried for 2 hours in vacuo at 80 °C to remove physisorbed $H_2O$. SBA-15 quantities of 0.25 g were impregnated in static vacuum with 1.0 $ml.g^{-1}$ aqueous 4.2 M $[Ni(OH_2)_6](NO_3)_2$, or aqueous 3 M $[Co(OH_2)_6](NO_3)_2$ solutions (demineralised $H_2O$) to provide loadings of 24 wt% NiO, and 19 wt% $Co_3O_4$, respectively. Quantities of 1 g of silica gel were impregnated using 1.25 $ml.g^{-1}$ of the same Ni and Co nitrate solutions to yield 28 wt% NiO and 23 wt% $Co_3O_4$ loadings. CNF (2g) was impregnated with 0.65 $ml.g^{-1}$ of aqueous 3.6 M $[Co(OH_2)_6](NO_3)_2$ solution to yield a loading of 16 wt% $Co_3O_4$. The impregnates were dried in static air by increasing the temperature from room temperature at a rate of 1 $°C.min^{-1}$ to 120 °C for the Ni samples and 70 °C for the Co samples. The samples were kept at the final temperatures for 12 hours.

Small quantities of the dried SBA-15 (40 mg) and silica gel supported (100 mg) samples were calcined in an air flow of 90 $ml.min^{-1}$ using a plug-flow reactor (length 17 cm and diameter 1 cm). The samples were heated to 450 °C with a ramp of

1 °C.min$^{-1}$ and kept at 450 °C for 4 hours. A similar heating profile was used for the thermal treatments in NO/He or in He. The total flow rates and NO concentrations were varied between 0 to 90 ml.min$^{-1}$ and 0.01 to 1 vol% NO/He, respectively.

Reduction treatments were performed by heating the dried samples to 600 °C at a rate of 5 °C.min$^{-1}$, while 5 vol% $H_2$/Ar flow was passed through the sample bed. The reduced samples were passivated via controlled exposure to air.

Two nickel catalysts were tested in the hydrogenation of soybean oil with an iodine value (IV) of 133. A portion of 70 mg of NiO/$SiO_2$ sample was weighed into a glass vessel and reduced for 1 hour at 400 to 450 °C under atmospheric $H_2$ pressure. The reduced catalyst was transferred into 200 g of soybean oil and loaded to a closed and stirred hydrogenation reactor (Medimex). The mixture was heated to 140°C and $H_2$ sparged through the slurry at a pressure of 3 bar abs. The temperature was raised by 2 °C.min$^{-1}$ to 200 °C and kept at that temperature. The amount of $H_2$ absorbed into the oil was monitored with a Büchi gas dosage unit and the test was terminated once the IV had dropped to 79. The hydrogenation time to reach an IV of 79 was used as a measure of the activity of the catalyst. The melting point and percentage of trans-isomers were determined using standard methods.[53,54]

All samples were labelled using sample codes. An example of a sample code is S24Ni/D-$C_{He}$. The first part S24Ni denotes the support: S = SBA-15 and G = silica gel support and metal oxide loading of 24wt% NiO, whereas the second part indicates the thermal treatments that was applied: D = drying in static air, $C_{He}$ = heat treatment in He flow at 450 °C.

*Characterisation*.

$N_2$-physisorption measurements were performed at -196 °C, using a Micromeritics Tristar 3000 apparatus. Prior to analysis the samples were dried in He flow for 14 hours at 120 °C. The pore size distribution was derived from the adsorption branch of the isotherm using non-local density functional theory (NL-DFT). A model developed by Jaroniec *et al*.[39] for ordered mesoporous silica supports with a cylindrical pore geometry was used. This model seemed a reliable representation of the data as it depended only slightly on the regularization constraint. The pore diameter of the mesoporous channels of SBA-15 was defined by the value at which the maximum in differential pore volume was observed. The micro- and meso-porosity were defined as the volume present in pores smaller than 2 nm, and between 2 and 50 nm, respectively. There is no standard method yet for the determination of blocked mesopore volume ($V_{meso,bl}$). We used BJH theory[40] with the Harkins and Jura[41] thickness equation and the Kruk-Jaroniec-Sayari[42] correction for ordered mesoporous siliceous materials to calculate from the desorption branch the cumulative pore volume as a function of the pore size. From this we determined the total amount of blocked volume ($V_{meso,bl}$) considering that the pores with a diameter of 2 to 5 nm are due to volume in (partially) blocked pores. Finally, mesopore and external surface areas were determined with the t-method using thickness ranges of 0.35-0.55 and 1.00-1.41 nm, respectively.[43]

Powder X-ray diffraction (XRD) patterns were obtained at room temperature from 5 to 90° 2θ with a Bruker-AXS D8 Advance X-ray Diffractometer setup using Co-$K_{\alpha 12}$ radiation. Low angle diffraction patterns from 0.5 to 5° 2θ were recorded using a zero-background sample holder from Bruker-AXS. The average $Ni_3(NO_3)_2(OH)_4$, NiO and $Co_3O_4$ sizes were calculated according to the Scherrer equation ($k$=1) using the most intense diffraction peaks at 2θ = 14.9°, 50.8° and 43.1°, respectively.

Scanning Transmission Electron Microscopy (STEM) images were obtained using a Tecnai 20 microscope operating at 200 kV and equipped with a High-Angle Annular Dark-Field (HAADF) detector. A typical camera length of 120 mm was used for HAADF. With this detector high-angle scattered electrons are collected instead of the low angle scattered electrons used for normal dark-field imaging. Since the intensity of the high-angle scattered electrons is approximately proportional to $Z^2$, heavy elements appear as bright spots in the images.

## Results and discussion

*Preparation of SBA-15 supported NiO*

SBA-15 was impregnated with aqueous $[Ni(OH_2)_6](NO_3)_2$ solution, and dried at 120 °C to yield sample S24Ni/D that displayed a 24 wt% NiO/SBA-15 loading. The XRD pattern of the dried impregnate (not shown) contained diffraction lines typical for that of layered nickel nitrate hydroxide crystal phase $Ni_3(NO_3)_2(OH)_4$.[44,45] Line broadening analysis of the (001) peak showed that crystallites of 9 nm on average had formed, which was in good agreement with the mesopore diameter (9 nm) and indicated confinement by the pore walls. In Figure 1 (center image) an HAADF-STEM image of the dried impregnate is shown together with that of the NiO/SBA-15 samples obtained thereof after subsequent thermal treatment at 450 °C under different atmospheres, as indicated. STEM results of the dried impregnate S/D revealed exclusive deposition of precursor inside the mesopores as no large particles or agglomerates of $Ni_3(NO_3)_2(OH)_4$ were found outside the mesopores. As discussed in chapter 2 and others[46,47], incomplete filling of the pores was observed. However, the filled pores appeared to contain well-dispersed nickel precursor phase. Details of the XRD and STEM characterisation results of all the samples are given in Table 1. Severe sintering and redistribution during calcination in air flow resulted in large NiO particles of about 10 to 35 nm at the exterior surface of the SBA-15 particles and rodlike particles inside the mesopores (Figure 1, top-left image). The latter particles appeared confined by the pore diameter. The bottom-left image in Figure 1 obtained after calcination in stagnant air demonstrated that high concentrations of gaseous decomposition products led to NiO particles of 20 to 100 nm at the exterior surface, and rodlike NiO particles inside the mesopores. The XRD patterns (Figure 2) confirmed the STEM findings as NiO crystallites with an average size of 10 and ≥25 nm were found with the air flow and stagnant air treated samples, respectively. Hence, maintaining a high gas-hourly-space-velocity (GHSV) during

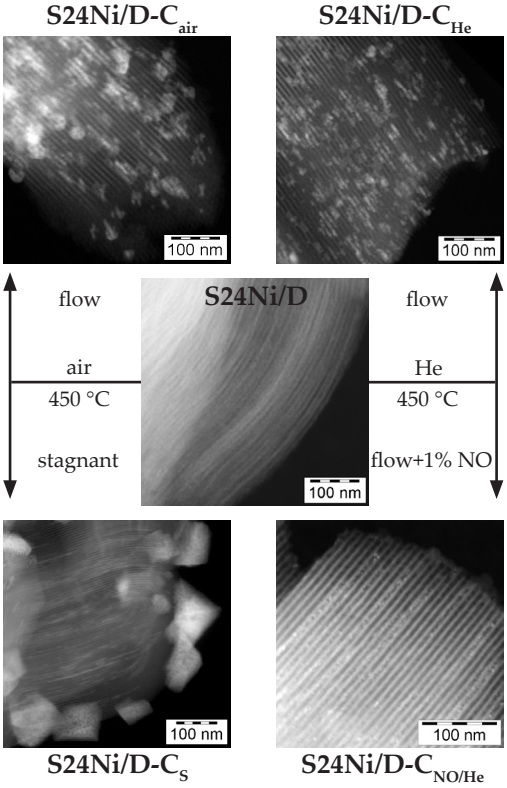


*Figure 1.* HAADF-STEM images of $Ni_3(NO_3)_2(OH)_4$ sample S24Ni/D obtained after drying at 120 °C and of NiO/SBA-15 samples obtained after different thermal treatments at 450 °C, as indicated.

air calcination showed to favour formation of smaller NiO particles. These results are in line with observations by Poels *et al.* and van de Loosdrecht co-workers.[21,22,24] The SBA-15 supported samples were also characterised with $N_2$-physisorption. The isotherms were corrected for the contribution of precursor to the total weight of the sample and hence expressed per gram of $SiO_2$. The results have been summarised in Table 2, but also isotherms of a few selected samples are depicted in Figure 3. The isotherm of the pristine SBA-15 (Figure 3a) contained all features typical for this material: a high onset at low relative pressures because of the intra-wall micro porosity, and hysteresis at higher values originating from the mesoporous channels. The small relative pressure region of 0.69 to 0.71 in which capillary condensation took place during adsorption is a consequence of the uniform mesopore diameter of 9 nm. $N_2$-physisorption results of dried impregnate S24Ni/D (Table 2) showed that the porosity had decreased to 0.47 $cm^3.g_{SiO2}^{-1}$ upon deposition of $Ni_3(NO_3)_2(OH)_4$ in the mesopores. Also shown in Figure 3a is the isotherm of the air calcined sample

S24Ni/D-$C_{air}$. The adsorption branch contained similar features as observed for pristine SBA-15, whereas during desorption a delayed closure of the hysteresis loop was found in the relative pressure region of 0.45 to 0.60. This forced closure of the desorption branch at ~0.48 is typical for emptying of ink-bottle pores with necks smaller than 3 to 4 nm and is referred to as cavitation.[48-51] In case of SBA-15, these pores could have been created by voids between rodlike NiO particles inside the mesopores, with the micropores as pore necks. In sample S24Ni/D-$C_{air}$, this partially blocked mesopore volume ($V_{meso,bl}$) was found to be 75% of the total accessible mesoporosity.

The top-right STEM image in Figure 1 of sample S24Ni/D-$C_{He}$ was recorded after thermal treatment of the dried impregnate in pure He flow. The electron micrograph showed that use of He flow instead of air flow led to a reduced degree of migration out of the mesopores as the number and size (10 - 25 nm) of NiO particles decreased. Although smaller NiO particles were found, the majority of particles inside the mesopores had adopted a rodlike symmetry indicating that intrapore migration took place. XRD analysis showed that NiO crystallites with an average size of 7 nm had formed, but the peak shape of the diffraction lines (Figure 2) also revealed the bimodal NiO crystal size distribution as the onset of the peaks displayed additional broadening. Hence, decomposition under an $O_2$-free atmosphere significantly reduced sintering and redistribution but it did not prevent it.

Finally, the bottom-right frame of Figure 1 shows the electron micrograph of SBA-15 supported NiO prepared by heating under a stream of 1 vol% NO/He. Contrary to the NiO/SBA-15 sample prepared through heat treatment in pure He flow, exclusively small NiO particles of about 3 to 5 nm were found. Neither NiO

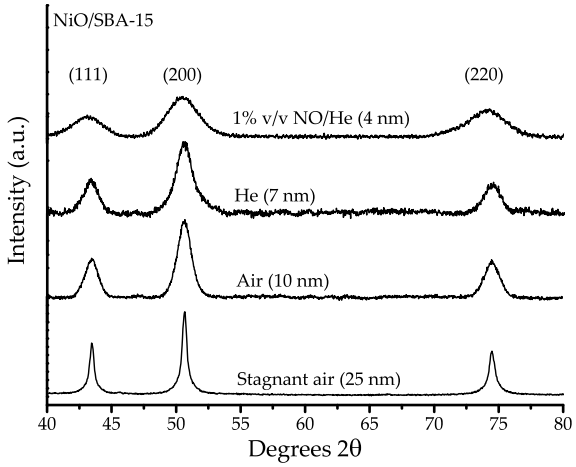


*Figure 2.* XRD patterns of 24 wt% NiO/SBA-15 samples obtained after thermal treatment at 450 °C under different atmospheres, as indicated.

*Table 1.* Overview of applied thermal treatments and, XRD and STEM results of samples.

| Samples | Thermal treatments | Nickel phase | Loading (wt%) | Size (nm) | |
|---|---|---|---|---|---|
| | | | | $d_{XRD}$ | $d_{TEM}$ |
| **Silica gel** | | | | | |
| G28Ni/D | drying | $Ni_3(NO_3)_2(OH)_4$ | 39 | 12 | - |
| G28Ni/D-$C_{air}$ | drying/calcination | NiO | 28 | 15 | 7-70 |
| G28Ni/D-$C_{NO/He}$ | drying/heating in 1 vol% NO/He | NiO | 28 | 4 | 3-5 |
| G23Co/D | drying | amorphous | 52[a] | - | - |
| G23Co/D-$C_{air}$ | drying/calcination | $Co_3O_4$ | 23 | 11 | 8-60 |
| G23Co/D-$C_{NO/He}$ | drying/heating in 1 vol% NO/He | $Co_3O_4$ | 23 | 5 | 3-5 |
| **SBA-15** | | | | | |
| S24Ni/D | drying | $Ni_3(NO_3)_2(OH)_4$ | 34 | 9 | - |
| S24Ni/D-$C_{air}$ | drying/calcination | NiO | 24 | 10 | 10-35 |
| S24Ni/D-$C_{He}$ | drying/heating in He | NiO | 24 | 7 | 10-25 |
| S24Ni/D-$C_s$ | drying/calcination (stagnant air) | NiO | 24 | ≥25 | 50-200 |
| S24Ni/D-$C_{NO/He}$ | drying/heating in 1 vol% NO/He | NiO | 24 | 4 | 3-5 |
| S37Ni/D | drying | NiO | 49 | 9 | - |
| S37Ni/D-$C_{air}$ | drying/calcination | NiO | 37 | 11 | 15-60 |
| S37Ni/D-$C_{NO/He}$ | drying/heating in 1 vol% NO/He | NiO | 37 | 4 | 3-5[b] |
| S19Co/D | drying | amorphous | 47[a] | - | - |
| S19Co/D-$C_{air}$ | drying/calcination | $Co_3O_4$ | 19 | 10 | 10-100[c] |
| S19Co/D-$C_{NO/He}$ | drying/heating in 1 vol% NO/He | $Co_3O_4$ | 19 | 5 | 3-5 |
| **CNF** | | | | | |
| CNF16Co/D | drying | amorphous | 31 | - | - |
| CNF16Co/D-$C_{air}$ | drying/calcination | $Co_3O_4$ | 16 | 9 | 5-15 |
| CNF16Co/D-$C_{NO/He}$ | drying/heating in 1 vol% NO/He | $Co_3O_4$ | 16 | 5 | 3-6 |

[a]assuming $Co(NO_3)_2.6H_2O$ phase; [b]analysis hampered by high NiO particle density; [c]primarily rodlike $Co_3O_4$ particles were found inside the pores.

particles were found at the exterior surface of the SBA-15 particles, nor rodlike particles inside the pores as observed with the other gas atmospheres, and the NiO particles appeared homogeneously distributed throughout the mesopores. Additional HAADF-STEM tilt series supported these findings, and quantitative electron tomography results obtained for this sample and published elsewhere[52] were in line too. The XRD pattern of the NO/He treated sample is depicted in Figure 2. Line-broadening analysis showed that crystallites of 4 nm on average had formed. Thus, use of a pure He flow reduced migration out of the pores, but addition of 1 vol% of NO to the He flow completely prevented sintering and redistribution, resulting in the formation of exclusively small NiO particles.

These findings were supported by $N_2$-physisorption results. Shown in Figure 3b and 3c are the isotherms obtained for the samples prepared by heat treatment under pure He flow or under 1 vol% NO/He flow. The isotherm of the He treated sample contained similar features as observed after calcination in air; capillary condensation typical for SBA-15 and cavitation due to the rodlike NiO plugs inside

*Table 2.* Overview of $N_2$-physisorption results of SBA-15 supported samples.

| **Sample** | **Surface area ($m^2.g_{SiO2}^{-1}$)** | | **Porosity ($cm^3.g_{SiO2}^{-1}$)** | | | | | |
|---|---|---|---|---|---|---|---|---|
| | $S_t$ [a] | $S_{t,ext}$ [b] | $V_{tot,calc}$ [c] | $V_{tot,exp}$ [d] | $V_{micro}$ [e] | $V_{meso}$ [f] | $V_{meso,bl}$ [g] | (%) |
| SBA-15 | 516 | 38 | 0.78 | 0.78 | 0.05 | 0.68 | 0.00 | 0 |
| S24Ni/D | 293 | 33 | 0.63 | 0.47 | 0.01 | 0.42 | 0.08 | 19 |
| S24Ni/D-$C_S$ | 388 | 33 | 0.73 | 0.65 | 0.04 | 0.56 | 0.15 | 27 |
| S24Ni/D-$C_{air}$ | 409 | 31 | 0.73 | 0.66 | 0.06 | 0.56 | 0.42 | 75 |
| S24Ni/D-$C_{He}$ | 442 | 34 | 0.73 | 0.59 | 0.03 | 0.51 | 0.29 | 57 |
| S24Ni/D-$C_{NO/He}$ | 493 | 26 | 0.73 | 0.59 | 0.05 | 0.49 | 0.00 | 0 |
| S37Ni/D | 342 | 32 | 0.50 | 0.42 | 0.06 | 0.33 | 0.15 | 45 |
| S37Ni/D-$C_{air}$ | 455 | 38 | 0.69 | 0.65 | 0.04 | 0.56 | 0.47 | 84 |
| S37Ni/D-$C_{NO/He}$ | 515 | 33 | 0.69 | 0.57 | 0.04 | 0.49 | 0.13 | 27 |
| S19Co/D | 231 | 27 | 0.53[h] | 0.42 | 0.01 | 0.39 | 0.00 | 0 |
| S19Co/D-$C_{air}$ | 400 | 33 | 0.74 | 0.56 | 0.02 | 0.50 | 0.41 | 82 |
| S19Co/D-$C_{NO/He}$ | 330 | 27 | 0.74 | 0.47 | 0.04 | 0.40 | 0.00 | 0 |

[a]mesopore surface area determined using t-method; [b]external surface area calculated using t-method; [c]expected total pore volume based on contribution of precursor to volume decrease; [d]total pore volume based on amount $N_2$ adsorbed at $p/p_o$=0.995; [e]micropore volume calculated using NL-DFT; [f]mesopore volume calculated using NL-DFT; [g]partially blocked mesopore volume calculated from desorption branch (see experimental section for details); [h]assuming a $Co(NO_3)_2.6H_2O$ phase.

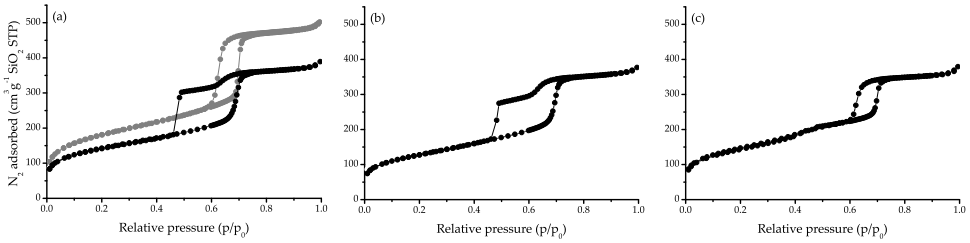


*Figure 3.* $N_2$-physisorption isotherms of pristine SBA-15 (a, grey) and of NiO/SBA-15 samples obtained after heat treatment of dried impregnate S/D in air flow (a), in pure He flow (b) or in 1% NO/He flow (c).

the mesopores. The latter feature was not observed in the desorption branch of sample S24Ni/D-$C_{NO/He}$, and instead a hysteresis loop typical for SBA-15 was found. As the NiO particle size had been limited by the NO/He flow, the voids were now large enough to allow normal emptying of the mesopores during desorption. As a result the degree of partial pore blocking of 57% and 73% as observed with He flow and air flow, respectively, had now dropped to zero. Moreover, the mesopore diameter of 9 nm and required minimum pore neck size of 3 to 4 nm to prevent cavitation[48-51] indicated that the maximum NiO size was 5 to 6 nm. The mesopore volumes found for the air, He and NO/He samples qualitatively supported the STEM findings, as a lower porosity was found for the NO/He treated sample than for the air and He ones due to the more extensive migration of the NiO guest phase out of the mesopores, for the latter cases.

After establishing the beneficial role of 1 vol% NO/He flow on the final dispersion of 24 wt% NiO/SBA-15 catalysts, we investigated the possibility to obtain higher loadings of small NiO particles with this treatment. As was discussed in chapter 2, impregnating the SBA-15 support with 1.0 ml.$g^{-1}$ precursor solution to yield 24 wt% NiO had resulted in non-uniform filling of the pores. It was also shown in the same chapter that a higher degree of filling of all the pores could be accomplished by offering more of the precursor solution. Hence, we prepared a 37 wt% NiO/SBA-15 sample using the same precursor solution as was used for S24/D, only now 1.8 ml.$g^{-1}$ instead of 1.0 ml.$g^{-1}$ was impregnated. The samples obtained after drying was labelled S37Ni/D. STEM results (not depicted) indicated that the impregnation and drying treatment had resulted in deposition of precursor exclusively inside the mesopores as no agglomerates were found at the external surface of the support particles. XRD (Table 1) showed that $Ni_3(NO_3)_2(OH)_4$ crystallites of 9 nm on average had formed. $N_2$-physisorption results (Table 2) showed a lower mesopore volume, but also an increased percentage of $V_{meso,bl}$ (41%) compared with sample S24Ni/D (19%). The results collected in Table 1 show that subsequent thermal treatment in air flow led to large NiO particles of about 15 to 60 nm at the exterior surface of the support particles and rodlike particles inside the mesopores, whereas treatment in 1 vol% NO/He flow yielded highly dispersed NiO particles of 3 to 5 nm. It should be noted

that accurate size determination with STEM was somewhat hampered by the high density of NiO particles inside the mesopores. With XRD line-broadening average NiO crystal sizes of 11 and 4 nm were found for the air and NO/He treated samples, respectively. Finally, with $N_2$-physisorption some (partial) pore blocking was observed (27%) with the NO/He treated sample presumably due to the high density of small NiO particles, but significantly less than after calcination in air (84%). Thus, we concluded that thermal treatment in 1 vol% NO/He of dried impregnate that was prepared by offering a quantity of precursor solution more than twice the pore volume enabled preparation of uniformly and highly dispersed SBA-15 supported catalysts with a NiO loading of 37 wt%.

*Conventional silica support*

Next, we extended our study to the preparation of conventional silica gel supported NiO catalysts. As air calcination is the standard method for the preparation of metal oxides from nitrate precursors we used samples treated accordingly as a benchmark. A conventional support silica gel powder was selected with a porosity ($0.90\ cm^3.g^{-1}$) and pore size distribution (7 nm) comparable to that of SBA-15. The silica gel powder was impregnated to incipient wetness, and dried at 120 °C. The dried impregnate was labelled G28Ni/D and displayed an NiO loading of 28 wt%. STEM analysis suggested that the precursor was relatively homogeneously distributed as no agglomerates of $Ni_3(NO_3)_2(OH)_4$ were found, though it should be noted that characterisation was cumbersome due to the heterogeneity of the support. XRD results (Table 1) showed that 12 nm $Ni_3(NO_3)_2(OH)_4$ crystals were present. XRD line-broadening of the peaks present in the pattern of the air calcined product (sample G28Ni/D-$C_{air}$) showed that NiO crystals of 15 nm on average were obtained. STEM analysis indicated that NiO particles were present with sizes ranging from about 7 to 70 nm. Hence, it was clear that sintering and redistribution had taken place and, compared with the SBA-15 supported samples it appeared more extensive presumably due to the inter-connected pore system. The sample treated under an NO/He flow (1 vol%) was labelled S28Ni/D-$C_{NO/He}$ and contained small NiO particles of 3 to 5 nm. These STEM observations were in line with XRD results, which showed that NiO crystallites of 4 nm on average were present. When a spherical geometry is assumed for the 12 nm $Ni_3(NO_3)_2(OH)_4$ crystals and a density of $3.5\ g.cm^{-3}$, the observed NiO (density= $6.7\ g.cm^{-3}$) crystal size of 4 nm was unexpected. However, layered hydroxide crystallites such as $Ni_3(NO_3)_2(OH)_4$ typically are anisotropic. As a result the small particles might have formed by breaking-up of these particles. Unfortunately, the XRD diffraction lines did not allow estimation of the aspect ratios of the $Ni_3(NO_3)_2(OH)_4$ phase to support this.

We conclude from the results obtained with silica gel support that the NO/He method is valid for conventional supports too. In addition, the results showed that the pore geometry of the support had little effect on the final NiO particle sizes obtained via this method.

*Significance for Co catalysts and carbon supports*

As poor metal (oxide) dispersions have been reported too for Co-based catalysts prepared from cobalt nitrate salts[23,24], we also investigated the usefulness of the NO/He treatment for the preparation of highly dispersed $Co_3O_4$ catalysts. Moreover, we looked into the importance of the precursor-support interactions for the NO/He method by carrying out experiments with carbon nanofiber supports that display a relatively poor interaction with the cobalt nitrate precursor compared to silica.

We started with impregnating SBA-15 to incipient wetness with an aqueous $[Co(OH_2)_6](NO_3)_2$ solution to yield a $Co_3O_4$ loading of 19 wt%. After drying at 70 °C for 12 hours a purple product (S19Co/D) was obtained indicating that a cobalt nitrate hydrate had formed presumably with composition $Co(NO_3)_2.6H_2O$ or $Co(NO_3)_2.4H_2O$. However, this could not be confirmed with XRD as no crystalline phase was detected. STEM analysis indicated that precursor had been deposited inside the mesopores as no agglomerates were found at the external surface of the support particles. Next,

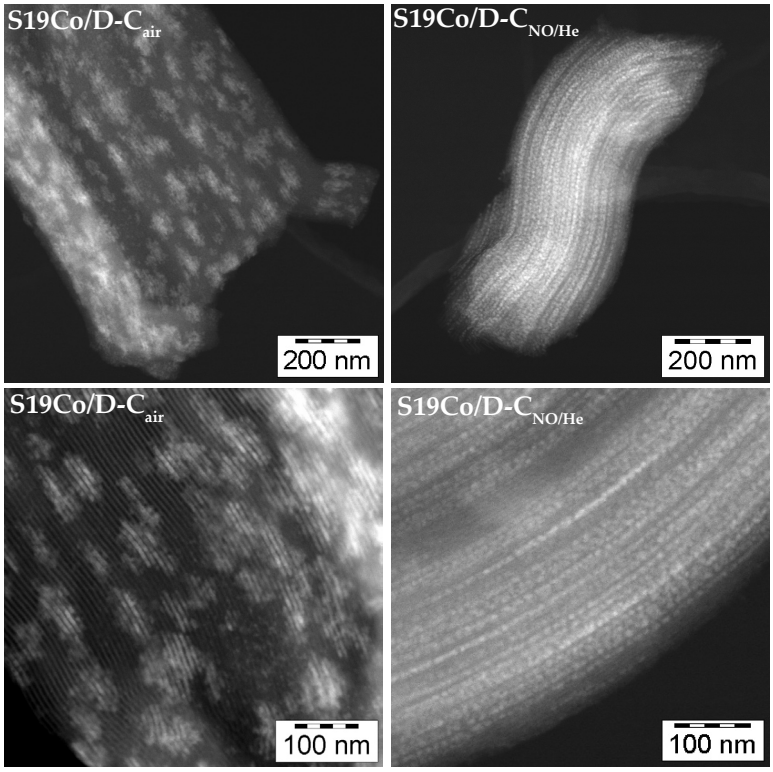


*Figure 4.* HAADF-STEM images recorded of samples S15Co/D-$C_{air}$ and S19Co/D-$C_{NO/He}$ after heat treatment at 450 °C of dried impregnate S19Co/D in air flow or in 1 vol% NO/He flow, respectively.

the dried impregnate was heat treated in air flow or in 1 vol% NO/He flow, and the products were labelled S19Co/D-$C_{air}$ and S19Co/D-$C_{NO/He}$, respectively. XRD analysis showed that $Co_3O_4$ crystals had formed of 10 nm (air) and 5 nm (NO/He). HAADF-STEM images of the two samples are depicted in Figure 4. Comparison between the two samples showed that similar results were obtained as with Ni; air calcination led to a poor $Co_3O_4$ dispersion, whereas the NO/He treatment yielded small particles of 3 to 5 nm. Contrary to the calcined NiO/SBA-15 samples, sintering and redistribution predominantly took place inside the mesopores resulting in large rodlike particles with lengths ranging from about 10 to 100 nm as shown in the bottom-left frame of Figure 4. Moreover, the sintering appeared to have led to $Co_3O_4$ patches within the SBA-15 particles. $N_2$-physisorption (Table 2) confirmed the presence of rodlike $Co_3O_4$ particles after calcination as 82% of the mesopore volume was (partially) blocked, whereas after treatment in NO/He no plugging of the mesopores was observed.

With silica gel powder similar experiments were carried out and after impregnation and drying also a purple product was obtained (G23Co/D) containing an amorphous cobalt nitrate phase. Subsequent calcination in air flow or thermal treatment in 1 vol% NO/He flow yielded $Co_3O_4$ with crystal sizes (Table 1) of 11 nm (G23Co/D-$C_{air}$) and 5 nm (G23Co/D-$C_{NO/He}$). STEM confirmed these observations as particles sizes of about 8 to 60 nm and 3 to 5 nm were observed for the air flow and NO/He flow treated samples, respectively. Hence, similar as with Ni, the results could be transferred to a conventional silica gel support.

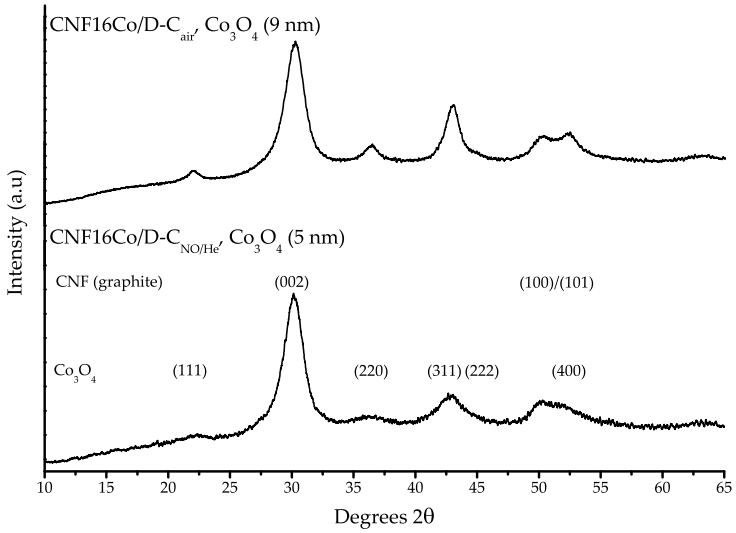


*Figure 5.* XRD patterns of CNF supported $Co_3O_4$ samples CNF16Co/D-$C_{air}$ and CNF16Co/D-$C_{NO/He}$ prepared through heat treatment at 200 °C in air flow or in 1 vol% NO/He flow.

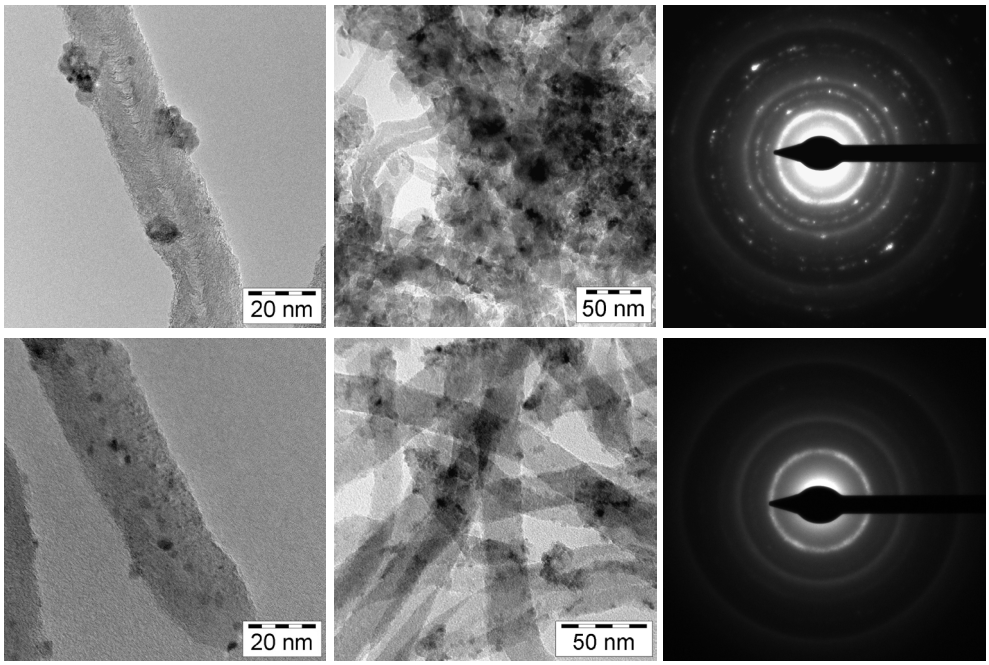


*Figure 6.* TEM images and electron-diffraction patterns of CNF supported $Co_3O_4$ samples CNF16Co/D-$C_{air}$ (top row) and CNF16Co/D-$C_{NO/He}$ (bottom row) prepared via thermal treatment at 200 °C in air flow or in 1 vol% NO/He flow. The center images were used for collection of the electron-diffraction patterns (right-frame).

Finally, CNF was impregnated with aqueous $[Co(OH_2)_6](NO_3)_2$ solution and dried at 70 °C. Again, an amorphous precursor phase had formed after drying. Parts of the dried impregnate that were heat treated in air flow or in 1 vol% NO/He flow were denoted CNF16Co/D-$C_{air}$ and CNF16Co/D-$C_{NO/He}$, respectively, and contained 16 wt% $Co_3O_4$. A maximum temperature of 200 °C was used to minimise gasification of the carbon support. With XRD (Figure 5) average $Co_3O_4$ crystal sizes of 9 nm (air) and 5 nm (NO/He) were found. Typical STEM images of both the samples are depicted in Figure 6 together with electron diffraction patterns. The images indicated that the NO/He method was also beneficial to the $Co_3O_4$ dispersion as particles of about 5 to 15 nm were found after air calcination and 3 to 6 nm after NO/He heat treatment. The large difference in the number of diffraction spots found in the electron diffraction patterns supported these findings. Hence, we concluded that the role of NO was not dependent on specific precursor-support interactions.

*Impact of NO concentration on the NiO particle size*

Thus far, we used an NO concentration of 1 vol% and GHSV of 24,500 $h^{-1}$ to investigate the relevance of the gas atmosphere during thermal nitrate decomposition

for different systems. However, the experiments with stagnant air and an air flow (see Figure 1 and 2) had already demonstrated that maintaining relatively high concentrations of gaseous decomposition products ($NO_2$, $H_2O$ and $O_2$) favoured formation of large particles. Therefore, insight into the interplay between these products and the added NO was important. Hence, we carried out experiments in which the concentration of NO in He was varied during thermal treatment at 450 °C (ramp= 1 °C.min$^{-1}$) while maintaining a constant GHSV of 24,500 h$^{-1}$, and experiments where the NO concentration was kept constant at 1 vol% while varying the GHSV between 1,700 to 24,500 h$^{-1}$. The impact of these parameters on the final NiO dispersion was monitored by XRD. For these experiments small quantities of silica gel supported sample G28Ni/D (28 wt% NiO) were used as its well-defined sieve fraction ensured plug-flow conditions. The results have been plotted in Figures 7 and 8. As shown in Figure 7, with pure He an average NiO crystal size of almost 11 nm was obtained. Adding a small amount of 0.05 vol% NO to the He flow had little impact, however, doubling the concentration to 0.1 vol% led to a decrease of more than a factor of two. Further increasing the concentration to 1 vol% had little effect as the average crystal size remained constant. Thus, with a GHSV of 24,500 h$^{-1}$ only 0.1 vol% NO/He was needed to obtain silica gel supported NiO crystals of 4 nm on average at a loading of 28 wt%.

The results obtained after varying the GHSV while maintaining a constant NO concentration of 1 vol% have been plotted in Figure 8. The results demonstrated that the obtained average NiO crystal sizes with NO/He were always smaller than with pure He. With the latter NiO crystal sizes started to increase at GHSVs lower than ~14,000 h$^{-1}$. Although decreasing the GHSV by a factor of 2 had a moderate impact on the crystal size, further decrease resulted in severe sintering and redistribution, and 14 nm NiO crystals were obtained at a GHSV of 1,700 h$^{-1}$. For the samples treated in

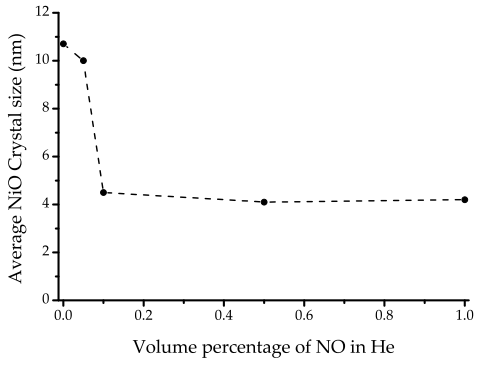


*Figure 7.* Relation between the NO concentration in the He flow and the average NiO crystal size obtained after thermal treatment at 450 °C of sample G/D.

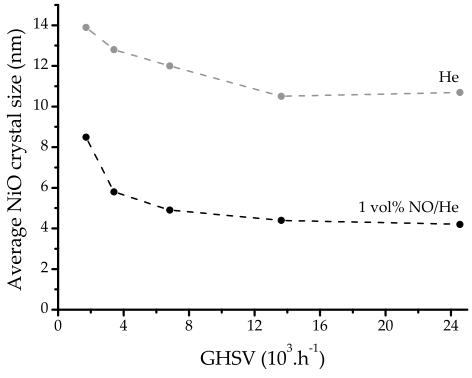


*Figure 8.* Relation between the GHSV during thermal treatment at 450 °C of sample G/D in He (grey) or in NO/He (black) and the average NiO crystal size obtained.

1 vol% NO/He flow a similar trend was observed, however, the increase of the NiO crystal size was much smaller at all GHSV. Lowering of the GHSV by more than a factor of 7 from 24,500 to 3,400 $h^{-1}$ led only to a moderate size increase. Only at values lower than 3,400 $h^{-1}$ substantial rise of the NiO crystal size was observed, and at a GHSV of 1700 $h^{-1}$ an average crystallite size of almost 9 nm was obtained, still being smaller than obtained with pure He flow. Thus, with NO substantial smaller crystallites could be obtained irrespective of the GHSV, but the highest dispersion was obtained with a GHSV ≥6,800 $h^{-1}$. Moreover, these results suggest the relation between the NiO crystal size and the concentration of gaseous decomposition products, and the necessity of a minimum local NO concentration to moderate the $Ni_3(NO_3)_2(OH)_4$ decomposition (see chapter 5 for details).

*Relevance for catalysis: hydrogenation of soybean oil over $Ni/SiO_2$*

Finally, the relevance for catalysis of the NO/He treatment was studied by comparing the activities of the reduced silica gel supported NiO catalysts prepared either through calcination in air flow or heat treatment in 1 vol% NO/He flow in the hydrogenation of soybean oil with an Iodine Value (IV) of 133. The IV value is a measure for the number of unsaturated double bonds present in the oil. Small quantities of silica gel supported samples G28Ni/D-$C_{air}$ and G28Ni/D-$C_{NO/He}$ were used after high-temperature reduction with $H_2$, and hydrogenation was carried out at 140 °C. The amount of $H_2$ absorbed into the oil was monitored and the test was terminated once the IV had dropped to 79. The hydrogenation time to reach the IV of 79 was used as a measure of the activity of the catalyst, and the results are shown in Table 3. The percentage of trans-isomers and melting points of the fats turned out to be almost identical and had not been affected by the preparation method. However, the hydrogenation times showed that preparation of $Ni/SiO_2$ catalysts via the NO/He method instead of in air flow led to a reduction of ~30% of the time needed to reach the IV of 79. Hence, the NO/He thermal treatment resulted in a much higher hydrogenation activity of the final $Ni/SiO_2$ catalyst.

*Table 3.* Soybean oil hydrogenation results of silica gel supported Ni catalysts.

| Catalyst | Hydrogenation time (min.) | End IV ($gI_2.100\ g^{-1}$) | Trans (%) | Melting point (°C) |
|---|---|---|---|---|
| G28Ni/D-$C_{air}$ | 148 | 79.0 | 34.8 | 45.4 |
| G28Ni/D-$C_{NO/He}$ | 101 | 79.2 | 37.7 | 45.0 |

## Conclusions

A method comprising of heat treatment of supported nitrate precursor in NO/He flow was described that allowed preparation of supported NiO and $Co_3O_4$ nanoparticles of 3 to 5 nm at loadings of 24 to 37 wt% and 16 to 23 wt%, respectively, depending on the support used.

The preparation of NiO/SBA-15 *ex* nitrate was studied in detail. After impregnation, followed by drying at 120 °C $Ni_3(NO_3)_2(OH)_4$ crystallites of 9 nm were found exclusively inside the mesopores of SBA-15. Their size indicated confinement by the pore walls. Upon calcination in air flow severe sintering and redistribution took place resulting in large NiO particles (10 to 35 nm) outside the mesopores, and rodlike NiO particles inside the mesopores. Use of a flow of pure He instead of air showed that exclusion of $O_2$ had an inhibiting effect on the NiO migration out of the mesopores, but the majority of NiO inside the mesopores still had sintered to form the rodlike NiO particles. However, smaller and more spherical NiO particles were found too. XRD supported these findings as the diffraction lines had a broadened onset, which is indicative for a bimodal crystal size distribution. With 1 vol% of NO/He flow small NiO particles of 3 to 5 nm were found exclusively inside the mesopores. $N_2$-physisorption results of the NiO/SBA-15 samples treated in air, He or NO/He flow supported the results as cavitation due to the rodlike NiO particles was found in all samples expect in the NO/He treated ones.

The versatility of the NO/He method was demonstrated as SBA-15, silica gel and CNF supported Ni and Co systems yielded similar results. Results obtained with silica gel showed that with a 1 vol% NO/He flow NiO crystals of 4 nm could be obtained at GHSV values of ≥6800 $h^{-1}$. Though lowering of the GHSV resulted in an increase of the average NiO crystal size, the particles were still significantly smaller than obtained in pure He flow. When a GHSV of 24,500 $h^{-1}$ was applied, 0.1 vol% of NO sufficed to obtain silica gel supported NiO crystals of 4 nm at a loading of 28 wt%.

Hydrogenation tests with soybean oil showed that the NiO on silica gel catalysts prepared via the NO/He method yielded, after high-temperature reduction, $Ni/SiO_2$ catalysts that displayed higher activity as a reduction of ~30% of the hydrogenation time was observed compared to the product treated through standard calcination in air. Hence, thermal decomposition of supported metal nitrates in a NO/He flow showed to be a versatile and robust method to obtain highly dispersed metal oxide particles and more active metal catalysts when followed by high-temperature reduction, and is a promising technique for the preparation of a wide range of metal (oxide) nanoparticles.

**Acknowledgements**

Jos van Dillen is kindly thanked for his guidance and support. Bart Zwijnenburg and Martin Lok of Johnson-Matthey Catalysts are kindly thanked for the hydrogenation experiments and valuable discussions. Hans Meeldijk is acknowledged for assistance with TEM. Johan den Breejen is thanked for providing the CNF supported cobalt nitrate impregnate.

**References**

1. Bell, A.T. *Science* **2003**, *299*, 1688-1691.
2. Schögl, R.; Abd Hamid, S.B. *Angew. Chem. Int. Ed.* **2004**, *43*, 1628-1667.
3. Ying, J.Y. *Chem.Eng. Sci.* **2006**, *61*, 1540-1548.
4. De Jong, K.P. *Curr. Op. Solid Mat. Sci.* **1999**, *4*, 55-62.
5. Serp, P.; Kalck, P.; Feurer, R. *Chem. Rev.* **2002**, *102*, 3085-3128.
6. Schreier, M.; Regalbuto, J.R. *J. Catal.* **2004**, *225*, 190-202.
7. Carrier, X.; Lambert, J.F.; Che, M. *J. Am. Chem. Soc.* **1997**, *119*, 10137-10146.
8. Hermans, L.A.M.; Geus, J.W. *Stud. Surf. Sci. Catal.* **1979**, *3*, 113-130.
9. Van der Lee, M.K.; Van Dillen, A.J.; Bitter, J.H.; De Jong, K.P. *J. Am. Chem. Soc.* **2005**, *127*, 13573-13582.
10. Nares, R.; Ramírez, J.; Gutiérrez-Alejandre, A.; Louis, C.; Klimova, T. *J. Phys. Chem. B* **2002**, *106*, 13287-13293.
11. Lok, C.M. *Stud. Surf. Sci. Catal.* **2004**, *147*, 283-288.
12. Bourikas, K.; Kordulis, C.; Lycourghiotis, A. *Catal. Rev.* **2006**, *48*, 363-444.
13. Ertl, G.; Knözinger, H.; Weitkamp, J. *Preparation of solid catalysts* **1999**, Weinheim, Germany, Wiley-VCH.
14. Clause, O.; Kermarec, M.; Bonnevoit, L.; Villain, F.; Che, M. *J. Am. Chem. Soc.* **1992**, *114*, 4709-4717.
15. Carriat, J.Y.; Che, M.; Kermarec, M.; Verdaguer, M.; Michalowicz, A. *J. Am. Chem. Soc.* **1998**, *120*, 2059-2070.
16. Lekhal, A.; Glasser, B.J.; Khinast, J.G. *Chem. Eng. Sci.* **2004**, *59*, 1063-1077.
17. Burattin, P.; Che, M.; Louis, C. *J. Phys. Chem. B* **1997**, *101*, 7060-7074.
18. Li, G.; Hu, L.; Hill, J.M. *Appl. Catal. A* **2006**, *301*, 16-24.
19. Van Dillen, A.J.; Terörde, R.J.A.M.; Lensveld, D.J.; Geus, J.W.; de Jong, K.P. *J. Catal.* **2003**, *216*, 257-264.
20. Chen, I.; Lin, S-Y.; Shiue, D-W. *Ind. Eng. Chem. Res.* **1988**, *27*, 926-929.
21. Poels, E.K.; Dekker, J.G.; Van Leeuwen, W.A. *Stud. Surf. Sci. Catal.* **1991**, *63*, 205-214.
22. Vos, B.; Poels, E.K.; Bliek, A. *J. Catal.* **2001**, *198*, 77-88.
23. Reinalda, D.; Kars, J. *U.S. Patent* No. 5,021,387 **1991**.

24. Van de Loosdrecht, J.; Barradas, S.; Caricato, E.A.; Ngwenya, N.G.; Nkwanyana, P.S.; Rawat, M.A.S.; Sigwebela, B.H.; Van Berge, P.J.; Visagie, J.L. *Top. Catal.* **2003**, *26*, 121-127.
25. Louis, C.; Cheng, Z.X.; Che, M. *J. Phys. Chem.* **1993**, *97*, 5703-5712.
26. Wang, Y.; Noguchi, M.; Takahashi, Y.; Ohtsuka, Y. *Catal. Today* **2001**, *68*, 3-9.
27. Ohtsuka, Y.; Takahashi, Y.; Noguchi, M.; Arai, T.; Takasaki, S.; Tsubouchi, N.; Wang, Y. *Catal. Today* **2004**, *89*, 419-429.
28. Van den Brink, P.J.; Scholten, A.; Van Wageningen, A.; Lamers, M.D.A.; Van Dillen, A.J.; Geus, J.W. *Stud. Surf. Sci. Catal.* **1991**, *63*, 527-537.
29. Chen, H-C.; Anderson, R.B. *J. Catal.* **1976**, *43*, 200-206.
30. Balakos, M. W.; Hernandez, E.E. *Catal. Today* **1997**, *35*, 415-425.
31. Fouilloux, P. *Appl. Catal.* **1983**, *8*, 1-42.
32. Allen, R.R. *J. Am. Oil Chem. Soc.* **1986**, *63*, 1328-1332.
33. Iglesia, E. *Appl.Catal. A* **1997**, *161*, 59-78.
34. Kroschwitz, I.; Howe-Grant, M. *Kirk-Othmer encyclopedia of chemical technology* **1996**, Wiley & Sons, New York, 4th edn.
35. Bezemer, G.L.; Bitter, J.H.; Kuipers, H.P.C.E.; Oosterbeek, H.; Holewijn, J.E.; Xu, X.; Kapteijn, F.; Van Dillen, A.J.; De Jong, K.P. *J. Am. Chem. Soc.* **2006**, *128*, 3956-3964.
36. Balakos, M. W.; Hernandez, E.E. *Catal. Today* **1997**, *35*, 415-425.
37. Zhao, D.; Feng, J.; Huo, Q.; Melosh, N.; Fredrickson, G.H.; Chmelka, B.F.; Stucky, G.D. *Science* **1998**, *279*, 548-552.
38. Toebes, M.L.; Bitter, J.H.; Van Dillen, A.J.; De Jong, K.P. *Catal. Today* **2002**, *76*, 33-42.
39. Jaroniec, M.; Kruk, M.; Olivier, J.P.; Koch, S. *Stud. Surf. Sci. Catal.* **2000**, *128*, 71-80.
40. Barrett, E.P.; Joyner, L.S.; Halenda, P.P. *J. Am. Chem. Soc.* **1951**, *73*, 373-380.
41. Harkins, W.D.; Jura, G. *J. Am. Chem. Soc.* **1944**, *66*, 1366-1373.
42. Kruk, M.; Jaroniec, M.; Sayari, A. *Langmuir* **1997**, *13*, 6267-6273.
43. Lippens, B.C.; De Boer, J.H. *J. Catal.* **1965**, *4*, 319-323.
44. Gallezot, P.; Prettre, M. *Bull. Soc. Chim. Fr.* **1969**, *2*, 407-411.
45. Estellé, J.; Salagre, P.; Cesteros, Y.; Serra, M.; Medina, F.; Sueiras, J.E. *Solid State Ionics* **2003**, *156*, 233-243.
46. Moreno, S.M.; Weyland, M.; Midgley, P.A.; Bengoa, J.F.; Cagnoli, M.V.; Gallegos, N.G.; Alvarez, A.M.; Marchetti, S.G. *Micron* **2006**, *37*, 52-56.
47. Impéror-Clerc, M.; Bazin, D.; Appay, M-D. ; Beaunier, P.; Davidson, A. *Chem. Mater.* **2004**, *16*,1813-1821.
48. Ravikovitch, P.I.; Neimark, A.V. *Langmuir* **2002**, *18*, 9830-9837.
49. Janssen, A.H; Yang, C.-M.; Wang, Y.; Schüth, F.; Koster, A.J. De Jong, K.P. *J. Phys. Chem. B* **2003**, *107*, 10552-10556.
50. Vradman, L.; Landau, M.V.; Kantorovich, D.; Koltypin, Y.; Gedanken, A. *Micropor. Mesopor. Mater.* **2005**, *79*, 307-318.

51. Van Der Voort, P.; Ravikovitch, P. I.; De Jong, K. P.; Benjelloun, M.; Van Bavel, E.; Janssen, A. H.; Neimark, A. V.; Weckhuysen, B. M.; Vansant, E. F. *J. Phys. Chem. B.* **2006**, *106*, 5873-5877.
52. Friedrich, H.; Sietsma, J.R.A.; De Jongh, P.E.; Verkleij, A.J.; De Jong, K.P. *J. Am. Chem. Soc.* **2007**, *129*, 10249-10254.
53. Sampling and analysis of commercial fats and oils method Cd 14d-99: *Rapid determination of isolated trans geometric isomers* **1999**.
54. Sampling and analysis of commercial fats and oils AOCS method Cc 3b-92: *Slip melting point ISO standard*.

# 5

# How NO affects the thermal decomposition of supported nickel nitrate to form uniform NiO nanoparticles

The influence of air, He and NO/He gas atmospheres on the decomposition of $Ni_3(NO_3)_2(OH)_4$ was investigated to explain their profound impact on the obtained NiO dispersion. By combining electron tomography with $N_2$-physisorption and XRD a consistent picture of the NiO distribution inside the mesopores was obtained as a function of the gas atmosphere. Predominantly rodlike NiO particles were obtained with air (9×35 nm) and He (9×20 nm), though pores containing smaller particles were found in the latter too. The NO/He treated samples exclusively contained well-distributed NiO particles (4 nm). TGA/MS results showed that $NO_2$, $N_2O$ and $H_2O$ gaseous decomposition products evolved in all cases, but more gradually in NO/He. *In situ* XRD experiments demonstrated that NO moderated the decomposition rate of $Ni_3(NO_3)_2(OH)_4$ into NiO and proceeded gradually contrary to air. DSC results revealed this effect too and suggested that decomposition in NO/He was less endothermic than in air. This might be explained by the exothermic scavenging of oxygen by NO. MS results were in line with this hypothesis as no $O_2$ was detected amongst the gaseous decomposition products in NO/He flow contrary to treatment in inert atmosphere.

## Introduction

Supported metal (oxide) catalysts are indispensable for the preparation of bulk and fine chemicals, and the reduction of environmental pollution.[1-3] Since catalytic processes take place only at the metal (oxide) surface and are often carried out at rather high temperatures, small as well as thermally stable metal (oxide) particles are important. Therefore, the particles are generally stabilised with high-surface area support materials such as $SiO_2$ and $\gamma$-$Al_2O_3$. Hence, preparation techniques often aim at obtaining catalysts that display a high dispersion of the active phase over the support, combined with a high loading. Supported metal (oxide) particles can be obtained by deposition from the vapour or liquid phase. Although Chemical Vapour Deposition (CVD) techniques[4] enable uniform deposition of the active phase or its precursor onto a support, the deposition from gaseous precursors is relatively complicated, and limited to low loadings. Catalyst preparation techniques are, therefore, mainly based on liquid phase processes and methods comprise of ion-adsorption[5,6], deposition-precipitation[7-9] and, impregnation and drying[10-14]. In particular the latter is often used as it enables high metal (oxide) loadings and its technical simplicity allows execution on an industrial scale. This technique involves impregnation of a support with a precursor-containing solution, followed by evaporation of the solvent. The dried impregnate is heat treated in air, often referred to as calcination, to convert the precursor into the desired metal oxide, optionally followed by a high temperature reduction treatment to obtain the metal in question.

The type of precursor has a large impact on the properties of the final metal (oxide). Small particles of 1 to 3 nm can be obtained when organic precursor complexes based on citric acid, nitrilotriacetic acid (NTA) and ethylenediamminetetraacetic acid (EDTA)[11], but only moderate loadings up to 10 wt% can be realised via single-step impregnations due to their limited solubility. Hence, aqueous solutions of inorganic salts are used when higher loadings are desired. In particular highly soluble nitrate salts are attractive as pure metal oxides can be obtained via facile and complete thermal decomposition in air. Regrettably, catalysts prepared as such display often poor metal dispersions, which has been ascribed to either redistribution during drying[11,15-18] or to sintering during the air calcination[19-23] step.

Ni-based catalysts are extensively used because of their activity in important processes such as the hydrogenation of fatty acids.[24-26] Using ordered mesoporous silica SBA-15 as model support, we recently studied the preparation of $Ni/SiO_2$ *ex* nitrate catalysts and found that the poor dispersion finds origin in severe sintering and redistribution during the air calcination treatment. Moreover, we identified that sintering could be reduced using an He atmosphere, but that treatment in NO/He fully prevented sintering resulting in small NiO particles of 4 nm at a loading of 24 wt%.[28,29]

Although the ordered structure of SBA-15 allowed clear differentiation between NiO and support with standard Transmission Electron Microscopy (TEM), the technique

cannot give full insight into the NiO distribution throughout individual pores, as it yields a two-dimensional projection of the three-dimensional SBA-15 structure. This problem can be overcome using Electron Tomography (ET), sometimes referred to as 3D-TEM, as this technique allows three-dimensional imaging of the interior of porous structures such as SBA-15.[30-32] Hence, ET could yield valuable insight into the impact of the air, He and NO/He atmospheres on the local distribution of NiO inside the mesopores and type of NiO particles formed. When combined with bulk-characterisation techniques such as $N_2$-physisorption and XRD, a representative picture can be obtained.

In addition, it remained an open question why NO has such a large impact on the final NiO dispersion. Hence, we studied the decomposition reaction of the $Ni_3(NO_3)_2(OH)_4$ precursor under different atmospheres using TGA/MS, *in situ* XRD and DSC characterisation techniques. Moreover, we varied the concentration of NO, and the gas flow rate. Based on these results we propose an explanation for the impact of NO on the nitrate decomposition to form uniform NiO particles.

## Experimental

*Sample preparation*

SBA-15 (total pore volume= 0.78 $cm^3.g^{-1}$ and average pore diameter= 9 nm) was synthesised by following a procedure of Zhao *et al.*[33]. 8 g of $PEO_{20}PPO_{70}PEO_{20}$ (PEO= poly(ethylene oxide) and PO= poly(propylene oxide)) tri-block copolymer obtained from Aldrich was dissolved in 250 ml demineralised water of 40 °C. After the solution had become clear, 48 g of concentrated HCl (Merck) was added, followed by the addition of 21.5 ml of tetraethyl orthosilicate (Acros). Next, the mixture was stirred for 20 hours at 40 °C after which it was transferred to an oven for further reaction at 80 °C for 48 hours. The solid product was collected from the suspension by filtration, washed, dried in air for 12 hours at 80 °C, and calcined for 6 hours at 550 °C. Davicat 1404SI silica gel (total pore volume= 0.90 $cm^3.g^{-1}$ and average pore diameter= 7 nm) was used as received from Grace-Davison.

Prior to impregnation, the supports were dried for 2 hours in dynamic vacuum at 80 °C to remove physisorbed water. The precursor solution was prepared by dissolving $Ni(NO_3)_2.6H_2O$ (Acros) in demineralised water. SBA-15 and silica gel quantities of 0.25 g and 1.00 g were impregnated in static vacuum using 1.00 $ml.g^{-1}$ and 1.25 $ml.g^{-1}$ of precursor solution to provide 24 wt% and 28 wt% NiO/SiO2, respectively. The fresh impregnates were dried in static air by increasing the temperature at a rate of 1 $°C.min^{-1}$ to 120 °C. The samples were kept at the final temperature for 12 hours.

Small quantities of 40 mg (SBA-15) and 100 mg (silica gel) of the dried impregnates were calcined in air using a plug-flow reactor (length 17 cm and diameter 1 cm) and flow of 90 $ml.min^{-1}$. The samples were heated to 450 °C with a ramp of 1 $°C.min^{-1}$ and kept at 450 °C for 4 hours. The same heating programme was used for the thermal treatments in He flow or in NO/He flow. The gas-hourly-space-velocities (GHSV)

and NO concentrations were varied between 1,700 - 24,500 $h^{-1}$ and 0.01 - 1 vol%, respectively. Apparent bulk densities of 0.46 and 0.09 $g.cm^{-3}$ for silica gel and SBA-15, respectively, were used to calculate the GHSV.

All samples were labelled using sample codes. An example of a sample code is S/D-$C_{He}$. The first part denotes the support: S= SBA-15 and G= silica gel support, whereas the second part indicates the thermal treatments that were applied: D= drying in static air, $C_{He}$= heat treatment in He flow.

*Characterisation*

Powder X-ray diffraction (XRD) patterns were obtained at room temperature from 5 to 90° 2θ with a Bruker-AXS D8 Advance X-ray Diffractometer setup using Co-$K_{\alpha 12}$ radiation. The patterns were baseline-corrected for the amorphous SiO2 background. The average $Ni_3(NO_3)_2(OH)_4$ and NiO crystal sizes were calculated according to the Scherrer equation ($k$=1) using the most intense (001) and (200) diffraction lines at 2θ= 14.9° and 50.8°, respectively. For *in situ* XRD experiments the diffractometer was equipped with an Anton-Paar XRK reaction chamber. Sample S/D (20 mg) was heated in air flow or in 1 vol% NO/He flow from room temperature to 248 °C at a controlled rate of 1 °C.$min^{-1}$ and kept isothermal until decomposition of $Ni_3(NO_3)_2(OH)_4$ and formation of NiO had completed. During these experiments the reaction chamber was continuously flushed using a flow of 90 ml.$min^{-1}$.

TEM tomography grids were prepared by applying 10 nm sized colloidal gold particles from suspension to a Quantifoil R2/1 carbon film supported on a parallel bar Cu TEM grid. After drying in air, a small amount of sample was deposited directly onto the grid. Excess catalyst was shaken-off before inserting the TEM grid into a Fischione, Model 2020, advanced tomography holder. ET was performed in bright-field TEM mode, and series of TEM images (tilt-series) were acquired by rotating the specimen over a tilt range of at least ±70° at increments of 1°. Images were recorded at each tilt step on a 2048 pixel × 2048 pixel TVIPS CCD camera using Xplore3D software (FEI). The defocus was set between -130 nm and -200 nm depending on the size of the examined SBA-15 particle to keep the entire object in underfocus. The nominal magnification was 29000× which corresponds to a pixel size of 0.27 nm. Images of the tilt-series were aligned with respect to a common origin and rotation axis using the 10 nm gold particles as fiducial markers. Finally the aligned tilt-series was binned to 0.54 nm pixel size prior to reconstruction of the three-dimensional volume. Alignment and reconstruction by filtered backprojection was performed in IMOD.[34]

$N_2$-physisorption measurements were performed at -196 °C, using a Micromeritics Tristar 3000 apparatus. Prior to analysis the samples were dried in He flow for 14 hours at 120 °C. The pore size distribution was derived from the adsorption branch of the isotherm using non-local density functional theory (NL-DFT). A model developed by Jaroniec *et al.*[35] for ordered mesoporous silica supports with cylindrical pore geometry was used. This model fitted our data well as the results depended only slightly on the regularisation contraint. The pore diameter of the mesoporous

channels of SBA-15 was defined by the value at which the maximum in differential pore volume was observed. The micro- and meso-porosity were defined as the volume present in pores smaller than 2 nm, and between 2 and 50 nm, respectively. There is no standard method yet for the determination of blocked mesopore volume ($V_{meso,bl}$). We used BJH theory[36] with the Harkins and Jura[37] thickness equation and the Kruk-Jaroniec-Sayari[38] correction for ordered mesoporous siliceous materials to calculate from the desorption branch the cumulative pore volume as a function of the pore size. From this we determined $V_{meso,bl}$ considering that the pores with a diameter of 2 to 5 nm are due to volume in (partially) blocked pores. The mesopore surface areas were calculated with the t-method[39] using thickness ranges of 0.35-0.55.

Thermogravimetric analysis (TGA) was carried out using a Perkin-Elmer Pyris 1 apparatus. Typically a quantity of 5 mg sample was heated from room temperature to 500 °C using a ramp of 5 °C.min$^{-1}$. The off-gas was simultaneously analysed with a quadrupole Pfeiffer Omnistar mass spectrometer, and ion currents were recorded for $m/z$ values ($m$= molar mass of X$z$+ ion, $z$= charge of the ion) of 14, 15, 16, 17, 18, 28, 30, 32, 44, 46, 62 and 63. Differential scanning calorimetry (DSC) experiments were done using a Q200 Thermal Analysis Instruments apparatus. Small quantities (5 mg) of sample S/D were heated to 300 °C with 1 °C.min$^{-1}$ under a 90 ml.min$^{-1}$ flow of either air or 1 vol% NO/He.

## Results and discussion

Figure 1 shows the XRD pattern of the dried impregnate S/D obtained after impregnation of SBA-15 with aqueous $[Ni(OH_2)_6](NO_3)_2$ solution and subsequent drying at 120 °C. The results of XRD line-broadening analysis obtained for all the samples have been summarised in Table 1 together with TEM particle size estimations. The diffractograms of sample S/D showed that nickel nitrate hydroxide, also referred to as basic nickel nitrate, with composition $Ni_3(NO_3)_2(OH)_4$ had formed.[40,41] Line-broadening analysis of the (001) diffraction line indicated that the crystallites were 9 nm on average, which agreed well with the average pore diameter of 9 nm as determined from $N_2$-physisorption, and suggested confinement by the pore walls.

The second step in the preparation involved heat treatment of the dried impregnate at 450 °C to convert $Ni_3(NO_3)_2(OH)_4$ into NiO:

$$Ni_3(NO_3)_2(OH)_4\ (s) \longrightarrow 3\ NiO\ (s) + 2\ NO_2\ (g) + \tfrac{1}{2}\ O_2\ (g) + 2\ H_2O\ (g) \qquad (1)$$

In Figure 1, the XRD patterns are shown of the NiO/SBA-15 products obtained using different gas atmospheres during this step. It should be noted that the same flow rates were used in all the plug-flow experiments unless otherwise stated. Line-broadening analysis showed that thermal decomposition in stagnant air

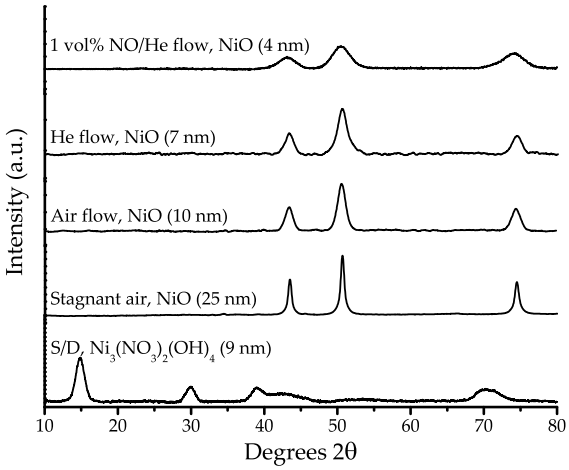


*Figure 1.* XRD patterns of SBA-15 supported impregnate S/D after drying at 120 °C, and NiO/SBA-15 samples obtained thereof after thermal treatment at 450 °C using different gas atmospheres. The resulting average crystal sizes and gas atmospheres have been indicated.

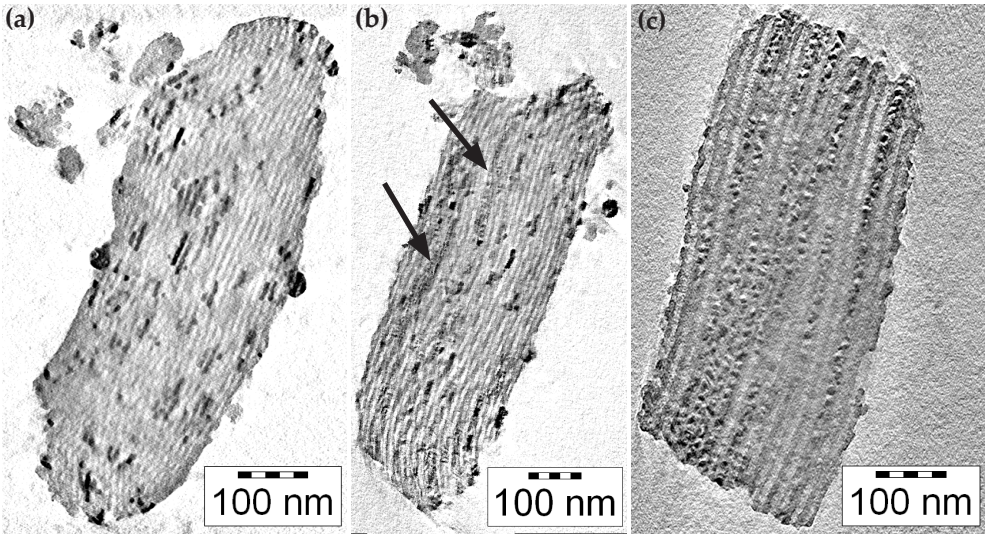


*Figure 2.* ET slices of NiO/SBA-15 samples obtained after calcination in air flow (a), thermal treatment in He flow (b), and heat treatment in 1vol% NO/He flow (c). The arrows indicate regions containing small NiO particles.

resulted in relatively large NiO crystals of 25 nm on average, use of an air flow led to crystals of 10 nm and with a pure He flow an average crystallite size of 7 nm was obtained. Adding 1 vol% of NO to the He flow resulted in the formation of NiO crystallites of 4 nm on average. The observed differences showed the impact of the gas atmosphere on the degree of sintering and redistribution during thermal decomposition of $Ni_3(NO_3)_2(OH)_4$.

In Figure 2, three representative 0.54 nm thick cross-sections through the ET reconstructions are given of the NiO/SBA-15 samples that were treated in air (sample S/D-$C_{air}$), pure He (S/D-$C_{He}$) or 1 vol% NO/He (S/D-$C_{NO/He}$). A non-uniform distribution of NiO over the mesopores was found in all three samples, presumably due to non-uniform wetting during impregnation as was discussed in chapter 2. The NiO/SBA-15 sample obtained through air calcination contained both large NiO particles outside the mesopores and particles retained inside the pores. The ET reconstruction showed that all the NiO particles inside the mesopores were rodlike with a diameter of 9 nm due to confinement by the pore walls, and their length varied between 10 to 70 nm. No special location of the NiO particles, for instance at the pore mouths of the mesopores, was observed. After thermal treatment in He (Figure 2b) three types of NiO particles could be identified; large particles outside the mesopores and, rodlike and more spherical particles inside the mesopores. Again, the rodlike NiO particles were confined by the pore walls, but their length had decreased to about 10 to 40 nm. Areas containing smaller and more spherical NiO particles were found too, as indicated by the arrows in Figure 2b. XRD (Figure 1) supported the ET findings as the onset of the diffraction lines had broadened indicating a bimodal particle size distribution. Finally, Figure 2c depicts a slice taken from a three-dimensional reconstruction of a NiO/SBA-15 particle prepared with

*Table 1.* Overview of applied thermal treatments, compositions and XRD and STEM results.

| **Samples** | **Thermal treatments** | **Nickel phase** | **Loading (wt%)** | **Size (nm)** | |
|---|---|---|---|---|---|
| | | | | $d_{XRD}$ | $d_{TEM}$ |
| **SBA-15** | | | | | |
| S/D | drying | $Ni_3(NO_3)_2(OH)_4$ | 34 | 9 | - |
| S/D-$C_{air}$ | drying/calcination in air | NiO | 24 | 10 | 10-35 |
| S/D-$C_{He}$ | drying/heat treatment in He | NiO | 24 | 7 | 10-25 |
| S/D-$C_{NO/He}$ | drying/heat treatment in 1 vol% NO/He | NiO | 24 | 4 | 3-5 |
| **Silica gel** | | | | | |
| G/D | drying | $Ni_3(NO_3)_2(OH)_4$ | 39 | 12 | - |
| G/D-$C_{air}$ | drying/calcination in air | NiO | 28 | 15 | 7-70 |
| S/D-$C_{NO/He}$ | drying/heat treatment in 1 vol% NO/He | NiO | 24 | 4 | 3-5 |

NO/He. Exclusively small NiO particles were found in this sample and although particles between 2 to 7 nm were found, detailed particle-size analysis published elsewhere[42] showed that 80% of the particles were 3 to 5 nm. Moreover, a volume weighted NiO size maximum of 4 nm was found, which was in good agreement with the average crystal size of 4 nm derived from the XRD pattern shown in Figure 1.

Combination of the ET results with characterisation results from $N_2$-physisorption and XRD (Table 2) allowed us to put together representative pictures of the NiO particle distributions inside the mesopores of the air, He and NO/He treated samples. In Figure 3, ET slices and $N_2$-physisorption results of the samples are shown together with schematic illustrations that represent the NiO distribution inside the pores as a function of the gas atmosphere. With ET (Figure 3a) we found in the air treated sample many voids between the rodlike NiO particles situated in the same pore. Compared to the pristine SBA-15 that contained all features typical for SBA-15[33], the air calcined sample displayed a forced closure of the hysteresis loop. This feature is referred to as cavitation and associated with ink-bottle type pores.[43] The appearance

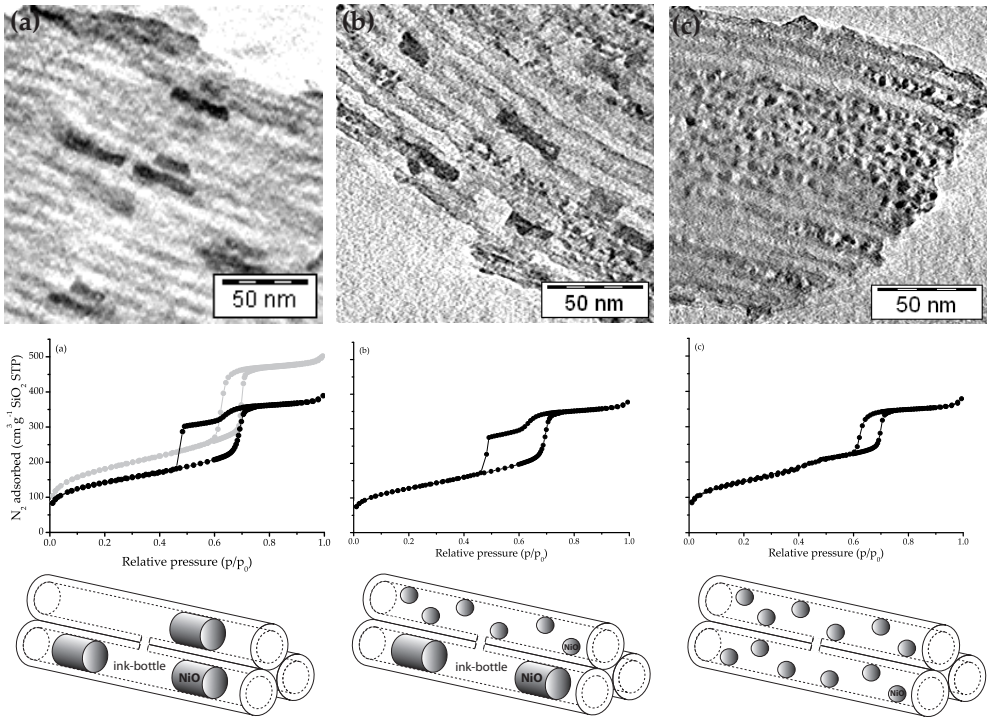


*Figure 3.* ET slices, $N_2$-physisorption isotherms and schematic representations of the NiO particle distribution inside the mesopores and of NiO/SBA-15 samples obtained after heating to 450 °C of dried impregnate S/D in air flow (a), in pure He flow (b) or in 1 vol% NO/He flow (c). Also included is the isotherm of pristine SBA-15 (a, grey).

of cavitation upon introduction of a guest phase[31,44] or plugs[45] to SBA-15 has been previously reported. Quantification (Table 2) showed that 74% of the mesopore volume ($V_{meso,bl}$) was blocked by the rodlike NiO particles. In He atmosphere (Figure 3b), similar ink-bottles were found with ET, hence cavitation was also observed in the isotherm. However, quantification showed that the total blocked mesopore volume had lowered to 57%. As schematically illustrated in Figure 3, this was in line with the observation that pores with smaller NiO particles, that allowed normal hysteresis, were present too. Finally, in NO/He (Figure 3c) the well-dispersed NiO particles were small enough (3 to 5 nm), had not agglomerated and hence the sample displayed hysteresis similar to that of pristine SBA-15. The observed trend in the mesopore volumes supported the abovementioned findings as the porosity decreased going from air to He, and to NO/He due to the more extensive retention of the NiO guest phase inside the mesopores for the latter cases. Thus, with ET analysis we could directly image the NiO distribution inside individual mesopores, and combined with $N_2$-physisorption and XRD bulk characterisation this led to a consistent insight into influence of the gas atmosphere on the obtained NiO particle distribution inside the mesopores of SBA-15.

The experiments with stagnant air and with air flow (see Figure 1) demonstrated that the concentration of gaseous decomposition products had a profound impact on the final NiO dispersion. Hence, insight into the interplay between NO and these products, and its effect on the NiO dispersion was important to better understand the role of NO. Therefore, we conducted a series of experiments in which on the one hand the NO concentration was varied while maintaining a constant flow rate

*Table 2.* $N_2$-physisorption results of SBA-15 supported samples.

| **Sample** | **Surface area ($m^2.g_{SiO2}^{-1}$)** | **Porosity ($cm^3.g_{SiO2}^{-1}$)** | | | | | |
|---|---|---|---|---|---|---|---|
| | $S_t$ [a] | $V_{tot,calc}$ [b] | $V_{tot,exp}$ [c] | $V_{micro}$ [d] | $V_{meso}$ [e] | $V_{meso,bl}$ [f] | |
| SBA-15 | 516 | 0.78 | 0.78 | 0.05 | 0.68 | 0.00 | 0% |
| S/D | 293 | 0.63 | 0.47 | 0.01 | 0.42 | 0.08 | 19% |
| S/D-C | 409 | 0.73 | 0.66 | 0.06 | 0.56 | 0.42 | 75% |
| S/D-$C_{He}$ | 442 | 0.73 | 0.59 | 0.03 | 0.51 | 0.29 | 57% |
| S/D-$C_{NO/He}$ | 493 | 0.73 | 0.59 | 0.05 | 0.49 | 0.00 | 66% |

[a]mesopore surface area determined using t-method; [b]expected total pore volume based on contribution of Ni precursor to volume decrease; [c]total pore volume based on amount $N_2$ adsorbed at $p/p_o$=0.995; [d]micropore volume calculated using NL-DFT; [e]mesopore volume calculated using NL-DFT; [f]partially blocked mesopore volume calculated from desorption branch (see experimental section for details).

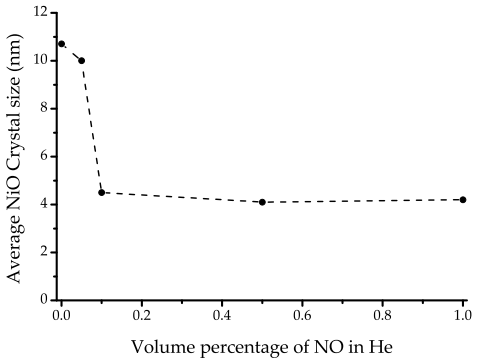


*Figure 4.* Impact of the NO concentration on the final average NiO crystal size obtained after heat treatment at 450 °C of sample G/D. A constant GHSV of 24,500 $h^{-1}$ was used.

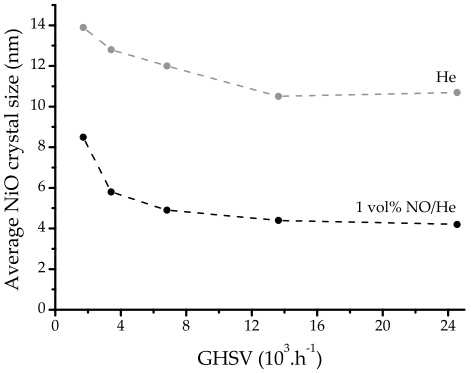


*Figure 5.* Relation between the GHSV during thermal treatment at 450 °C of sample G/D in He (grey) or in NO/He (black) and the average NiO crystal size obtained.

(i.e. constant GHSV), and on the other hand the GHSV was varied at constant NO/He concentration (1 vol%). To ensure plug-flow conditions we used a conventional silica gel powder sieve fraction instead of the low-density SBA-15. Silica gel powder with a porosity (0.90 cm3.$g^{-1}$) and an average pore size (7 nm) comparable to that of the SBA-15 was selected. Prior to the plug-flow experiments, it was checked whether the impact on the NiO dispersion found with silica gel was similar as with SBA-15. From the results collected in Table 1 it can be concluded that indeed the same trends were found. In Figure 4, the relation has been plotted between the NO/He concentration and the average NiO crystal size obtained. Without addition of NO to the He flow an average NiO crystal size of almost 11 nm was obtained. Adding a small amount of 0.05 vol% NO only had a small impact, but doubling to 0.1 vol% led to a decrease by more than a factor of two of the average crystal size. Further increase of the concentration had little effect as the average NiO crystal size of 4 nm remained constant. Thus, at the present loading of 28 wt% NiO and high GHSV of 24,500 $h^{-1}$, a concentration of 0.1 vol% NO/He was sufficient to obtain small NiO crystallites of 4 nm on average.

The results obtained when varying the GHSV between 1,700 to 24,500 $h^{-1}$ with pure He flow or NO/He flow (1 vol%) are shown in Figure 5. The results demonstrated that the obtained average NiO crystal sizes with NO/He were always smaller than with pure He. With the latter gas atmosphere, the average NiO crystal size started to increase at a GHSV lower than ~14,000 $h^{-1}$. Although decreasing the GHSV with a factor of 2 had little effect, further lowering led to more sintering and finally an average crystal size of almost 14 nm was found. Although at all times smaller NiO crystals were obtained with NO/He, the crystal sizes followed a similar trend as with pure He. Lowering of the GHSV by more than a factor of 7 from 24,500 $h^{-1}$ to 3,400 $h^{-1}$ led to a rise of the crystal size of around 4 to 6 nm. Further decrease of the

GHSV resulted in substantial rise of the average NiO crystal size to 9 nm, but still being smaller than with pure He. These results suggest the relation between the NiO crystal size and the concentration of gaseous decomposition products, and the necessity of a minimum local NO concentration to moderate the $Ni_3(NO_3)_2(OH)_4$ decomposition in such as way that small NiO particles are formed.

To identify the type of gaseous decomposition products formed, we conducted TGA/MS experiments using SBA-15 supported impregnate S/D. The results obtained with 1 vol% NO/He flow were compared with those obtained in air flow and in pure Ar flow. The TGA and MS results are shown in Figure 6 and 7, respectively. For all samples up to ~200 °C removal of physisorbed $H_2O$ and partial dehydroxylation of the $SiO_2$ surface took place. Evolved gas analysis results supported this as only mass fractions were detected that belonged to $H_2O$. Surprisingly, at 210 °C weight loss due to dehydration of the NO/He flow treated sample was almost 1.5% larger than those treated in air or in Ar flow. At higher temperatures, irrespective of the atmosphere used, the weight losses rapidly increased till a temperature of ~320 °C was reached. The observed weight losses for air (13%), Ar (13%), and NO/He (12.5%) atmosphere matched or were close to the expected value of 13% upon complete decomposition of $Ni_3(NO_3)_2(OH)_4$ into NiO. MS results showed that $H_2O$, $NO_2$ and $O_2$ gaseous products were formed as expected based on Eq. 1. The MS signal with *m*/*z*= 18 originated from $H_2O$ and was found in all atmospheres. Mass fraction 17 ($OH^+$) was found to support the assignment to $H_2O$. Mass fraction 46 confirmed that significant amounts of $NO_2$ formed during decomposition, irrespective of the atmosphere. In Ar flow we detected, albeit in relatively small amounts, *m*/*z*= 32 indicative for $O_2$. Next to these expected products also mass fraction 44 was found to evolve during each treatment, and this indicated that either $N_2O$, $CO_2$ or a mixture of these compounds was formed.

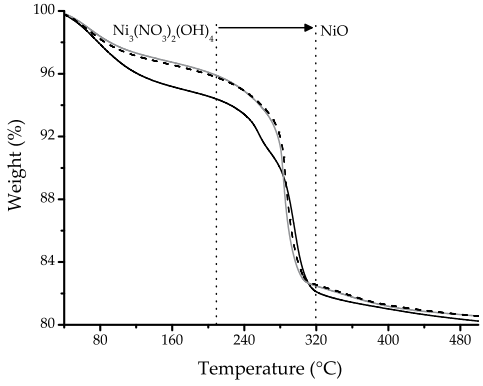


*Figure 6.* TGA curves recorded during thermal treatment of sample S/D in air flow (dashed line), in Ar flow (grey line) or in 1 vol% NO/He flow (black line).

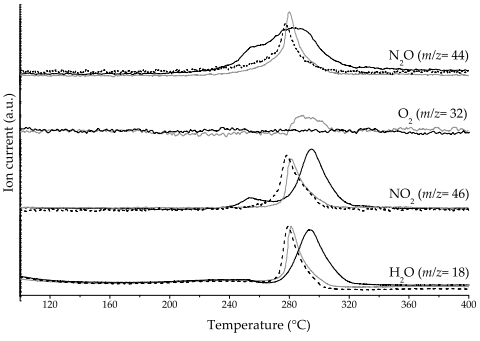


*Figure 7.* MS results obtained from the off-gas during thermal treatment of sample S/D in air flow (dashed lines), in Ar flow (grey lines) or in 1 vol% NO/He (black lines).

With GC analysis we could confirm that this mass fraction originated exclusively from $N_2O$, which is in line with observations of Małecki *et al.*[46] that 5 to 8 wt% of the nitrogen from nitrates evolves as $N_2O$. A remarkable difference was that $O_2$ was not found during decomposition in NO/He. Furthermore, in NO/He the bulk of the gasses evolved over a broader temperature range and, apart from $N_2O$, the peaks also shifted to higher temperatures. This indicated that NO influenced the kinetics of the $Ni_3(NO_3)_2(OH)_4$ decomposition, and the absence of $O_2$ during decomposition in NO/He suggested that NO might scavenge atomic oxygen that is expected to play a role in the mechanism of the decomposition of $Ni_3(NO_3)_2(OH)_4$.

As the TGA/MS results indicated that NO affected the rate of decomposition of $Ni_3(NO_3)_2(OH)_4$ into NiO, and both phases were crystalline, we carried out *in situ* XRD experiments to study the possible moderation of the reaction rate by NO in more detail. The most intense (001) and (002) diffraction lines of $Ni_3(NO_3)_2(OH)_4$ and NiO at 14.9° and 50.8° 2θ (see Figure 1) were used for this, respectively. The experiments were carried out with sample S/D and consisted of heating to 248 °C and maintaining isothermal conditions during decomposition as this could give more insight into the kinetics. The observed $Ni_3(NO_3)_2(OH)_4$ decomposition and NiO formation at 248 °C in air flow or in 1 vol% NO/He flow have been plotted in Figure 8. The left frame graph showed that after an incubation time of almost 25 minutes, decomposition proceeded relatively fast in air at a rate of about ~13%.min$^{-1}$, and about 85% of the $Ni_3(NO_3)_2(OH)_4$ decomposed within 6.5 minutes. In NO/He atmosphere, decomposition started almost immediately and though the initial rate was somewhat higher (3.6%.min-1), a relatively low constant rate of 2.7%.min$^{-1}$ throughout the entire process was observed. As a result decomposition of the $Ni_3(NO_3)_2(OH)_4$ proceeded gradually over 34 minutes and took longer than in air. Moreover, a remarkable difference between the decomposition profiles in air and NO/He was observed. The former displayed an 'autocatalytic' type of trend,

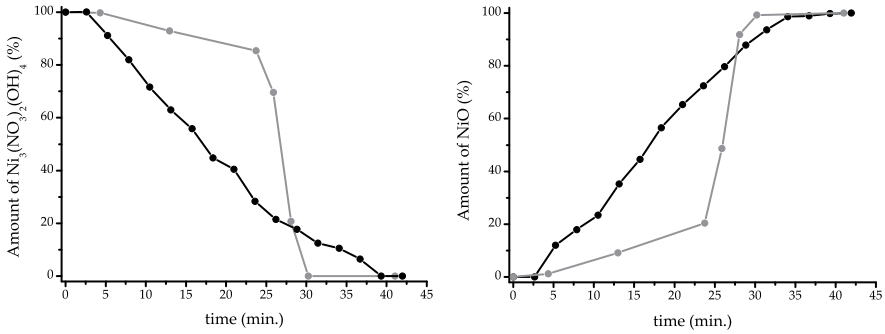


*Figure 8. in situ* XRD results obtained during thermal decomposition of $Ni_3(NO_3)_2(OH)_4$/SBA-15 sample S/D into NiO at a constant temperature of 248 °C either under air flow (grey lines) or under 1 vol% NO/He flow (black lines).

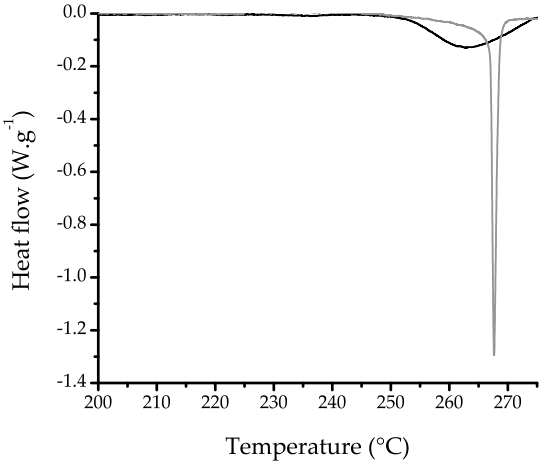


*Figure 9.* DSC heat flow traces obtained during heating at 1 °C.min$^{-1}$ ramp of SBA-15 supported $Ni_3(NO_3)_2(OH)_4$ sample S/D under air flow (grey line) or under 1 vol% NO/He flow (black line).

whereas the latter suggested zero-order kinetics. Finally, the plot on the right-hand side of Figure 8 demonstrated for both gas atmospheres that decomposition of $Ni_3(NO_3)_2(OH)_4$ was accompanied by formation of NiO without delay. In other words, the NiO formation followed an inverse profile, suggesting that no intermediate phases were formed. Similar *in situ* experiments that consisted of heating to 450 °C at a rate of 1 °C.min$^{-1}$ qualitatively supported the findings obtained at isothermal heating at 248 °C, but the decomposition rates had increased to 15.8 %.min$^{-1}$ for air and to 6.6 %.min$^{-1}$ for NO/He. Moreover, these *in situ* results showed that the average NiO crystal size observed after thermal decomposition had completed was not affected by further heating to 450 °C, and we concluded that in air precursor migration took place only during the decomposition of $Ni_3(NO_3)_2(OH)_4$ into NiO. Hence, use of an NO/He flow clearly moderated the kinetics of the $Ni_3(NO_3)_2(OH)_4$ decomposition. With the average decomposition rate we could roughly estimate the rate at which $NO_2$, $H_2O$ and oxygen evolved. Since reaction of NO with $NO_2$ or $H_2O$ was unlikely, we compared the amount of oxygen evolved with that of the 1 vol% of NO added during the reaction. Using the decomposition rate of 6.6%.min$^{-1}$, a NO : $O_2$ ratio of 32 was calculated, indicating that the amount of NO sufficed to react with all the oxygen formed during decomposition.

Thus far, the results showed on the one hand that NO moderated the decomposition rate of $Ni_3(NO_3)_2(OH)_4$, and indicated on the other hand that NO suppressed the formation of $O_2$. As both these processes would induce heat flow differences we recorded DSC traces during heat treatment of sample S/D in air flow or in 1 vol% NO/He flow. The results are given in Figure 9. Firstly, both heat flow curves showed to be endothermic, as expected, and similar to the decomposition of $Ni(NO_3)_2.6H_2O$.[47,48]

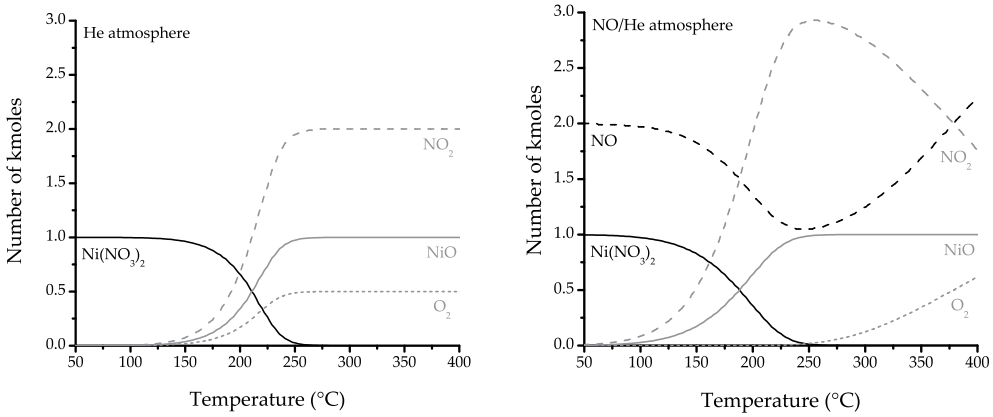


*Figure 10.* Calculated plots[49] of the temperature dependency of the thermodynamic equilibria (1 bar) of $Ni(NO_3)_2$ with NiO and gaseous $NO_2$ and $O_2$ without (left) or with NO (right). Input: 1 kmol $Ni(NO_3)_2$, 10 kmol He, 2 kmol NO (NO/He).

Secondly, the trace recorded during decomposition in air had a very sharp peak with a maximum at 268 °C, whereas the NO/He trace consisted of a broad peak from 250 to 277 °C. Hence, the DSC results confirmed that NO moderated the decomposition rate of $Ni_3(NO_3)_2(OH)_4$. In air flow a heat of reaction of +241 $J.g^{-1}$ $Ni_3(NO_3)_2(OH)_4$ was found while during NO/He treatment a heat of reaction of +202 $J.g^{-1}$ $Ni_3(NO_3)_2(OH)_4$ was observed. These differences suggested that NO played a role in lowering the heat of reaction of $Ni_3(NO_3)_2(OH)_4$ into NiO.

Although the enthalpy of formation of $Ni_3(NO_3)_2(OH)_4$ is not exactly known, an indication for the reaction enthalpies could be obtained using the heat of formation of $Ni(NO_3)_2$.[49] The endothermic decomposition of $Ni(NO_3)_2$ is usually accompanied by the formation of molecular oxygen:

$$Ni(NO_3)_2\,(s) \longrightarrow NiO\,(s) + 2NO_2\,(g) + \tfrac{1}{2}O_2\,(g) \qquad \Delta H°_r = +241\ kJ.mol^{-1} \qquad (2)$$

Although the exact mechanism of this reaction (2) is not known to us, we propose that the formation of $O_2$ is the rate determining step. In fact $O_2$ has to be formed from two oxygen radicals emerging from two nitrate groups. The combination of two radicals to form $O_2$ is most likely a surface catalysed process and NiO amongst other transition metal oxides such as $MnO_2$, $Fe_2O_3$ and CuO have been reported[50-53] to display relatively high activities in this reaction:

$$2\,O \longrightarrow O_2\,(g) \qquad (3)$$

If NiO indeed catalysed reaction (3) it would explain the 'autocatalytic' type of behaviour of the decomposition in air (Figure 8). The role of NO can now be

understood as follows. First, the overall reaction in the presence of NO excludes formation of $O_2$ (cf. Figure 7) and reads as follows:

$$Ni(NO_3)_2\,(s) + NO \longrightarrow NiO\,(s) + 3NO_2\,(g) \qquad \Delta H^\circ_r = +184\ kJ.mol^{-1} \qquad (4)$$

The lowering of the $\Delta H^\circ_r$ from +241 to +184 kJ.mol$^{-1}$ is in line with the DSC results. Second, NO affects the equilibria of reactions (2) and (4). In Figure 10, the temperature dependency of the thermodynamic equilibria of Eq. 2 (left) and 4 (right) have been plotted. The plots add to the proposed explanation of the impact that NO might have on the decomposition of $Ni_3(NO_3)_2(OH)_4$. With NO present, decomposition of $Ni(NO_3)_2$ becomes already thermodynamically feasible around 100 °C compared to ~125 °C without NO. Hence, this might explain the DSC findings (Figure 9) that the decomposition in NO started earlier than decomposition in air. Moreover, the NO/He graph shows that formation of $O_2$ during decomposition was only thermodynamically favourable if NO was not present, which was in line with the MS results obtained for thermal decomposition of $Ni_3(NO_3)_2(OH)_4$ in NO/He and Ar (Figure 7).

Finally, although somewhat less efficient, $H_2$ (see chapter 3) had shown to moderate the decomposition rate of $Ni_3(NO_3)_2(OH)_4$ too. Therefore, we propose that the presence of oxygen scavenging compounds such as NO, $N_2O$, CO and $H_2$ is crucial for preventing sintering and redistribution during thermal decomposition of supported transition metal (e.g. Fe, Co, Ni and Cu) nitrates.

## Conclusions

We studied the impact of air, He and NO/He gas atmospheres on the thermal decomposition of supported $Ni_3(NO_3)_2(OH)_4$. By combining ET, $N_2$-physisorption and XRD a consistent picture of the distribution and sizes of NiO particles inside the mesopores of SBA-15 as a function of the gas atmosphere was obtained. ET results confirmed that after treatment in air exclusively rodlike NiO particles (9×35 nm) confined by the pore walls were present inside the mesopores. During heat treatment in pure He predominantly rodlike NiO particles were formed inside the mesopores as well, but also pores were identified that contained smaller and more spherical particles.

Experiments with conventional silica gel showed that at all GHSV smaller crystals could be obtained with NO, and with a GHSV of 24,500 h$^{-1}$, 0.1 vol% NO/He was already sufficient to obtain small 4 nm NiO particles at a loading of 28 wt%.

TGA/MS results showed that the $NO_2$, $N_2O$ and $H_2O$ gaseous decomposition products evolved more gradually in NO/He than in air or in pure He, and *in situ* XRD and DSC experiments confirmed that NO moderated the decomposition rate of $Ni_3(NO_3)_2(OH)_4$ into NiO, and proceeded much slower than in air. The heat of reactions as determined with DSC suggested that decomposition in NO/He was less

endothermic than in air. This might be explained by the exothermic scavenging of oxygen radicals by NO. MS results appeared to support this hypothesis as no $O_2$ was detected amongst the gaseous decomposition products in NO/He flow contrary to treatment in pure Ar flow.

**Acknowledgements**

Rudolf Mollema, Els Verdonck and Daniel Roedolf from TA Instruments and, Herre Talsma and Mies van Steenbergen from the department of pharmaceutics are kindly thanked for their help with DSC analysis. Heiner Friedrich is acknowledged for electron tomography characterisation. Fred Broersma and Marjan Versluijs-Helder are thanked for carrying out the TGA/MS and *in situ* XRD experiments.

**References**

1. Bell, A.T. *Science* **2003**, *299*, 1688-1691.
2. Schögl, R.; Abd Hamid, S.B. *Angew. Chem. Int. Ed.* **2004**, *43*, 1628-1637.
3. Ying, J.Y. *Chem.Eng. Sci.* **2006**, *61*, 1540-1548.
4. Serp, P.; Kalck, P.; Feurer, R. *Chem. Rev.* **2002**, *102*, 3085-3128.
5. Schreier, M.; Regalbuto, J.R. *J. Catal.* **2004**, *225*, 190-202.
6. Carrier, X.; Lambert, J.F.; Che, M. *J. Am. Chem. Soc.* **1997**, *119*, 10137-10146.
7. Hermans, L.A.M.; Geus, J.W. *Stud. Surf. Sci. Catal.* **1979**, *3*, 113-130.
8. Van der Lee, M.K.; Van Dillen, A.J.; Bitter, J.H.; De Jong, K.P. *J. Am. Chem. Soc.* **2005**, *127*, 13573-13582.
9. Che, M.; Cheng, Z.X.; Louis, C. *J. Am. Chem. Soc.* **1995**, *117*, 2008-2018.
10. Bourikas, K.; Kordulis, C.; Lycourghiotis, A. *Catal. Rev.* **2006**, *48*, 363-444.
11. Van Dillen, A.J.; Terörde, R.J.A.M.; Lensveld, D.J.; Geus, J.W.; De Jong, K.P. *J. Catal.* **2003**, *216*, 257-264.
12. Clause, O.; Kermarec, M.; Bonnevoit, L.; Villain, F.; Che, M. *J. Am. Chem. Soc.* **1992**, *114*, 4709-4717.
13. Carriat, J.Y.; Che, M.; Kermarec, M.; Verdaguer, M.; Michalowicz, A. *J. Am. Chem. Soc.* **1998**, *120*, 2059-2070.
14. Lekhal, A.; Glasser, B.J.; Khinast, J.G. *Chem. Eng. Sci.* **2004**, *59*, 1063-1077.
15. Kotter, M.; Riekert, L. *Stud. Surf. Sci. Catal.* **1979**, *2*, 53-63.
16. Lensveld, D.J.; Mesu, J.G.; Van Dillen, A.J.; De Jong, K.P. *Micropor. Mesopor. Mater.* **2001**, *44-45*, 401-407.
17. Fang, K.; Ren, J.; Sun, Y. *Mol. Catal. A: Chem.* **2005**, *229*, 51-58.
18. Van den Brink, P.J.; Scholten, A.; Van Wageningen, A.; Lamers, M.D.A.; Van Dillen, A.J.; Geus, J.W. *Stud. Surf. Sci. Catal.* **1991**, *63*, 527-537.
19. Vos, B.; Poels, E.K.; Bliek, A. *J. Catal.* **2001**, *198*, 77-88.

20 Poels, E.K.; Dekker, J.G.; Van Leeuwen, W.A. *Stud. Surf. Sci. Catal.* **1991**, *63*, 205-214.
21. Van de Loosdrecht, J.; Barradas, S.; Caricato, E.A.; Ngwenya, N.G.; Nkwanyana, P.S.; Rawat, M.A.S.; Sigwebela, B.H.; Van Berge, P.J.; Visagie, J.L. *Top. Catal.* **2003**, *26*, 121-127.
22. Chen, I.; Lin, S-Y.; Shiue, D-W. *Ind. Eng. Chem. Res.* **1988**, *27*, 926-929.
23. Chen, H-C.; Anderson, R.B. *J. Catal.* **1976**, *43*, 200-206.
24. Balakos, M. W.; Hernandez, E.E. *Catal. Today* **1997**, *35*, 415-425.
25. Fouilloux, P. *Appl. Catal.* **1983**, *8*, 1-42.
26. Allen, R.R. *J. Am. Oil Chem. Soc.* **1986**, *63*, 1328-1332.
27. Sietsma, J.R.A.; De Jongh, P.E.; Van Dillen, A.J.; De Jong, K.P. *Stud. Surf. Sci. Catal.* **2006**, *162*, 95-102.
28. Sietsma, J.R.A.; Van Dillen, A.J.; De Jongh, P.E.; De Jong, K.P. *Patent application* No. WO2007/071899 **2007**.
29. Sietsma, J.R.A.; Meeldijk, J.D.; Den Breejen, J.P.; Versluijs-Helder, M.; Van Dillen, A.J.; De Jongh, P.E.; De Jong, K.P. *Angew. Chem. Int. Ed.* **2007**, *46*, 4547-4549.
30. Koster, A. J.; Ziese, U.; Verkleij, A. J.; Janssen, A. H.; De Jong, K. P. *J. Phys. Chem. B.* **2000**, *104*, 9368-9370.
31. Janssen, A.H.; Yang, C.-M.;Wang, Y.; Schüth, F.; Koster, A.J.; De Jong, K.P. *J. Phys. Chem B* **2003**, *107*, 10552-10556.
32. Ziese, U.; De Jong, K.P.; Koster, A.J. *Appl. Catal. A: General* **2004**, *260*, 71.
33. Zhao, D.; Feng, J.; Huo, Q.; Melosh, N.; Fredrickson, G.H.; Chmelka, B.F.; Stucky, G.D. *Science* **1998**, *279*, 548-552.
34. Kremer, J. R.; Mastronarde, D. N.; McIntosh, J. R. *J. Struct. Biol.* **1996**, *116*, 71-76.
35. Jaroniec, M.; Kruk, M.; Olivier, J.P.; Koch, S. *Stud. Surf. Sci. Catal.* **2000**, *128*, 71-80.
36. Barrett, E.P.; Joyner, L.S.; Halenda, P.P. *J. Am. Chem. Soc.* **1951**, *73*, 373-380.
37. Harkins, W.D.; Jura, G. *J. Am. Chem. Soc.* **1944**, *66*, 1366-1373.
38. Kruk, M.; Jaroniec, M.; Sayari, A. *Langmuir* **1997**, *13*, 6267-6273.
39. Lippens, B.C.; De Boer, J.H. *J. Catal.* **1965**, *4*, 319-323.
40. Gallezot, P.; Prettre, M. *Bull. Soc. Chim. Fr.* **1969**, *2*, 407-.
41. Estellé, J.; Salagre, P.; Cesteros, Y.; Serra, M.; Medina, F.; Sueiras, J.E. *Solid State Ionics* **2003**, *156*, 233-243.
42. Friedrich, H.; Sietsma, J.R.A.; De Jongh, P.E.; De Jong, K.P. *J. Am. Chem. Soc.* **2007**, *129*, 10249-10254.
43. Ravikovitch, P.I.; Neimark, A.V. *Langmuir* **2002**, *18*, 9830-9837.
44. Vradman, L.; Landau, M.V.; Kantorovich, D.; Koltypin, Y.; Gedanken, A. *Micropor. Mesopor. Mater.* **2005**, *79*, 307-318.
45. Van Der Voort, P.; Ravikovitch, P. I.; De Jong, K. P.; Benjelloun, M.; Van Bavel, E.; Janssen, A. H.; Neimark, A. V.; Weckhuysen, B. M.; Vansant, E. F. *J. Phys. Chem. B.* **2006**, *106*, 5873-5877.

46. Małecki, A.; Małecki, B. *Thermochim. Acta* **2006**, *446*, 113-116.
47. Maneva, M.; Petroff, N.; Pankova, M. *J. Therm. Anal.* **1990**, *36*, 577-587.
48. Hou, X.; Williams, J.; Choy, K-L. *Thin Solid Films* **2006**, *495*, 262-265.
49. *HSC Chemistry for Windows 4.1:* Roine, A., Outokumpu Research Oy, Pori, Finland.
50. Bhattacharya, A.K. *J. Chem. Soc., Faraday Trans. 1* **1978**, *74*, 1750-1757.
51. Greaves, J.C.; Linnett, J.W. *Trans. Faraday Soc.* **1959**, *55*, 1346-1354.
52. Dickens, P.G.; Sutcliffe, M.B. *Trans. Faraday Soc.* **1964**, *60*, 1272-1285.
53. Crane, P.J.; Dickens, P.G.; Thomas, R.E. *Trans. Faraday Soc.* **1967**, *63*, 693-700.

# 6

# Highly active Fischer-Tropsch catalysts obtained from NO controlled thermal decomposition of cobalt nitrate precursor

The preparation of $Co/SiO_2$ Fischer-Tropsch catalysts by the impregnation and drying method using aqueous $[Co(OH_2)_6](NO_3)_2$ precursor solutions was studied. After impregnation and drying the nitrate precursor appeared well-dispersed, however, severe sintering and redistribution during the air calcination step led to poorly dispersed $Co_3O_4$ particles (8 to 60 nm). It was identified that thermal treatment in NO/He prevented sintering and redistribution, yielding silica gel supported $Co_3O_4$ particles of 3 to 5 nm at a Co metal loading of 18 wt%. Due to the small particles, reduction to Co metal was more difficult than with the air calcined samples. As a result, the activity of the NO/He treated catalysts largely depended on the reduction temperature used. The highest activity of $5.4\times10^{-5}$ $mol_{CO}.g_{Co}^{-1}.s^{-1}$ was obtained after reduction at 550 °C, but addition of 0.05 wt% Pt reduction promoter to the catalyst allowed lowering of the temperature to 450 °C without loss of activity. Preparation of catalysts involving the NO/He heat treatment led to an increase in activity by more than a factor of two compared to the catalysts treated through conventional calcination in air or direct treatment with $H_2$.

## Introduction

Fischer-Tropsch (FT) synthesis is an important process for the production of clean liquid fuels from synthesis gas, a mixture of $H_2$ and CO.[1-3] Presently, the process receives wide-spread interest as it allows profitable use of the large world-wide natural gas and coal reserves.[4] Although the FT synthesis is also catalysed by ruthenium, only iron and cobalt are commercially applied. Despite iron being more cost-effective, cobalt is generally preferred in natural gas based FT because of its superior activity, selectivity and stability.[5] Currently, a typical industrial catalyst contains relatively large cobalt metal particles of 10 to 20 nm in size. From an economical point of view it is important that the effectiveness of the cobalt metal is increased. An optimal cobalt metal particle size of 6-8 nm for carbon nanofibers supported catalysts has been reported recently.[6] Next to the cobalt dispersion, the support has been varied with emphasis on silica[7], alumina[8] and titania[9]. In particular with silica many fundamental studies on preparation[7], cobalt dispersion[10] and reducibility[11] have been carried out. Although addition of small amounts of elements such as Zr and Mn generally improves the performance of the catalyst by increasing the selectivity[12,13], obtaining highly active catalysts remains desirable. In this chapter we focus on the preparation of highly active $Co/SiO_2$ catalysts.

The most widely used method for the preparation of heterogeneous catalysts is deposition of the active component onto a support by impregnation with a precursor-containing solution. Subsequently, the catalyst precursor is dried and further treated through heat treatments such as air calcination and high-temperature reduction with $H_2$ to bring about the desired cobalt metal particles. This method is primarily attractive because of its simplicity, low costs and limited amount of waste produced. The type of metal salt used has a large impact on the final size of the metal particles. With organic precursor complexes (e.g. acetates and citrates) typically small metal particles of 1 to 3 nm can be deposited, but due to their limited solubility only moderate cobalt metal loadings up to 10 wt% can be achieved via single-step impregnations.[14] Moreover, high reduction temperatures are often needed due to relatively strong precursor-support interactions.[7] When higher loadings are required, inorganic salts are typically used because of their high solubility. In particular use of $Co(NO_3)_2.6H_2O$ is attractive as pure $Co_3O_4$ can be obtained through thermal decomposition of the nitrate. Unfortunately, its use as precursor salt often yields catalysts that display a poor cobalt metal dispersion. A number of attempts have been reported to address this problem. Van der Loosdrecht *et. al*.[8] reported that increasing the air-space-velocity during the calcination treatment of the dried impregnate led, after high temperature reduction, to a higher FT activity as the cobalt metal dispersion increased. Soled and co-workers observed that heat treating the dried impregnate directly with $H_2$ improved the performance too.[15] The latter treatment is often referred to as the 'direct reduction' method.

Herein, we present a novel method for the preparation of highly-active silica supported FT catalysts based on the impregnation and drying method using

aqueous $[Co(OH_2)_6](NO_3)_2$ precursor solutions. The method comprises of controlling the thermal decomposition of the nitrate precursor into $Co_3O_4$ in the presence of NO, followed by high-temperature reduction in $H_2$ to end up with the metal catalyst. The impact of NO on the $Co_3O_4$ particle size is compared to that of air using results obtained with ordered mesoporous silica SBA-15, but conventional silica gel catalysts are used for catalytic testing. Moreover, the activity of the catalysts prepared via thermal treatment in NO/He flow are compared with those obtained via standard air calcination and those obtained via the direct treatment in $H_2$.

## Experimental

*Sample preparation*

SBA-15 (pore volume= 0.80 ml.g$^{-1}$ and pore size= 9 nm) was synthesised according to the procedure of Zhao *et al.*[16]. 8 g of $PEO_{20}PPO_{70}PEO_{20}$ (PEO= poly(ethylene oxide) and PPO= poly(propylene oxide)) tri-block copolymer (Aldrich) was dissolved in 250 ml demineralised water of 40 °C. After the solution had become clear, 48 g of concentrated HCl (Merck) was added, followed by the addition of 21.5 ml of tetraethyl orthosilicate (Acros). The mixture was stirred for 20 hours at 40 °C and then transferred to an oven for further reaction at 80 °C for 48 hours. The solid product was collected from the suspension by filtration, washed, dried in air for 12 hours at 80 °C and calcined for 6 hours at 550 °C. Davicat 1404SI silica gel (pore volume=0.90 ml.g$^{-1}$ and average pore diameter= 7 nm) was used as received from Grace-Davison.

Prior to impregnation, the supports were dried for 2 hours at 80 °C in dynamic vacuum. The precursor solution of 3 M was prepared by dissolving $Co(NO_3)_2.6H_2O$ (Acros) in demineralised water. Quantities of 0.25 g of SBA-15 and 1 g of silica gel were impregnated to incipient wetness with 1.00 ml.g$^{-1}$ and 1.25 ml.g$^{-1}$ of precursor solution to provide 15 wt% and 18 wt% Co metal, respectively. The samples were dried in static air during 12 hours at 70 °C using a ramp of 1 °C.min$^{-1}$. The dried silica gel and SBA-15 samples were labelled G/D and S/D, respectively. The Pt promoted catalyst was prepared by co-impregnation of the silica gel support with 1.23 ml.g$^{-1}$ of aqueous solution (demineralised water) containing 3 M of $[Co(OH_2)_6](NO_3)_2$ and 2.25 mM of $Pt(NH_3)_4(NO_3)_2$ to yield 18/0.05 wt% Co/Pt metal. The impregnate was dried in static air at 60 °C (ramp= 1 °C.min$^{-1}$) for 4 hours and labelled G/DPt.

The reduction/oxidation treatments of samples G/D-NC-R-ox and G/D-$H_2$-ox were carried out using 100 mg of G/D-NC and G/D, respectively. After reduction for 2 hours at 550 °C (ramp= 5 °C.min$^{-1}$) in 120 ml.min$^{-1}$ flow of 33 vol% $H_2/N_2$ flow, the sample was cooled down with 10 °C.min$^{-1}$ to 300 °C under a flow of 80 ml.min$^{-1}$ $N_2$, flushed for 10 minutes with 1.25 vol% $O_2/N_2$ (81 ml.min$^{-1}$), and heated with 5 °C.min$^{-1}$ to 400 °C under a 20 vol% $O_2/N_2$ flow of 100 ml.min$^{-1}$. The sample was kept at 400 °C for 1 hour and subsequently cooled to room temperature while maintaining the 100 ml.min$^{-1}$ flow of 20 vol% $O_2/N_2$.

Quantities of 40 to 100 mg of the dried impregnates were heated in air or in 1 vol% NO/He flow (90 ml.min$^{-1}$) to 450 °C with a ramp of 1 °C.min$^{-1}$. The final temperature of 450 °C was maintained for 4 hours, and the obtained products treated in air were labelled with AC, whereas the 1 vol% NO/He treated ones were denoted with NC. The direct treatment of dried impregnate G/D (20 mg) prior to catalysis was done *in situ* using a 33 vol% $H_2$/He flow (60 ml.min$^{-1}$) and heating rate of 5 °C.min$^{-1}$. The products were labelled G/D-$H_2$.

*Characterisation*

Powder X-ray Diffraction (XRD) patterns were obtained from 35 to 80° 2θ with a Bruker-AXS D8 Advance X-ray Diffractometer setup using Co-$K_{\alpha 12}$ radiation.

$N_2$-physisorption measurements were performed on a Micromeritics Tristar 3000 apparatus at -196 °C. Prior to analysis the samples were dried in a He flow at 120 °C for 14 hours. The pore size distribution, micro- and meso-porosity were derived from the adsorption branch of the isotherm using NL-DFT. A model developed by Jaroniec *et al.*[17] for ordered mesoporous silica supports with cylindrical pore geometry was used. There is no standard method for the determination of blocked mesopore volume ($V_{meso,bl}$). We used the BJH theory[18] with the Harkins and Jura[19] thickness equation and the Kruk-Jaroniec-Sayari[20] correction for ordered mesoporous siliceous materials to calculate from the desorption branch the cumulative pore volume distribution. The total amount of $V_{meso,bl}$ was determined considering that the volume in pores with a diameter of 2 - 5 nm is (partially) blocked. Mesopore and external surface areas were determined with the t-method[21] using thickness ranges of 0.35 - 0.55 and 1.00 - 1.41 nm, respectively.

Scanning Transmission Electron Microscopy (STEM) images were obtained using a Tecnai 20 FEG microscope operating at 200 kV.

*Catalysis*

Fischer-Tropsch synthesis was done at 1 bar and 220 °C using a plug-flow reactor and $H_2$/CO volume ratio of 2. To achieve isothermal plug-flow conditions a small quantity of the sample (20 mg) was mixed with 200 mg SiC particles with a diameter of 0.2 mm. The calcined catalysts were in situ reduced using He containing 33 vol% of $H_2$ and a total flow of 60 ml.min$^{-1}$. Reduction temperatures were varied from 350 °C to 600 °C and a heating rate of 5 °C.min$^{-1}$ was used. The final reduction temperature was maintained for two hours. Online product gas analysis ($C_1$-$C_{20}$) was performed using a gas chromatograph to determine the selectivity (wt%) towards $C_1$ and $C_{5+}$ hydrocarbons. The activities and selectivities were determined after 16 - 22 hours of reaction. For this the conversion of CO was adjusted to 2% by tuning the flows.

## Results and discussion

*Ordered mesoporous SBA-15 supported $Co_3O_4$ catalysts*

The preparation of $Co_3O_4/SiO_2$ catalysts by impregnation with an aqueous $[Co(OH_2)_6](NO_3)_2$ solution, followed by drying and subsequent heat treatments was studied using ordered mesoporous silica SBA-15 as model support. Because of its ordered structure, STEM analysis of the SBA-15 supported samples yielded detailed information of the impact of each step in the preparation on the precursor dispersion and distribution over the support.

STEM results of sample S/D obtained after impregnation, and drying at 70 °C indicated that the Co precursor was well-dispersed over the support as no large particles or agglomerates were found outside the mesopores of SBA-15. An overview of the STEM and XRD characterisation results of the samples is given in Table 1. The purple colour of the sample suggested that $Co(NO_3)_2.6H_2O$ had formed as a consequence of the drying treatment, however, this could not be confirmed with XRD as no crystalline phase was detected. With low-angle XRD measurements retention of the long range order of the support upon impregnation and drying was confirmed as the (100), (110), (200), (210) and (300) diffraction lines of the hexagonal unit cell of SBA-15[16] were still found. The SBA-15 supported samples were characterised with $N_2$-physisorption, and the results have been summarised in Table 2. The physisorption results were corrected for the contribution of precursor to the

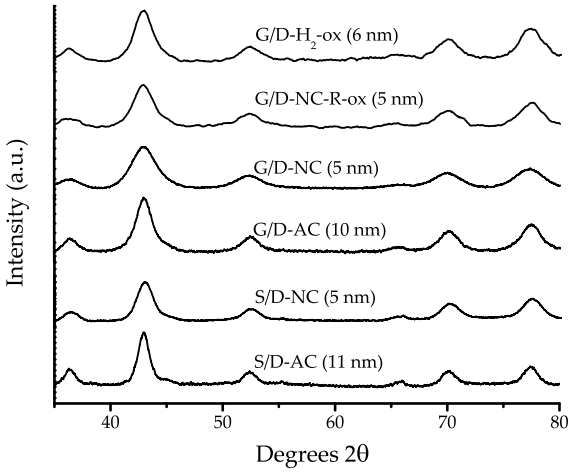


*Figure 1.* XRD patterns of SBA-15 and silica gel supported $Co_3O_4$ obtained after calcination in air flow (AC) or after heat treatment in 1 vol% NO/He flow (NC). Also included are the patterns obtained for silica gel samples G/D and G/D-NC that were reduced with $H_2$ and re-oxidised at 400 °C to form $Co_3O_4$.

*Table 1.* Overview of thermal treatments and, XRD and STEM results.

| Samples | Thermal treatments | Precursor phase | Loading (wt%) | Size (nm) | |
|---|---|---|---|---|---|
| | | | | $d_{XRD}$ | $d_{TEM}$ |
| **SBA-15** | | | | | |
| S/D | drying | amorphous | 47[a] | - | - |
| S/D-AC | drying / calcination in air | $Co_3O_4$ | 19 | 10 | 10-100[b] |
| S/D-NC | drying / heating in 1 vol% NO/He | $Co_3O_4$ | 19 | 5 | 3-5 |
| **Silica gel** | | | | | |
| G/D | drying | amorphous | 52[a] | - | - |
| G/D-AC | drying / calcination in air | $Co_3O_4$ | 23 | 11 | 8-60 |
| G/D-NC | drying / heating in 1 vol% NO/He | $Co_3O_4$ | 23 | 5 | 3-5 |
| G/D-NC-R550-ox | drying/heating in 1 vol% NO/He / reduction at 550 °C in 33 vol% $H_2$ / oxidation at 400 °C | $Co_3O_4$ | 23 | 5 | - |
| G/D-$H_2$-ox | drying/heating in 33 vol% $H_2$/He / reduction at 550 °C in 33 vol% $H_2$ / oxidation at 400 °C | $Co_3O_4$ | 23 | 6 | - |
| GPt/D-NC | drying/heating in 1 vol% NO/He | $Pt/Co_3O_4$ | 0.05/23 | 6 | - |

[a]assuming a $Co(NO_3)_2.6H_2O$ phase; [b]primarily rodlike particles inside the mesopores.

*Table 2.* $N_2$-physisorption results of SBA-15 supported samples.

| Sample | Surface area ($m^2.g_{SiO2}^{-1}$) | | Porosity ($cm^3.g_{SiO2}^{-1}$) | | | | | |
|---|---|---|---|---|---|---|---|---|
| | $S_t$[a] | $S_{t,ext}$ | $V_{tot,calc}$[b] | $V_{tot,exp}$[c] | $V_{micro}$[d] | $V_{meso}$[e] | $V_{meso,bl}$[f] | |
| SBA-15 | 516 | 38 | 0.78 | 0.78 | 0.05 | 0.68 | 0.00 | 0% |
| S/D | 231 | 27 | 0.53[h] | 0.50 | 0.01 | 0.46 | 0.00 | 0% |
| S/D-AC | 400 | 33 | 0.74 | 0.56 | 0.02 | 0.50 | 0.41 | 82% |
| S/D-NC | 330 | 27 | 0.74 | 0.47 | 0.04 | 0.40 | 0.00 | 0% |

[a]mesopore surface area determined using t-method; bexternal surface area calculated using t-method; [c]expected total pore volume based on contribution of Co precursor to volume decrease; [d]total pore volume based on the amount of $N_2$ adsorbed at $p/p_o$=0.995; [e]micropore volume calculated using NL-DFT; [f]mesopore volume calculated using NL-DFT; [g]partially blocked mesopore volume calculated from desorption branch (see experimental section for details); [h]assuming a $Co(NO_3)_2.6H_2O$ phase.

total weight of the sample and expressed per gram of $SiO_2$. $N_2$-physisorption results of the dried impregnate S/D showed that the total pore volume had decreased to 0.50 $cm^3.g_{SiO2}^{-1}$, which was close to the expected decrease to 0.53 $cm^3.g^{-1}$ and supported the STEM findings that cobalt nitrate precursor was present inside the mesopores of SBA-15. Subsequently the dried impregnate was calcined in an air flow at 450 °C to yield greyish sample S/D-AC. The XRD pattern obtained for this sample is shown in Figure 1. Line-broadening analysis (Table 1) indicated that $Co_3O_4$ had formed with an average crystal size of 10 nm. Typical STEM image of sample S/D-AC are shown in the top frame of Figure 2. The majority of $Co_3O_4$ particles were found inside the mesopores, but exclusively with a rodlike symmetry due to confinement by the pore walls. The size of these rodlike particles varied from about 10 to 100 nm. Moreover, the rodlike particles in adjacent pores appeared agglomerated as $Co_3O_4$ was concentrated in specific patches within the SBA-15 particles.

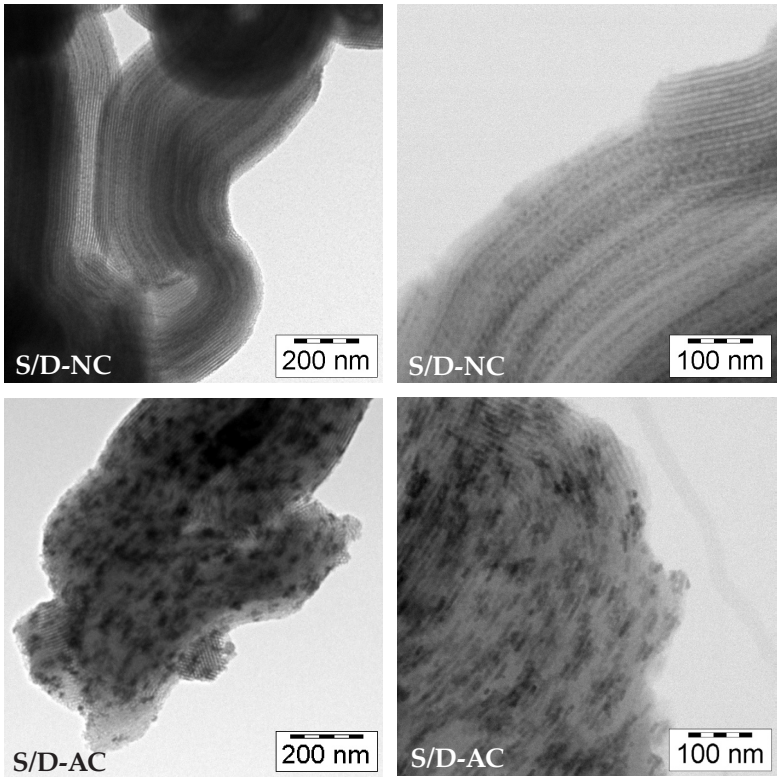


*Figure 2.* STEM images of samples S/D-AC and S/D-NC obtained through heat treatment at 450 °C of dried impregnate S/D in air (bottom) or in 1 vol% NO/He (top), respectively.

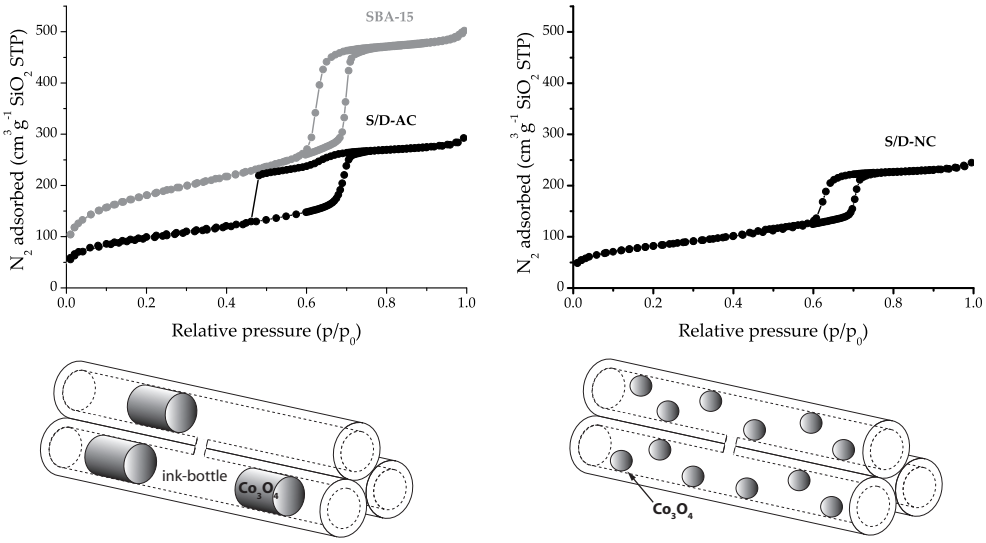


*Figure 3.* $N_2$-physisorption isotherms of pristine SBA-15, and samples S/D-AC and S/D-NC obtained after heat treatment of sample S/D in air flow or in 1 vol% NO/He flow. Also included are schematic representations of the impact of the thermal treatment in air (left) and in NO/He (right) on the $Co_3O_4$ distribution inside the mesopores.

In Figure 3 the $N_2$-physisorption isotherm is depicted together with that of pristine SBA-15 (grey). The isotherm of the pristine SBA-15 contained all features typical for this material: a high onset at low relative pressures because of the intra-wall micro porosity, and hysteresis at higher values ($p/p_o$= 0.69 to 0.71) originating from the uniform mesoporous channels with a diameter of 9 nm. The adsorption branch of the air calcined product S/D-AC contained similar features as observed for pristine SBA-15, whereas during desorption a delayed closure of the hysteresis loop was found in the relative pressure region of 0.45 to 0.50. This forced closure of the desorption branch at ~0.48 is typical for emptying of ink-bottle pores with necks smaller than 3 to 4 nm and referred to as cavitation.[22-25] In sample S/D-AC, these pores were created by voids between the rodlike $Co_3O_4$ particles inside the mesopores as has been illustrated in Figure 3. This partially blocked mesopore volume ($V_{meso,bl}$) was found to be 82% of the total accessible mesoporosity. Compared with the dried impregnate, the total pore volume had increased to 0.56 $cm^3.g_{SiO2}^{-1}$ as the density increased by going from the nitrate to $Co_3O_4$. However, the porosity was lower than expected (0.74 $cm^3.g_{SiO2}^{-1}$) supposedly due to inaccessible domains formed by the $Co_3O_4$ guest phase.

Next, the dried impregnate S/D was heat treated at 450 °C in a 1 vol% NO/He flow. The product was labelled S/D-NC, and XRD analysis (Figure 1) showed that

the sample contained $Co_3O_4$ crystals with an average size of 5 nm instead of 10 nm as obtained after air calcination. In the bottom frame of Figure 2, STEM images of the sample are given. The images showed that the heat treatment had led to the formation of well-dispersed $Co_3O_4$ particles and sizes of about 3 to 5 nm were found. Neither rodlike $Co_3O_4$ particles inside the mesopores, nor $Co_3O_4$ particles were found outside the mesopores. The $N_2$-physisorption isotherm obtained for this sample is shown in Figure 3. The isotherm contained similar features as observed with the air calcined sample, however, no cavitation was observed due to the exclusive formation of $Co_3O_4$ particles small enough to allow normal emptying of the mesopores as illustrated in Figure 3. Moreover, the mesopore volume (Table 2) had lowered with respect to the air calcined sample due to more extensive retention of $Co_3O_4$ inside the mesopores. Hence, sintering and redistribution was prevented by heat treating the dried impregnate in 1 vol% NO/He flow instead of in air flow allowing preparation of small $Co_3O_4$ particles at a loading of 19 wt%.

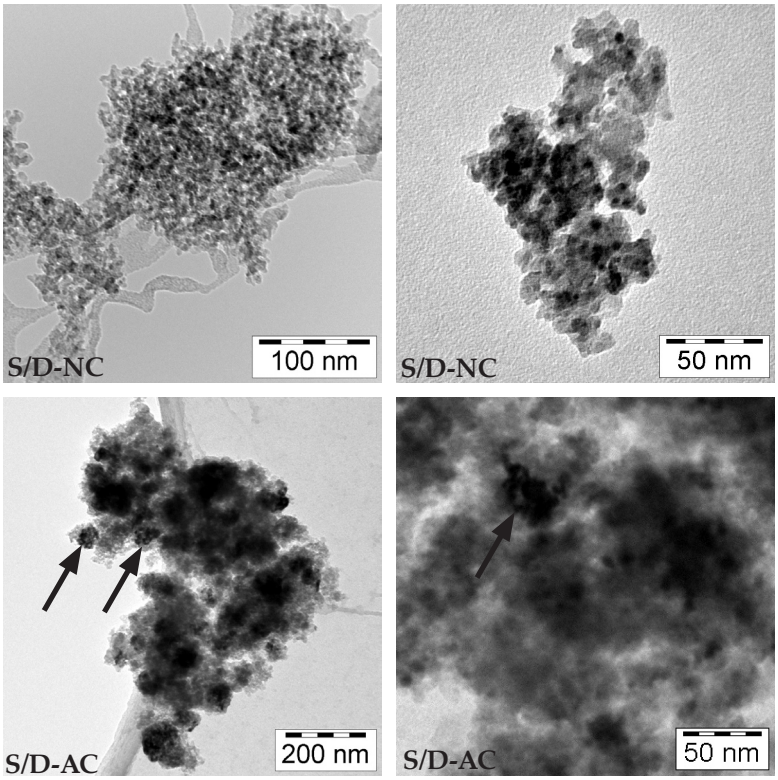


*Figure 4.* TEM images of silica gel supported $Co_3O_4$ obtained through calcination in air (bottom) or heat treatment in 1 vol% NO/He (top). The arrows indicate regions that indicate clusters of $Co_3O_4$ particles.

Similar experiments were carried with silica gel. The XRD patterns of G/D-AC (air calcined) and G/D-NC (NO/He heat treated) shown in Figure 1 indicated that similar results were obtained as the average $Co_3O_4$ crystal size had decreased from 11 nm (air) to 5 nm (NO/He). TEM images of the air calcined and NO/He treated samples are given in Figure 4. The TEM results (Table 1) supported the XRD findings as with NO/He well-dispersed $Co_3O_4$ particles of about 3 to 5 nm were found contrary to the air calcined sample that contained particles ranging from 8 to 60 nm.

To conclude, thermal decomposition of the nitrate precursor in a flow of 1 vol% NO/He enabled preparation of silica supported catalysts that contained small $Co_3O_4$ particles at loadings of 19 wt% (SBA-15) or 23 wt% (silica gel).

*Fischer-Tropsch synthesis over Co/$SiO_2$ catalysts*

As the silica gel supported $Co_3O_4$ catalyst precursors prepared through the NO/He method showed promising properties for catalysis (i.e. high dispersion at high loadings) we tested their catalytic performance after high-temperature reduction in the Fischer-Tropsch synthesis of hydrocarbons from synthesis gas (220 °C, 1 bar and $H_2$/CO= 2). To relate the impact of the NO/He treatment to other reported heat treatment methods to improve the dispersion, we compared the activity of the NO/He catalysts with those prepared via calcination in air using a high air-space-velocity[8] (samples G/D-AC) or direct heating in a flow of $H_2$[15] (samples G/D-$H_2$). The activity and selectivity results obtained for the catalysts are given in Figure 5 and Figure 6, respectively. In Figure 5, the activity results have been plotted as a function of the reduction temperature used after thermal decomposition of the nitrate precursor into $Co_3O_4$. The activity was expressed as the cobalt-time-yield (CTY): the number of moles of CO converted per gram of Co per second. The results demonstrated that the atmosphere composition used during thermal decomposition of the dried impregnate as well as the reduction temperature had a large impact on the CTY of the catalysts. The highest CTY ($5.4\times10^{-5}$ $mol_{CO}.g_{Co}.s^{-1}$) was observed for catalyst G/D-NC, however, its activity depended largely on the reduction temperature as the activity continued to increase up to a reduction temperature of 550 °C. Both for G/D-AC and G/D-NC, the activity decreased when a reduction temperature higher than 550 °C was used, presumably due to sintering of the Co metal particles. The CTY values of catalysts G/D-AC and G/D-$H_2$ were significantly lower than that of the G/D-NC catalysts, and though the activities improved by increasing the reduction temperature from 350 to 450 °C further increase of the temperature had little effect. The observed differences between the NO/He and air calcined catalysts could be explained by the large differences in $Co_3O_4$ particle sizes. For the air calcined sample relatively large particles of 8 to 60 nm were found. As a result reduction proceeds relatively facile at lower temperatures, and applying higher temperatures had little effect on the activity. On the contrary, reduction tends to proceed more slowly for highly dispersed metal oxide phases, and applying higher reduction temperatures, therefore, improved the degree of reduction of the small $Co_3O_4$ of catalyst G/D-NC significantly. Recently Bezemer *et al.*[6] found with carbon nanofiber supports an

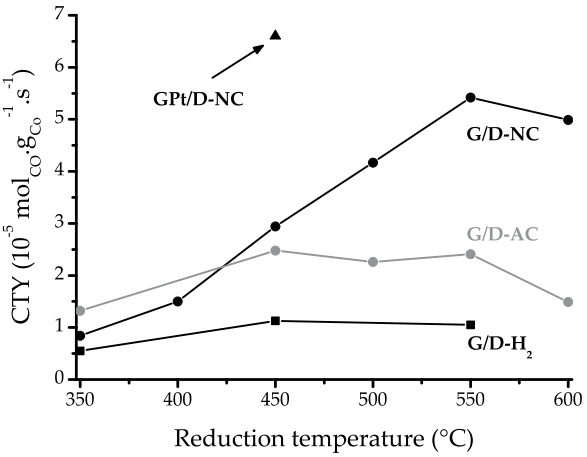


*Figure 5.* Relation between the FT activity and reduction temperature for different samples as indicated.

optimal Co metal particle size of 6 to 8 nm for FT synthesis. Assuming that a similar particle size effect is also relevant for $Co/SiO_2$ catalysts, the Co metal particles obtained from catalyst G/D-NC would not have an optimal size. This implied that the increased activity, in principle, also be related to formation of somewhat larger Co particles by sintering during reduction at higher temperatures.[9] Since re-oxidation of the Co metal phase upon exposure to air hampers XRD crystal size determination, we carried out an experiment in which catalyst G/D-NC was reduced at 550 °C, followed by slow oxidation at 400 °C to $Co_3O_4$ with $O_2$. The obtained product was denoted G/D-NC-R-ox and analysed with XRD. Line-broadening analysis of the pattern (Figure 1 and Table 1) yielded an average $Co_3O_4$ crystal of 5 nm. Hence, we concluded that significant sintering of Co metal due to the high-temperature reduction treatment had not occurred.

The use of high reduction temperatures of 550 °C is not desirable. Therefore, we carried out additional experiments with a 0.05 wt% Pt promoted catalyst G/D-NC (labelled GPt/D-NC) as Pt often improves reduction of the metal oxide particles.[26,27] In addition, this allowed us to verify the hypothesis that the large activity improvement upon increasing the reduction temperature indeed was related to the degree of reduction to Co metal. The catalytic results obtained for sample GPt/D-NC after reduction at 450 °C have been included in Figure 5, and demonstrated that addition of Pt reduction promoter led to a highly active catalyst, while a much lower reduction temperature of 450 °C could be used. In fact, the activity was higher than that of the unpromoted catalyst reduced at 550 °C. Next to enhanced reduction, it has been reported that noble metals may have a beneficial effect on the activity.[5,26] Hence, the results with Pt promoter confirmed that the increased activity when higher reduction

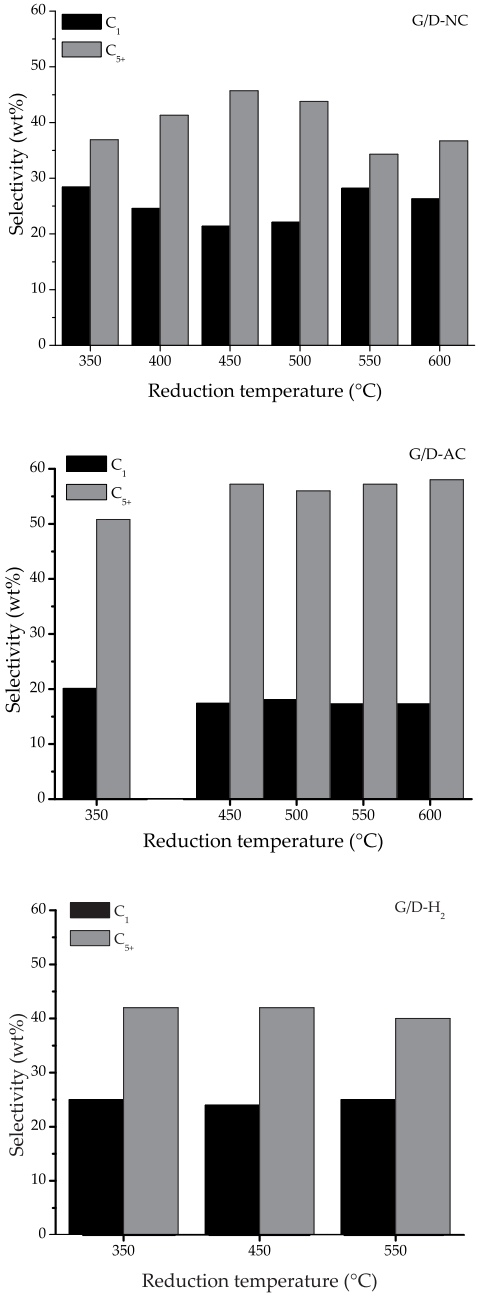


*Figure 6*. $C_1$ and $C_{5+}$ selectivities obtained for G/D-NC, G/D-AC and G/D-$H_2$ catalysts reduced at different temperatures, as indicated.

temperatures were used was related to the degree of Co reduction.

The activity of the catalysts prepared via direct treatment of the dried impregnate in an $H_2$-containing gas flow was relatively low compared to the air and NO/He treated catalysts (Figure 5). To gain insight into the Co metal particle sizes that had been obtained with the 'direct reduction' treatment we treated dried impregnate G/D with $H_2$ at 550 °C, followed by slow oxidation at 400 °C with $O_2$ to obtain $Co_3O_4$ again. The obtained sample was denoted G/D-$H_2$-ox and analysed with XRD. Line-broadening analysis (see Figure 1 and Table 1) indicated that relatively small $Co_3O_4$ crystallites had formed of 6 nm on average. Hence, the activity of these catalysts was unexpectedly low. This might be caused by formation of relatively large amounts of Co phyllosilicates instead of Co metal due to the thermal decomposition of the nitrate precursor in $H_2$, but it remains unclear why this was more extensive than with reduction of the small $Co_3O_4$ particles of the NO/He treated samples.[28]

The selectivities of the catalysts towards $CH_4$ and hydrocarbons with a $C_{5+}$ chain length are given in Figure 6 for the air, NO/He and $H_2$ treated catalysts. The selectivity of the Pt promoted catalyst GPt/D-NC is not included in these plots, but was comparable to that of the G/D-NC catalyst reduced at 550 °C (28 wt% for $C_1$ and 35 wt% for $C_{5+}$). The results showed that the selectivity towards $C_{5+}$ of the air calcined catalysts (G/D-AC) was higher than those of the NO/He and $H_2$ treated catalysts. This could be ascribed to the relatively large Co particles formed upon air calcination as the $C_{5+}$ selectivity tends to increase with the Co particle size.[6] Next to particle size, the difference in the extend of Co clustering (Figure 4) could also have affected the selectivity of the air calcined catalyst as Borg *et al.*[29] recently showed that more extensive clustering of Co metal particles improved the selectivity. The reduction temperatures used for catalysts G/D-AC and G/D-$H_2$ to bring about the Co metal phase had a relatively small impact on the observed $C_{5+}$ selectivities of ~57 wt% and 42 wt%, respectively, whereas the $C_{5+}$ selectivities obtained with the G/D-NC catalysts varied from 37 to 46 wt%. We could not yet establish a correlation between the reduction temperatures and $C_{5+}$ selectivities of the latter catalysts, and further research is required.

To conclude, the $C_{5+}$ selectivity of the NO/He catalysts was lower than that of the air calcined catalysts, which may call for addition of an oxidic promoter[12,13] for these catalysts that display superior activity.

## Conclusions

Using ordered mesoporous SBA-15 as model support and incipient wetness impregnation of aqueous $[Co(OH_2)_6](NO_3)_2$ precursor solutions, the preparation of $Co/SiO_2$ catalysts for the Fischer-Tropsch synthesis of hydrocarbons from a mixture of $H_2/CO$ was studied. After impregnation and drying the cobalt nitrate precursor appeared well-dispersed inside the mesopores, however, severe sintering and redistribution during the air calcination step led to formation of large rodlike $Co_3O_4$

particles of 10 to 100 nm inside the mesopores of SBA-15. We identified a novel thermal treatment in NO/He that prevented the sintering and enabled preparation of small and uniform $Co_3O_4$ particles of 3 to 5 nm at a Co metal loading of 15 wt%.

Experiments with silica gel demonstrated that this method was applicable to conventional supports too as changing from air flow to NO/He flow led to $Co_3O_4$ particles of 3 to 5 nm instead of 8 to 60 nm, respectively. The smaller $Co_3O_4$ particles formed via heat treatment in NO/He flow appeared more difficult to reduce than the air calcined samples as the activity largely depended on the reduction temperature used. The highest activity of $5.4\times10^{-5}$ $mol_{CO}.g_{Co}^{-1}.s^{-1}$ was obtained after reduction at 550 °C. By addition of Pt reduction promoter to the catalyst the reduction temperature could be lowered to 450 °C without loss of activity.

Preparation of the catalyst by our new method led to an increase in activity by more than a factor of two compared to the catalysts treated through calcination in air flow. The catalysts treated via the so-called 'direct reduction' method with $H_2$ showed a low activity possibly due to formation of Co phyllosilicates. Hence, thermal decomposition of the cobalt nitrate precursor in NO/He flow is a facile method to obtain highly active FT catalysts by the impregnation and drying method using $Co(NO_3)_2.6H_2O$ precursor salt.

**Acknowledgments**

Johan den Breejen is thanked for carrying out Fischer-Tropsch catalysis and reduction/oxidation experiments. Prof. J.W. Geus and Hans Meeldijk are acknowledged for their support with TEM characterisation.

**References**

1. Fischer, F.; Tropsch, H. *Brennstoff-Chemie* **1923**, *4*, 276-285.
2. Iglesia, E. *Appl. Catal. A* **1997**, *161*, 59-78.
3. Dry, M. *Catal. Today* **2002**, *71*, 227-241.
4. Kroschwitz, I.; Howe-Grant, M. *Kirk-Othmer encyclopedia of chemical technology* **1996**, Wiley & Sons, New York, 4th edn.
5. Khodakov, A.Y.; Chu, W.; Fongarland, P. *Chem. Rev.* **2007**, *107*, 1692-1744.
6. Bezemer, G.L.; Bitter, J.H.; Kuipers, H.P.C.E.; Oosterbeek, H.; Holewijn, J.E.; Xu, X.; Kapteijn, F.; Van Dillen, A.J.; De Jong, K.P. *J. Am. Chem. Soc.* **2006**, *128*, 3956-3964.
7. Girardon, J-S.; Lermontov, A.S.; Gengembre, L.; Chernavskii, P.A.; Griboval-Constant, A.; Khodakov, A.Y. *J. Catal.* **2005**, *230*, 339-352.
8. Van de Loosdrecht, J.; Barradas, S.; Caricato, E.A.; Ngwenya, N.G.; Nkwanyana, P.S.; Rawat, M.A.S.; Sigwebela, B.H.; Van Berge, P.J.; Visagie, J.L. *Top. Catal.* **2003**, *26*, 121-127.

9. Riva, R.; Miessner, H.; Vitali, R.; Del Piero, G. *Appl. Catal., A* **2000**, *196*, 111-123.
10. Barbier, A.; Tuel, A.; Arcon, I.; Kodre, A. and Martin, G.A. *J. Catal.* **2001**, *200*, 106-116.
11. Ernst, B.; Libs, S.; Chaumette, P. and Kiennemann, A. *Appl. Catal., A* **1999**, *186*, 145-168.
12. Morales, F.; Grandjean, D.; De Groot, F.M.F.; Stephan, O.; Weckhuysen, B.M. *Phys. Chem. Chem. Phys*. **2005**, *7*, 568-572.
13. Bezemer, G.L.; Falke, U.; Van Dillen, A.J.; De Jong, K.P. *Chem. Commun.* **2005**, 731-733.
14. Van Dillen, A.J.; Terörde, R.J.A.M.; Lensveld, D.J.; Geus, J.W.; De Jong, K.P. *J. Catal.* **2003**, *216*, 257-264.
15. Soled, S.L.; Iglesia, E.; Fiato, R.A.; Baumgartner, J.E.; Vroman H.; Miseo, S. *Top. Catal.* **2003**, *26*, 101-109.
16. Zhao, D.; Feng, J.; Huo, Q.; Melosh, N.; Fredrickson, G.H.; Chmelka, B.F.; Stucky, G.D. *Science* **1998**, *279*, 548-552.
17. Jaroniec, M.; Kruk, M.; Olivier, J.P.; Koch, S. *Stud. Surf. Sci. Catal.* **2000**, *128*, 71-80.
18. Barrett, E.P.; Joyner, L.S.; Halenda, P.P. *J. Am. Chem. Soc.* **1951**, *73*, 373-380
19. Harkins, W.D.; Jura, G. *J. Am. Chem. Soc.* **1944**, *66*, 1366-1373.
20. Kruk, M.; Jaroniec, M.; Sayari, A. *Langmuir* **1997**, *13*, 6267-6273.
21. Lippens, B.C.; De Boer, J.H. *J. Catal.* **1965**, *4*, 319-323.
22. Ravikovitch, P.I.; Neimark, A.V. *Langmuir* **2002**, *18*, 9830-9837.
23. Janssen, A.H; Yang, C.-M.; Wang, Y.; Schüth, F.; Koster, A.J. De Jong, K.P. *J. Phys. Chem. B* **2003**, *107*, 10552-10556.
24. Vradman, L.; Landau, M.V.; Kantorovich, D.; Koltypin, Y.; Gedanken, A. *Micropor. Mesopor. Mater.* **2005**, *79*, 307-318.
25. Van Der Voort, P.; Ravikovitch, P. I.; De Jong, K. P.; Benjelloun, M.; Van Bavel, E.; Janssen, A. H.; Neimark, A. V.; Weckhuysen, B. M.; Vansant, E. F. *J. Phys. Chem. B.* **2006**, *106*, 5873-5877.
26. Iglesia, E.; Soled, S.L.; Fiato, R.A.; Via, G.H. *J. Catal.* **1993**, *143*, 345-368.
27. De Jong, K.P.; Glezer, J.H.E.; Post, M.F.M. *European Patent* No. 0221598 **1986**.
28. Puska, I.; Fleisch, T.H.; Full, P.R.; Kaduk, J.A.; Marshall, C.L.; Meyers, B.L. *Appl. Catal. A* **2006**, *311*, 146-154.
29. Borg, Ø.; Eri, S.; Blekkan, E.A.; Storsæter, S.; Wigum, H.; Rytter, E.; Holmen, A. *J. Catal.* **2007**, *248*, 89-100.

# 7

# PCP- and SCS-pincer palladium complexes immobilised on ordered mesoporous silicas: application in C–C bond formation reactions

ECE-pincer palladium(II) complexes (ECE = $(C_6H_3(CH_2E)_2\text{-}2,6)^-$, E = $PPh_2$ and SPh) tethered to a trialkoxysilane moiety through a carbamate linkage were immobilised on ordered mesoporous silicas SBA-15 and MCM-41 using a grafting process. The resulting hybrid materials were characterised by IR spectroscopy (DRIFT), solid-state CP/MAS NMR ($^{13}C$, $^{31}P$, and $^{29}Si$), and elemental analyses. These analyses showed the integrity of the pincer-metal complexes on the supports, which highlights their stability under the applied immobilisation conditions. An H-bonding interaction between the carbamate carbonyl group of the complex and free silanol groups on the silica surface was also established. The hybrid materials were found to act as Lewis acid catalysts in the aldol reaction between methyl isocyanoacetate and benzaldehyde. SBA-15 modified with the PCP-pincer Pd-complex was used in up to five runs without loss of activity. Control experiments showed the true heterogeneous nature of the catalyst in this reaction. $N_2$-physisorption data, XRD, and TEM/EDX analyses of the hybrid materials revealed that the mesoporous structure of these materials was retained during the immobilisation process as well as during catalysis.

## Introduction

Catalyst separation from the product solution is an important aspect of homogeneous catalytic processes both from an economical and ecological point of view. Amongst current methods to separate homogeneous catalysts from product streams are distillation and selective extraction of products and catalysts.[1] In many cases these methods may turn out as unsustainable, however, due to the excessive use of energy and solvents, and could, therefore, also be economically less attractive. In this respect, heterogeneous catalytic processes have obvious advantages due to the ease of separation of the (insoluble) heterogeneous catalysts from reaction products. Current research is directed to merge the advantages of both catalytic approaches, for example, by immobilising homogeneous catalysts on an insoluble support.[2,3] In this way, properties such as catalyst selectivity and activity could be combined with ease of catalyst separation and catalyst reuse. A variety of insoluble supports have been used for the immobilisation of homogeneous catalysts. ,

ECE-pincer metal complexes (ECE= $(C_6H_3(CH_2E)_2\text{-}2,6)^-$, E= $NR_2$, SR, $PR_2$ etc.) are often highly stable and resistant to metal leaching due to a strong M–C σ-bond that is stabilised through metal coordination by two hetero-atoms (cis to the M–C bond) forming two five-membered chelate rings.[6] ECE-pincer Pd-complexes are known to catalyse a large variety of C–C and C–X bond formation reactions.[6-10] The robustness of the ECE-pincer metal complexes make them attractive candidates for processes for which recycling and reuse is a prerequisite. Various soluble supports have already been used for the immobilisation and recycling of pincer-based metal catalysts, among which are hyperbranched polymers,[9,11] oligo(ethylene glycol)[12], dendronised polymers[13], carbosilane dendrimers[14], cartwheel-molecules,[8,15] polycationic dendrimers[16], and soluble polymers[10,17]. Recently, we as well as others have reported on the grafting of ECE-pincer metal complexes on silica and on their use in aldol-type[18,19] and Heck[20] reactions.

In a recent effort by our group to immobilise NCN-pincer complexes on insoluble supports, we have used *para*-triethoxysilane-functionalised pincer-metal (platinum and palladium) complexes and immobilised these on conventional silica gel via surface grafting.[18] Although the heterogenised pincer Pd-complexes were found to be active in the aldol reaction of methyl isocyanoacetate (MI) with benzaldehyde (reaction 1), they showed a poor performance in terms of recycling. For a series of conventional silicas differing in macroscopic particle size (50 μm - 1.5 mm) and pore diameter (15 - 50 nm) significant losses of more than 50% between the first and second run were observed for the heterogenised catalysts. No indication could be derived for a relation between the macroscopic particle size and average pore diameter of the silicas, and the degree of catalyst leaching from the support. Presumably during the reaction, attrition of the catalyst took place due to partial hydrolysis of the silica surface. As a result, part of the catalyst was removed from the support in the form of small, difficult to separate by filtration and thus non-recyclable silica particles.

Recent investigations on the mechanism of operation of ECE-pincer palladium(II)

complexes as homogeneous catalyst have shown that the NCN- and SCS-pincer Pd-complexes undergo isocyanide insertion in the Pd–C bond and that the resulting cyclometalated species are the actual catalytically active species.[21] Remarkably, this insertion takes place for both the neutral halide and the cationic aquo complexes. For the PCP-pincer Pd-complexes, no insertion was observed, but replacement of the halide by a $\eta^1$-coordinated isocyanide generated the cationic, catalytically active species. Finally, this study showed that there is no need to generate a cationic palladium(II) species by prior treatment of the neutral species with e.g. Ag-reagents (note that Ag-halide salts are catalysts themselves) for the ECE-pincer palladium species to catalyse reaction 1.

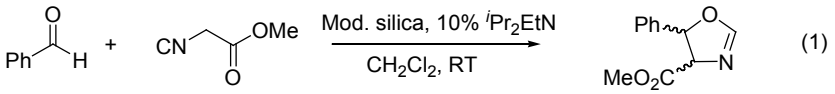


MI *cis*/*trans* oxazoline

*Reaction 1.* Aldol condensation reaction between benzaldehyde and methyl isocyanoacetate (MI).

In the present study, we have used our experience to immobilise NCN-pincer palladium complexes for the immobilisation of the corresponding PCP- and SCS-pincer palladium complexes on silica.[18] To this end, complexes **1** and **2** (Chart 1) were synthesised[23] and subsequently immobilised on silica-based support materials. The choice of support depended on the reaction conditions, ease of functionalisation of the surface groups required for attaching the catalyst, as well as on the chemical, mechanical and thermal stability of the support.[5] In the present study, we have used the ordered mesoporous molecular sieves MCM-41[24] and SBA-15[25], which fulfil most of the above mentioned requirements and have been used extensively by others.[3,26] Moreover, their well-defined structure may provide uniform active sites with well-controlled steric effects of the support.[27] The synthesis and characterisation of the pincer palladium-functionalised MCM-41 and SBA-15 materials as well as their performance in reaction 1 are discussed.

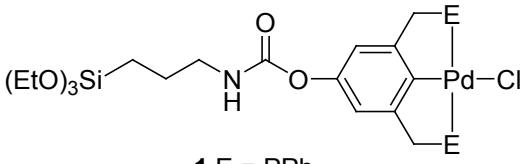


*Chart 1.* Siloxane-functionalised ECE-pincer palladium(II) chloride complexes

## Experimental

*General*

Solvents were dried over appropriate materials and distilled prior to use. All reagents were obtained from commercial sources and were used without further purification. All siloxane materials were stored under a $N_2$ atmosphere. Compounds **1** and **2** were synthesised using a previously reported procedure.[23] $^{13}C$ (75.5 MHz), $^{29}Si$ (59.6 MHz), and $^{31}P$ (121.5 MHz) CP/MAS (cross-polarisation/magic angle spinning) NMR spectra of 3 and 4 were recorded on a Varian Inova 300 spectrometer (Spinning rate 6000 Hz, contact time for $^{13}C$ 1.50 ms, for $^{29}Si$ 3.0 ms, and for $^{31}P$ 2.5 ms; number of transients for $^{13}C$ 6068, for $^{29}Si$ 11336, and for $^{31}P$ 3840). $^{13}C$ (188.6 MHz), $^{29}Si$ (149.0 MHz), and $^{31}P$ (303.7 MHz) CP/MAS NMR spectra of **5** were recorded on a Bruker AV-750 spectrometer (Spinning rate 12 kHz, contact time for $^{13}C$ 2.048 ms, for $^{29}Si$ 10.24 ms, and for $^{31}P$ 2.048 ms; number of transients for $^{13}C$ 30916, for $^{29}Si$ 23484, and for $^{31}P$ 3920). FT-IR and DRIFT spectra were recorded using a Mattson Instruments Galaxy Series FTIR 5000 spectrometer with SPECAC diffuse-reflectance assembly or Perkin Elmer Spectrum One FT-IR spectrometer with Universal ATR sampling accessory. Gas chromatographic analyses were performed with a Perkin Elmer Autosystem XL GC using a 30 m, PE-17 capillary column with an FID detector. Microanalyses were obtained from H. Kolbe Mikroanalytisches Laboratorium, Mülheim an der Ruhr, Germany. $N_2$-physisorption was carried out at -196 °C using a Micromeritics Tristar 3000 apparatus. The samples were dried in He flow for 14 hours at 120 °C prior to analysis. The pore size distribution, micro- and meso-porosity were derived from the adsorption branch of the isotherm using a NL-DFT model developed by Jaroniec *et al.*[28] for ordered mesoporous silica supports with cylindrical pore geometry. The total pore volume was determined at $p/p_o = 0.995$, whereas the mesopore surface area was calculated with the t-method[29] using a thickness range of 0.35-0.55 nm. Powder X-ray diffraction (XRD) patterns of MCM-41 and hybrid material derived from it (**4**) were obtained from 1.5 to 10° 2θ with a Philips PW1710 setup using Cu-K$\alpha$ radiation. XRD patterns of SBA-15 and hybrid materials derived from it (3 and 5) have been recorded using a Bruker-Nonius D8 Advance X-ray Diffractometer using Co-$K_{\alpha 12}$ radiation. Transmission Electron Microscopy (TEM) analysis was performed using a Tecnai 20 microscope operating at 200 kV and equipped with an Energy Dispersive X-ray Spectrometer (EDX).

*Support preparation*

MCM-41 and SBA-15 were prepared according to reported procedures.[24,25] For the MCM-41 synthesis Degussa Aerosil380 was used as silica source and cetyltrimethylammoniumbromide as surfactant (Acros). Surfactant was dissolved in demineralised water followed by the addition of a mineralising agent (20 wt% tetraethylammoniumhydroxide in water, Acros). To the resulting solution silica was added under vigorous stirring. The molar composition of the resulting mixture was 1 $SiO_2$ : 0.27 CTABr : 0.19 TEAOH : 40 $H_2O$. After 24 hours the viscous gel was

transferred to a teflon-lined autoclave and statically aged at 150 °C for 72 hours under autogeneous pressure. The product was collected by washing with demineralised water, filtration, drying in air for 12 hours at 120 °C and calcination for 6 hours at 550 °C to remove the surfactant. For the synthesis of SBA-15, 8 g of $EO_{20}PO_{70}EO_{20}$ surfactant (P123) was dissolved in 250 ml demineralised water of 40 °C. After the solution had become clear, 48 g of concentrated HCl (Merck) was added, followed by the addition of 21.5 ml of tetraethyl orthosilicate (Acros). Next, the mixture was stirred for 20 hours at 40 °C after which it was transferred to an oven for further reaction at 80 °C for 48 hours. The solid product was collected from the suspension by filtration, washed, dried in air for 12 hours at 80 °C and calcined for 6 hours at 550 °C.

*Grafting procedures*

A typical procedure for silica **3** consisted of pretreating 3 g of mesoporous silica (SBA-15) by heating it at 100 °C under vacuum for 2 hours. After allowing it to cool to room temperature, a solution of **1** (0.28 mmol) in dry toluene (100 mL) was introduced. The resulting mixture was stirred to form a suspension and heated at 90 °C for 20 hours, after which the silica was allowed to settle and the supernatant liquid was decanted. The silica was washed twice with dry $CH_2Cl_2$ (50 mL) and was subjected to Soxhlet extraction using $CH_2Cl_2$ for 16 hours. Finally, it was dried under vacuum yielding 3.2 g of solid **3**. IR (KBr, DRIFT): υ ($cm^{-1}$) 3065, 2982, 2939, 2902 (C–H, stretching); 1725 (C=O, stretching); 1514 (CHN group); 1438 (N–H, bending). CP/MAS $^{13}$C NMR (75.5 MHz, 25 °C): δ 8.62 (SiCH2); 16.68 (OCH2CH3); 29.4 (*C*H2); 40.27 (ArCH2P and NHCH2); 58.61 (OCH2); 121.69, 129.15, 131.57, 132.8, 141.65, 153.94, 157.57 (Ar*C*); 160.59 (C=O). CP/MAS $^{31}$P NMR (121.5 MHz, 25 °C): δ 36.01. CP/MAS $^{29}$Si NMR (59.6 MHz, 25 °C): δ -108.66, -101.34. Anal. Found: C, 4.96; P, 0.85; Pd, 0.82 (molar ratio of P/Pd = 2; found 3.6).

Complex **2** (15.2 mg, 0.021 mmol) and 0.5 g of MCM-41 gave 0.5 g of silica **4** in a similar procedure as for silica **3**. IR (KBr, DRIFT): υ ($cm^{-1}$) 2995, 2959, 2858 (C–H, stretching); 1726 (C=O, stretching); 1465 (N–H, bending); 1395. CP/MAS $^{13}$C NMR (75.5 MHz, 25 °C): δ 8.01 ($SiCH_2$); 17.18 ($OCH_2CH_3$); 23.44 ($CH_2$); 42.0 ($NHCH_2$); 49.3 ($ArCH_2S$); 59.73 ($OCH_2$); 118.74, 127.29, 130.21, 132.63, 148.77, 152.11, 155.23, 162.95 (Ar*C*); 165.45 (C=O). CP/MAS $^{29}$Si NMR (59.6 MHz, 25 °C): δ -107.91, -99.64, -90.96. Anal. Found: C, 1.71; S, 0.28; Pd, 0.43; (molar ratio of S/Pd = 2; found 2.17).

Synthesis of silica **5** was carried out by suspending 2.37 g of silica **3** in a mixture of hexane (20 ml) and 1,1,1,3,3,3-hexamethyldisilazane (10 ml) and stirred at ambient temperature for 20 hours, after which the silica was allowed to settle and the supernatant liquid was decanted. The silica was washed twice with dry $CH_2Cl_2$ (50 ml) and dried under vacuum yielding 2.2 g of solid 5. IR (KBr, DRIFT): υ ($cm^{-1}$) 3063, 2963, 2905 (C–H, stretching); 1756 (C=O, stretching); 1501 (CHN group); 1485, 1438 (N–H, bending). CP/MAS $^{13}$C NMR (188.64 MHz, 25 °C): δ -0.5 ($SiCH_3$); 7.9 ($SiCH_2$); 17.1 ($OCH_2CH_3$); 22.6 ($CH_2$); 43.2 ($ArCH_2P$ and $NHCH_2$); 58.8 ($OCH_2$); 117.5, 128.8, 132.6, 145.1 (Ar*C*); 150.4 (C=O). CP/MAS $^{31}$P NMR (303.7 MHz, 25 °C): δ 30.2.

CP/MAS $^{29}$Si NMR (149.0 MHz, 25 °C): δ -108.2, -59.4, -52.1, -45.5, 13.9. Anal. Found: C, 7.66; P, 0.58; Pd, 0.57 (molar ratio of P/Pd = 2; found 3.4).

*Catalysis*

The catalytic experiments were carried out using $^{i}Pr_2EtN$ (Hunig's base, 10 mol%) as a base, hybrid silica materials as catalyst, and methyl isocyanoacetate (1.6 mmol) and benzaldehyde (1.6 mmol) as reagents in $CH_2Cl_2$ (5 mL) at room temperature. The reaction progress was monitored by means of GC analysis using pentadecane as internal standard. After each run, the complete reaction mixture was centrifuged and the supernatant was separated. The remainders were washed with $CH_2Cl_2$ (2× 20 ml) and dried in vacuo. The obtained solid was used for the next run.

## Results and discussion

*Immobilisation of PCP- and SCS-pincer palladium complexes on silica*

The triethoxysilane-functionalised complexes **1** and **2** (Chart 1) were prepared from the corresponding para-hydroxy ECE-pincer complexes as reported previously.[23] These complexes comprise both a trialkoxysilane and an organometallic fragment covalently connected through a carbamate linker. The presence of a long, non-polar tail increases the solubility of these complexes considerably. They are soluble in non-polar solvents such as benzene or toluene, which allows the use of common grafting protocols of homogeneous catalysts on silica in these solvents. This is of importance to arrive at a uniform distribution of the catalyst on the support.

Silica surface grafting of **1** and **2** was carried out using SBA-15 or MCM-41. In a typical process, the silica support was pre-treated by heating it at 100 °C under vacuum for two hours. The support was then reacted with complexes **1** or **2** in toluene at 90 °C for 20 hours (Scheme 1). A continuous extraction (Soxhlet) of the resulting material with boiling dichloromethane was subsequently performed for 16 hours

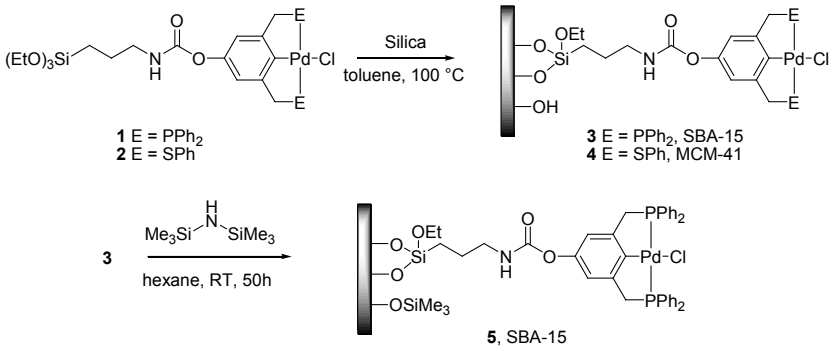


*Scheme 1.* Synthesis of hybrid materials **3**, **4**, and **5**.

in order to remove any non-covalently attached material. After drying in vacuo, the hybrid silicas **3** and **4**, respectively, were obtained as white solids. Subsequently, silica **3** was treated with 1,1,1,3,3,3-hexamethyldisilazane (HMDS) to cap remaining unreacted surface silanol groups with a trimethylsilyl functionality (silica **5**).

These materials were characterised by using IR spectroscopy (DRIFT), CP/MAS NMR spectroscopy ($^{13}C$, $^{29}Si$, and $^{31}P$), and elemental analysis. The impact of the immobilisation of **1** and **2** on the structure of MCM-41 and SBA-15 was studied by Powder X-ray diffraction (XRD), Transmission Electron Microscopy (TEM), and $N_2$-physisorption.

*IR studies*

Comparison of the IR (DRIFT) spectra of the pristine silicas (SBA-15 in Figure 1) with those of hybrid materials **3** (see Figure 1) and **4** pointed to a strong decrease in the number of isolated free silanol groups in the latter silicas. Comparison of the IR spectra of **1** and **2** with those of the hybrid materials **3** and **4** revealed that signals corresponding to the C–H stretching, C=O stretching, CNH group, and the N–H bending vibrations of **1** and **2** are present in the spectra of **3** and **4**. The intensity of the signal for isolated free silanol groups in **3** is further decreased in the spectrum of **5** (see Figure 1), showing that at least part of the remaining silanol groups in **3** became capped with a TMS group in **5**. By subtracting the spectrum of plain SBA-15 from that of **5**, a difference spectrum was obtained (top, Figure 2). In this difference spectrum, a sharp decrease in the intensity of the signal at 3745 $cm^{-1}$ was observed indicating that a large number of silanol groups had reacted. Other significant changes were observed for the carbamate C=O stretching vibration. In **1** the υ C=O

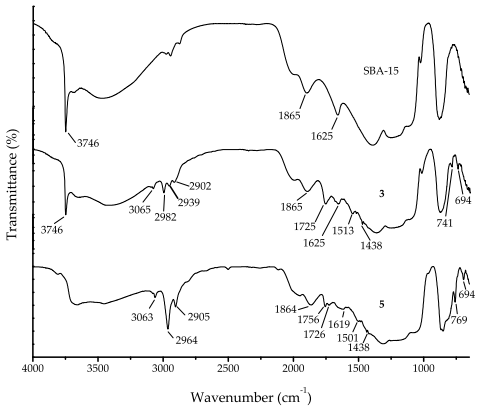


*Figure 1.* IR (DRIFT) spectra of pristine silica SBA-15 and hybrid materials **3** and **5**.

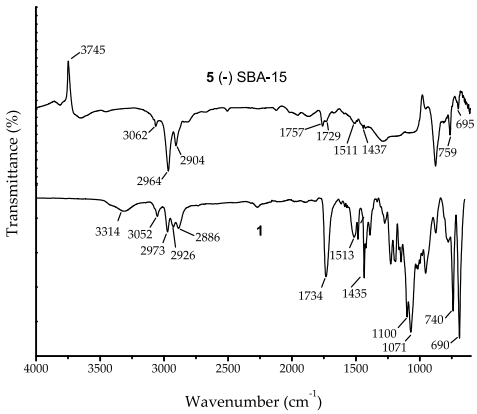


*Figure 2.* Difference spectrum between the DRIFT spectra of **5** and pristine silica SBA-15 (top) compared with the IR spectrum of non-supported complex **1** (bottom).

amounted to 1734 $cm^{-1}$ (see Figure 2), which changed to 1725 $cm^{-1}$ in hybrid material **3**, and to 1756 $cm^{-1}$ in TMS-capped **5** (see Figure 1). We believe that these shifts are indicative for the presence of H-bonding interactions of the carbamate-carbonyl group with surface silanol groups in **3**, which consequently are much less present in **5**. This observation is consistent with previous observations made on immobilising related NCN-pincer complexes on silica.[18]

*CP/MAS solid state NMR studies*

$^{13}C$ and $^{29}Si$ solid-state NMR spectroscopy on **3**, **4**, and **5** provided further information on the nature of both the organic (spacer and metal-complex) and inorganic part of these hybrid materials. All peaks corresponding to the $^{13}C$ NMR spectra of the parent complexes **1** and **2** were present in the $^{13}C$ NMR spectra of the hybrid materials **3** and **4**, respectively. The $^{31}P$ NMR spectrum of solid **3** (on SBA-15) showed a single peak at 36.01 ppm, while for **1** a resonance at 33.4 ppm (solution NMR in $C_6D_6$) was found which corresponds to a phosphine grouping coordinated to palladium. Signals at 16 and 58 ppm in the $^{13}C$ NMR spectra of all hybrid materials pointed to the presence of EtO–Si groups.[23] This supports the notion that not all tethered palladium complexes became immobilised via three Si(surface)–O–Si bonds, but rather that grafting occurred through an average of less than or equal to three bonds. The $^{29}Si$ NMR spectrum of **5** indeed showed all three $T^n$ type signals at -59, -52, and -45 ppm, corresponding to $T^3$, $T^2$, and $T^1$ types of organosilica species, respectively (Figure 3, inset; $T^n = RSi(OSi)_n(OEt)_{3-n}$). In addition, the latter spectrum also showed a signal at 13.9 ppm, which can be assigned to Si(surface)–O–*Si*$Me_3$ groups derived from surface silanols capped with a $Me_3Si$ grouping arising from HMDS treatment of the

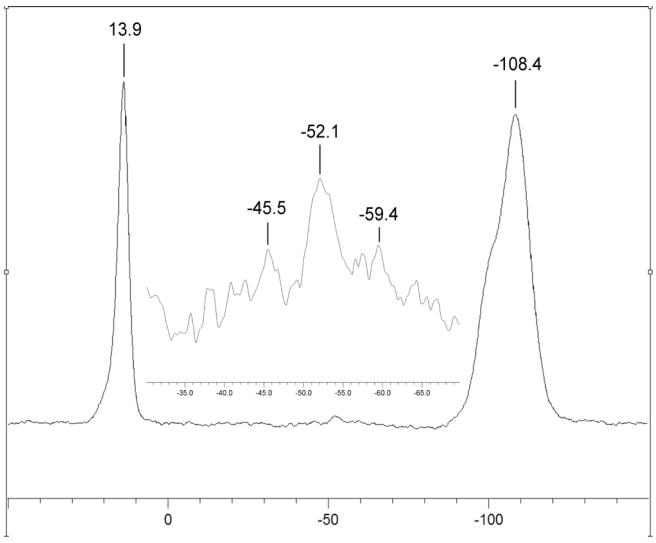


*Figure 3.* CP/MAS Solid-State $^{29}Si$ NMR of **5** (inset: expansion of –30 to –70 ppm region).

*Table 1.* Elemental analyses of the hybrid materials **3**-**5**.

| Sample | wt% C[a] (mmol.g$^{-1}$) | wt% Pd (mmol.g$^{-1}$) | wt% E[c] (mmol.g$^{-1}$) | E/Pd[d] | | C/E[d] | |
|---|---|---|---|---|---|---|---|
| | | | | Calc. | Found | Calc. | Found |
| **3** | 4.96 (4.13) | 0.82 (0.077) | 0.85 (0.275) | 2.0 | 3.6 | 18 | 15 |
| **4** | 1.71 (1.43) | 0.43 (0.040) | 0.28 (0.087) | 2.0 | 2.2 | 15 | 16 |
| **5** | 7.66 (6.38) | 0.57 (0.054) | 0.58 (0.187) | 2.0 | 3.4 | - | - |

[a]% by weight; [b]in brackets, mmol.g$_{SiO2}^{-1}$; [c]E=S for SCS and P for PCP; [d]atom ratio.

hybrid material **3**. Two signals were observed for the $SiO_2$ framework of **3** at -108 and -101 ppm, respectively, corresponding to $Q^4$ and $Q^3$ species ($Q^m$ = $Si(OSi)_m(OH)_{4-m}$), whereas for **5** a signal at -108 ppm ($Q^4$ species) along with a shoulder at about -100 ppm (decreased number of $Q^3$ species) was observed, which is in accordance with the partial $SiMe_3$-capping of silanol groups ($Q^3$ species) in **5** (*vide supra*).

*Elemental analysis*

The palladium, sulphur, phosphorus, and carbon contents of the grafted silicas were determined by ICP analysis (Table 1). The E/Pd ratio (E= S or P) was close to two for **4** as expected from its formula. In the case of **3** and **5**, this ratio was found to be higher than two, which could point to loss of Pd from the PCP-pincer ligand during the grafting process. $^{31}P$ NMR analysis of these materials did, however, not show the presence of free phosphine or of phosphine oxide moieties. In addition, no Pd(0) formation was observed during the immobilisation reaction, which justifies the conclusion that the complex remained intact. In the case of **5**, an increase of the carbon content was found, which most likely is due to the capping of some of the free silanol groups of SBA-15 with $SiMe_3$ groups.

*$N_2$-physisorption*

In order to gather information on changes in surface properties at various stages of the synthesis of silicas **3**, **4** and **5**, the materials were studied using $N_2$-physisorption. The results are summarised in Table 2 and some selected isotherms are shown in Figure 4. To ascertain the effect of the conditions of the immobilisation process on the ordered structure of SBA-15, we refluxed pristine SBA-15 at 85 °C in toluene for 24 hours. The $N_2$-physisorption isotherm (Figure 4a) of the obtained product contained the typical features: a high onset at low relative pressures originating from the intra-wall microporosity, and hysteresis at higher values because of the ordered mesoporous channels. The small relative pressure region ($p/p_o$= 0.69 - 0.71) in which the single-step capillary condensation took place is a consequence of the uniform mesopore diameter of 8.7 nm. The BET surface area and mesopore volume remained unaffected by the treatment. Next, the impact of the silanol capping treatment with HMDS was addressed by treating blank SBA-15. The isotherm (Figure 4a) showed

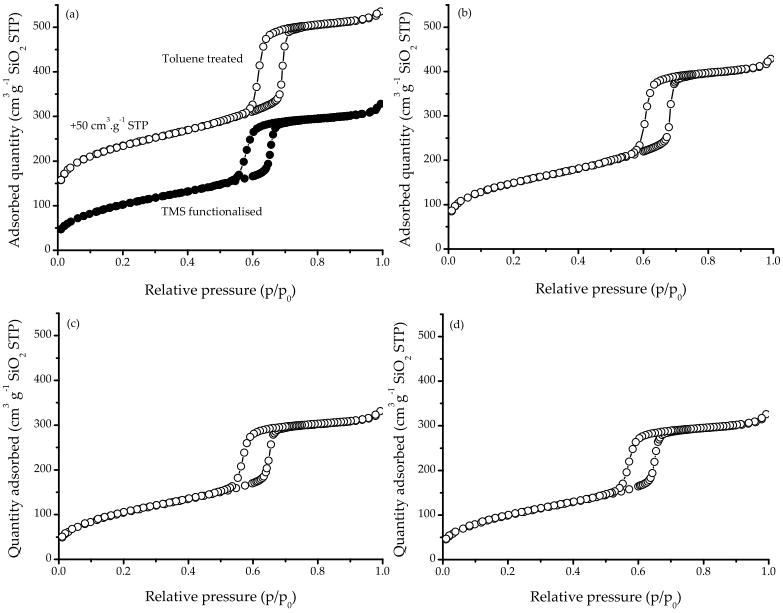


*Figure 4.* $N_2$-physisorption isotherms of SBA-15 after toluene or HMDS treatment (a), functionalised material **3** (b) and **5** (c), and **5** after five catalytic runs (d).

*Table 2.* $N_2$-physisorption results of functionalised silica samples.

| **Sample** | $S_{BET}$ [a] | $d_{Pore}$ | $V_{micro}$ [e] | $V_{meso}$ [f] | $V_{tot}$ [e] |
|---|---|---|---|---|---|
| | **($m^2.g^{-1}$)** | **(nm)** | **($cm^3.g^{-1}$)** | **($cm^3.g^{-1}$)** | **($cm^3.g^{-1}$)** |
| SBA-15 | 518 | 8.7 | 0.09 | 0.73 | 0.78 |
| SBA-15 (toluene) | 504 | 8.7 | 0.09 | 0.71 | 0.75 |
| SBA-15 (HMDS) | 460 | 7.8 | 0.00 | 0.49 | 0.54 |
| **3** | 442 | 8.2 | 0.05 | 0.62 | 0.66 |
| **5** | 433 | 7.9 | 0.00 | 0.47 | 0.51 |
| **5** after run 1 | 416 | 7.9 | 0.00 | 0.45 | 0.49 |
| **5** after run 5 | 423 | 7.9 | 0.00 | 0.46 | 0.50 |
| MCM-41 | 975 | 4.3 | 0.01 | 0.86 | 1.03 |
| **4** | 966 | 4.1 | 0.00 | 0.76 | 0.95 |

[a]$S_{BET}$ = BET surface area; [b]$d_{pore}$ = average pore diameter calculated using NL-DFT; [c]$V_{micro}$ = micropore volume; [d]$V_{meso}$ = mesopore volume; [e]$V_{tot}$ = total pore volume determined at $p/p_o = 0.995$.

that the characteristic SBA-15 features were retained. However, the porosity and average pore size diameter (Table 2) had decreased to 0.49 $cm^3.g^{-1}$ $SiO_2$ and 7.8 nm, respectively. The observed pore diameter decrease could not account for the total porosity decrease, and most likely some of mesopores of SBA-15 became blocked. In addition, after the HMDS treatment no micropore volume was present anymore. Comparison of the $N_2$-physisorption results of pristine SBA-15 and functionalised material **3** (Table 2) showed that the BET surface area and mesopore volume decreased from 518 to 442 $m^2.g_{SiO2}^{-1}$, and from 0.73 to 0.62 $cm^3.g_{SiO2}^{-1}$, respectively. The mesopore diameter had decreased from 8.7 to 8.2 nm due to deposition of complex **1** inside the mesopores of SBA-15. The steep capillary condensation step and hysteresis loop of the isotherm (Figure 4b) showed that the uniform character of the cylindrical mesopores had been retained. The observed mesoporosity reasonably matched the expected value of 0.58 $cm^3.g_{SiO2}^{-1}$ due to the pore diameter decrease of 0.5 nm. Comparison of the textural properties of materials **3** and **5** showed that treatment of **3** with HMDS resulted in a decline of the micropore volume from 0.05 to 0.00 $cm^3.g_{SiO2}^{-1}$, and a further decrease of the mesoporosity to 0.47 $cm^3.g_{SiO2}^{-1}$. Finally, $N_2$-physisorption results obtained after catalysis with material **5** (Figure 4d) showed that the textural properties remained unchanged up to five catalytic runs.

The physisorption results in Table 2 show that immobilisation of the SCS-pincer metal complex **2** onto MCM-41, yielding functionalised material **4**, had little effect on the surface area and total pore volume of the support. Also, the steep capillary condensation mesopore-filling step characteristic for cylindrically shaped mesopores was retained. Although the narrow pore size distribution had been preserved the pore diameter had slightly decreased upon immobilisation of SCS-pincer metal complex **2** from 4.3 to 4.1 nm.

*XRD analysis*

The X-ray diffraction patterns for SBA-15 and corresponding hybrid materials are shown in Figure 5A. The pattern of pristine SBA-15 revealed three well-resolved peaks located at 1.15, 2.0, and 2.3 degrees 2θ, that could be indexed as the (100), (110) and (200) diffraction lines, respectively, associated with a *p6mm* hexagonal symmetry that is typical for SBA-15. Although small variations between the d-spacing values of the (100) diffraction line of the different samples were found, the XRD results demonstrated that the hexagonal symmetry was retained for all the functionalised materials; not only after immobilisation of the complex and HMDS capping of the remaining hydroxyls, but also after five runs of catalysis.

The XRD patterns for blank MCM-41 contained four diffraction lines at 2.1, 3.7, 4.2, and 5.6 degrees 2θ. Again, these could be assigned to the (100), (110), (200) and (210) lattices of the hexagonal lattice of MCM-41, respectively (Figure 5B). Comparison between the patterns obtained for pristine MCM-41 and functionalised material **4** shows that the long range order of the mesopores was not affected by the grafting treatment.

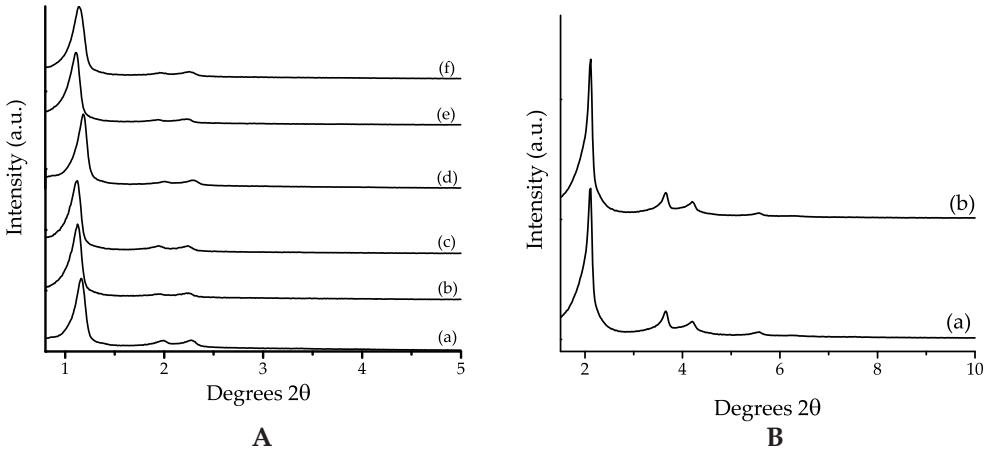


*Figure 5.* A: XRD patterns of (a) SBA-15, (b) SBA-15(HMDS), (c) 3, (d) 5, (e) 5 after run 1 and (f) 5 after run 5; B: XRD patterns of (a) MCM-41 and (b) hybrid material 4.

*TEM/EDX analysis*

TEM analysis of samples of **3** and **5** (SBA-15 materials, Figure 6) as well as of **4** (MCM-41 material; not shown) revealed that the hexagonal mesoporous structures of both SBA-15 and MCM-41 had been retained during immobilisation and consecutive steps in the preparation. Figure 5 shows two typical TEM images of material **5** before catalysis and after **5** catalytic runs. The images demonstrate that the ordered structure of the SBA-15 was retained. Moreover, with TEM no palladium clusters were found in the samples, however, EDX elemental analysis demonstrated that palladium as well as either phosphorous (for **3** and **5**) or sulfur (for **4**) are present in the structures. This indicated that no Pd(0) was formed during the immobilisation

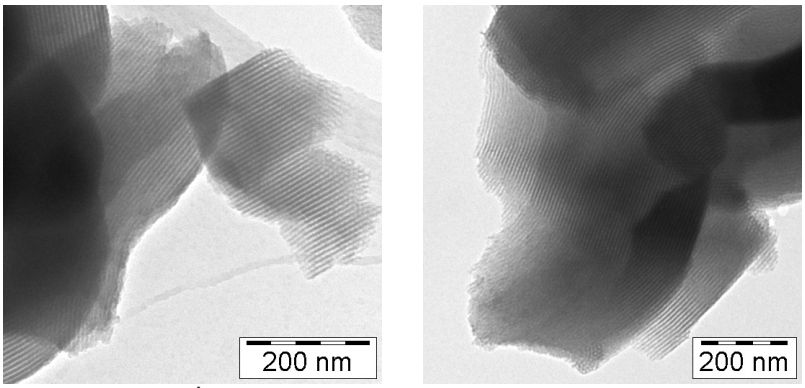


*Figure 6.* TEM of functionalised SBA-15 **5** (A) and **5** after catalysis run 5 (B).

and protection processes and that the organometallic groupings **1** and **2** have been molecularly immobilised.

*Catalysis*

As a test reaction for the catalytic properties of the hybrid materials **3**-**5**, the earlier studied aldol condensation reaction between benzaldehyde and MI (reaction 1) was chosen. For this reaction the ECE-pincer palladium(II) halide complexes can be used as such (see introduction).[21]

As a proof of principle, 250 mg of silica **5** which corresponds to 0.84 mol% of palladium loading was tested. Catalysis using 1.6 mmols of both benzaldehyde and MI was run to 30% conversion (Figure 7). At this stage stirring was stopped and a small part of the clear supernatant solution was removed and stirred separately. At the same time stirring of the remaining reaction mixture was continued. It was found that in the latter reaction mixture, catalysis in the presence of the hybrid material went further to completion, whereas the rate of the reaction in the sample of the supernatant had considerably slowed down and had become comparable to that of the blank reaction (Figure 7); i.e. that of a homogeneous reaction without added ECE-pincer Pd-complex. These observations indicate that the activity in the parent reaction and in the reaction mixture after sampling is associated with the catalytic activity of the (insoluble) hybrid material, i.e. with Pd-catalysis of the grafted PCP-catalyst, thereby demonstrating the true heterogeneous nature of the catalyst.

Next, the recyclability of hybrid material **5** as catalyst for reaction 1 was investigated. In this series of experiments, 500 mg of **5**, which corresponds to 1.67 mol% of

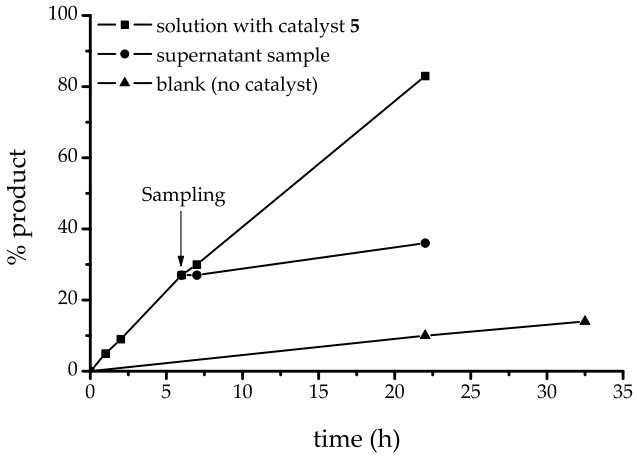


*Figure 7.* Kinetic traces of aldol reaction 1, showing catalysis only in presence of silica **5**; the supernatant sample (see text) shows the same kinetic trace as the blank.

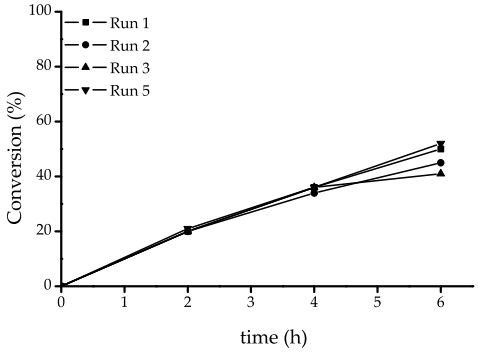


*Figure 8.* Consecutive use of silica **5** in reaction 1.

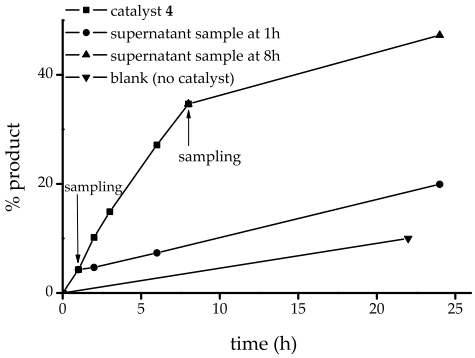


*Figure 9.* Aldol reaction 1 catalysed by silica **4**.

palladium loading, was used. Again 1.6 mmols of both benzaldehyde and MI were utilised. Work-up in between cycles involved centrifugation of the reaction mixture to separate the suspended silica and removal of the clear supernatant solution. The silica was washed twice with dichloromethane and then reused in the subsequent run. In total **5** consecutive runs were carried out. It was found that the activity of the catalyst was fully retained over these runs (Table 3, Figure 8). Comparison of the rate of the aldol reaction catalysed by homogeneous PCP-pincer palladium complex [PdCl(PCP)] with that of the hybrid material **5** showed that the homogeneous reaction (initial TOF 15 $h^{-1}$) was faster than the heterogeneous one (initial TOF 6 $h^{-1}$).

The supernatant reaction mixture for each of these runs was tested for palladium and silicon contents (Table 4). Some leaching of Pd on the ppm level was found but also the presence of Si was observed in the supernatant solutions. The amount of Si was larger as compared to that of Pd. This indicates that the origin of Pd is probably not the complex (which has a Pd/Si ratio of 1) but rather some small particles of silica itself that escaped separation from the solution. Moreover, the fact that the activity remained constant after each run indicated that leaching of the catalytic species during these experiments was negligible.

*Table 3.* Consecutive use of silica **5** in reaction 1.

| Run | % conversion after | | | | *trans* product |
|---|---|---|---|---|---|
| | 2h | 4h | 6h | 24h | (%) |
| 1 | 20 | 36 | 50 | - | 83 |
| 2 | 20 | 34 | 45 | - | 84 |
| 3 | 20 | 36 | 41 | 96 | 84 |
| 4 | - | - | - | 96 | 84 |
| 5 | 21 | 36 | 52 | 92 | 83 |

*Table 4.* Elemental analyses of supernatant aldol reaction mixtures catalysed by **5**.

| Sample | Pd | Si | Molar ratio |
|---|---|---|---|
| | (ppm) | (ppm) | Si/Pd |
| Run 1 | 348 | 856 | 9.3 |
| Run 2 | 126 | 969 | 29.1 |
| Run 3 | 144 | 728 | 19.1 |
| Run 4 | 96 | 113 | 4.5 |
| Run 5 | 115 | 447 | 14.7 |

TEM analyses carried out on a sample of **5** after run 1 and after run 5 indicated that the structure of the SBA-15 support was not damaged during catalysis. Furthermore, zerovalent palladium clusters were not observed in any of the investigated samples, i.e. no decomposition had occurred. EDX measurements confirmed that palladium and phosphor were present in the samples supporting the presence of the PCP-pincer Pd-complex. Further evidence for the integrity and stability of the hybrid material **5** after using it in aldol reaction 1 over 5 runs comes from solid-state $^{31}$P NMR, which showed a single peak at 42.3 ppm. This chemical shift corresponds to that of the P-centre in a cationic PCP-pincer Pd-complex with a coordinated isocyanide ligand instead of a chloride as the fourth ligand. This is consistent with our findings in case of the corresponding homogeneous complex, i.e. in a reaction of neutral [PdCl(PCP)] with MI, the $^{31}$P NMR resonance shifts from 31 ppm (neutral complex) to 42 ppm (cationic complex [Pd(PCP)(MI)]Cl).[21]

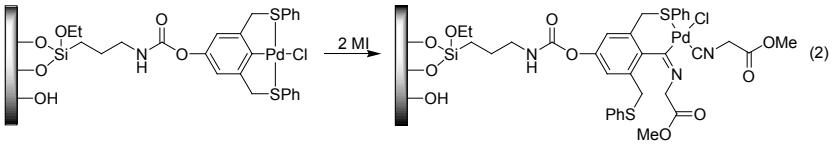


*Reaction 2.* Insertion complex formed upon reaction of SCS-pincer Pd-complex with isocyanide.

Hybrid material **4** (with the SCS-pincer palladium grouping) was found to behave in a similar manner as **5**. Similar experiments involving about 200 mg of silica **4** (0.48 mol% of palladium loading) confirmed that catalysis in the first run took place only because of the presence of **4** (Figure 9). However, upon recycling of **4**, a decreased activity was found. This is most likely due to catalyst deactivation and can be attributed to a low stability of the insertion complex that is formed upon reaction of SCS-pincer Pd-complex with an isocyanide (see reaction 2). Such insertion complexes are not formed in the case of PCP-pincer Pd-complexes[21] and, consequently, no deactivation is observed for hybrid materials derived from these complexes, i.e. for **3** and **5**. In the case of hybrid material **4**, a lower initial TOF of 11 $h^{-1}$ was observed whereas with its homogeneous counterpart SCS-pincer palladium complex [PdCl(SCS)] an initial TOF of 45 $h^{-1}$ was found.

## Conclusions

We have shown that ECE-pincer Pd-complexes were successfully immobilised on ordered mesoporous silicas. During immobilisation the integrity of both the organometallic moiety and the inorganic support remained unchanged. It was found that hybrid mesoporous material **5** derived from PCP-pincer palladium complex showed a good activity and recycling ability, whereas the corresponding hybrid

mesoporous material **4** with the SCS-pincer palladium complex, in spite of showing a similar initial activity in the first run, had a poor recycling ability. Likewise, a good initial activity together with a poor recycling ability was observed in the experiments with immobilised NCN-pincer palladium compounds.[18] It must be noted that both NCN- and SCS-pincer palladium complexes undergo a selective insertion reaction with MI, cf. reaction 2. As the corresponding PCP-pincer Pd-complex is not suffering from such an insertion reaction, the anchoring of this stable catalyst on a stable silica support like SBA-15 results in an excellent hybrid material **5**, which performs as a true heterogeneous catalyst and can be recycled and reused up to at least five times without loss of activity. Its decreased activity (TOF 6 $h^{-1}$) as compared to that of its homogeneous counterpart (TOF 15 $h^{-1}$) is quite acceptable for an immobilised catalyst. The fact that in consecutive catalysis runs the structure and integrity of both organometallic moiety and the inorganic support persisted, nicely meets the objective set to merge properties of a homogeneous and a heterogeneous catalytic system into one sustainable hybrid catalyst.

## Acknowledgements

Nilesh Mehendale is kindly thanked for grafting and catalysis experiments and valuable discussions. Prof. van Koten, Prof. Klein Gebbink and Dr. van Walree are thanked for their contributions as co-authors. The Dutch Technology Foundation STW and National Research School Combination Catalysis (NRSC-C) are acknowledged for financial support. Dr. Johan Hollander, and Dr. Kees Erkelens from University of Leiden are kindly thanked for the Solid-State NMR analysis. Finally, Hans Meeldijk is acknowledged for assistance with TEM analysis.

## References

1. Cornils, B., Herrmann, W. A.; *J. Catal.* **2003**, *216*, 23-31; Blaser, H.-U., Indolese, A., Schnyder, A., *Curr. Sci.* **2000**, *78*, 1336-1344.
2. McMorn, P., Hutchings, G. J., *Chem. Soc. Rev.* **2004**, *33*, 108-122; Dai, L.-X., *Angew. Chem. Int. Ed.* **2004**, *43*, 5726-5729; Quignard, F., Choplin, A., *Comprehensive Coordination Chemistry II* **2004**, *9*, 445-470; Cole-Hamilton, D. J., *Science* **2003**, *299*, 1702-1706; Hartley, F. R., *Supported Metal Complexes*, Kluwer Academic, Dordrecht, **1985**.
3. Thomas, J. M., Raja, R., *J. Organomet. Chem.* **2004**, *689*, 4110-4124.
4. Song, C. E., Lee, S.-G., *Chem. Rev.* **2002**, *102*, 3495-3524; Leadbeater, N. E., Marco, M., *Chem. Rev.* **2002**, *102*, 3217-3274; de Miguel, Y. R., Brulé, E., Margue, R. G., *J. Chem. Soc., Perkin Trans. 1* **2001**, *23*, 3085-3094; de Miguel, Y. R., *J. Chem. Soc., Perkin Trans. 1* **2000**, *24*, 4213-4221; Clark, J. H., Macquarrie, D. J., *Chem. Commun.* **1998**, 853-860; Choplin, A., Quignard, F., *Coord. Chem. Rev.* **1998**, *178-180*, 1679-1702; Brunel, D., Bellocq, N., Sutra, P., Cauvel, A., Laspéras, M., Moreau, P., Di Renzo, F., Anne, G., François, F.,

*Coord. Chem. Rev.* **1998**, *178-180*, 1085-1108.
5. Price, P. M., Clark, J. H., Macquarrie, D. J., *J. Chem. Soc., Dalton Trans.* **2000**, *2*, 101-110.
6. van der Boom, M. E., Milstein, D., *Chem. Rev.* **2003**, *103*, 1759-1792; Albrecht, M., van Koten, G., *Angew. Chem. Int. Ed.* **2001**, *40*, 3750-3781.
7. Szabo, K. J., *Synlett* **2006**, 811-824; Sebelius, S., Olsson, V. J., Szabo, K. J., *J. Am. Chem. Soc.* **2005**, *127*, 10478-10479; Kjellgren, J., Aydin, J., Wallner, O. A., Saltanova, I. V., Szabo, K. J., *Chem. Eur. J.* **2005**, *11*, 5260-5268; Kjellgren, J., Sunden, H., Szabo, K. J., *J. Am. Chem. Soc.* **2005**, *127*, 1787-1796; Wallner, O. A., Szabo, K. J., *J. Org. Chem.* **2005**, *70*, 9215-9221; Zhao, J., Goldman, A. S., Hartwig, J. F., *Science* **2005**, *307*, 1080-1082; Wallner, O. A., Szabo, K. J., *Org. Lett.* **2004**, *6*, 1829-1831; Solin, N., Kjellgren, J., Szabo, K. J., *J. Am. Chem. Soc.* **2004**, *126*, 7026-7033; Solin, N., Wallner, O. A., Szabo, K. J., *Org. Lett.* **2005**, *7*, 689-691; Kjellgren, J., Sunden, H., Szabo, K. J., *J. Am. Chem. Soc.* **2004**, *126*, 474-475; Takenaka, K., Uozumi, Y., *Org. Lett.* **2004**, *6*, 1833-1835; Fossey, J. S., Richards, C. J., *Organometallics* **2004**, **23**, 367-373; Wang, Z., Eberhard, M. R., Jensen, C. M., Matsukawa, S., Yamamoto, Y., *J. Organomet. Chem.* **2003**, *681*, 189-195; Diez-Barra, E., Guerra, J., Hornillos, V., Merino, S., Tejeda, J., *Organometallics* **2003**, *22*, 4610-4612; Singleton, J. T., *Tetrahedron* **2003**, *59*, 1837-1857; Rosa, G. R., Ebeling, G., Dupont, J., Monteiro, A. L., *Synthesis* **2003**, 2894-2897; Jung, I. G., Son, S. U., Park, K. H., Chung, K.-C., Lee, J. W., Chung, Y. K., *Organometallics* **2003**, *22*, 4715-4720; Fossey, J. S., Richards, C. J., *Tetrahedron Lett.* **2003**, *44*, 8773-8776; Sjoevall, S., Wendt, O. F., Andersson, C., *J. Chem. Soc., Dalton Trans.* **2002**, 1396-1400; Guillena, G., Rodriguez, G., van Koten, G., *Tetrahedron Lett.* **2002**, *43*, 3895-3898; Seul, J. M., Park, S., *J. Chem. Soc., Dalton Trans.* **2002**, 1153-1158; Morales-Morales, D., Cramer, R. E., Jensen, C. M., *J. Organomet. Chem.* **2002**, *654*, 44-50; Loch, J. A., Albrecht, M., Peris, E., Mata, J., Faller, J. W., Crabtree, R. H., *Organometallics* **2002**, *21*, 700-706; Williams, B. S., Dani, P., Lutz, M., Spek, A. L., van Koten, G., *Helv. Chim. Acta* **2001**, *84*, 3519-3530; Gruendemann, S., Albrecht, M., Loch, J. A., Faller, J. W., Crabtree, R. H., *Organometallics* **2001**, *20*, 5485-5488; Dupont, J., Pfeffer, M., Spencer, J., *Eur. J. Inorg. Chem.* **2001**, 1917-1927; Morales-Morales, D., Grause, C., Kasaoka, K., Redon, R., Cramer, R. E., Jensen, C. M., *Inorg. Chim. Acta* **2000**, *300-302*, 958-963; Morales-Morales, D., Redon, R., Yung, C., Jensen, C. M., *Chem. Commun.* **2000**, 1619-1620; Stark, M. A., Jones, G., Richards, C. J., *Organometallics* **2000**, *19*, 1282-1291; Gossage, R. A., Jastrzebski, J. T. B. H., van Ameijde, J., Mulders, S. J. E., Brouwer, A. J., Liskamp, R. M. J., van Koten, G., *Tetrahedron Lett.* **1999**, *40*, 1413-1416; Gossage, R. A., van de Kuil, L. A., van Koten, G., *Acc. Chem. Res.* **1998**, *31*, 423-431; Zhang, X., Longmire, J. M., Shang, M., *Organometallics* **1998**, *17*, 4374-4379; Ohff, M., Ohff, A., van der Boom, M. E., Milstein, D., *J. Am. Chem. Soc.* **1997**, *119*, 11687-11688; Denmark, S. E., Stavenger, R. A., Faucher, A.-M., Edwards, J. P., *J. Org. Chem.* **1997**, *62*, 3375-3389; Gorla, F., Togni, A., Venanzi, L. M., Albinati, A., Lianza, F., *Organometallics* **1994**, *13*, 1607-1616.
8. Rodriguez, G., Lutz, M., Spek, A. L., van Koten, G., *Chem. Eur. J.* **2002**, *8*, 45-57.
9. Schlenk, C., Kleij, A. W., Frey, H., van Koten, G., *Angew. Chem. Int. Ed.* **2000**, *39*, 3445-3447.
10. Bergbreiter, D. E., Osburn, P. L., Liu, Y.-S., *J. Am. Chem. Soc.* **1999**, *121*, 9531-9538.

11. Slagt, M. Q., Stiriba, S.-E., Kautz, H., Klein Gebbink, R. J. M., Frey, H., van Koten, G., *Organometallics* **2004**, *23*, 1525-1532; Slagt, M. Q., Stiriba, S.-E., Klein Gebbink, R. J. M., Kautz, H., Frey, H., van Koten, G., *Macromolecules* **2002**, *35*, 5734-5737; Kleij, A. W., Gossage, R. A., Jastrzebski, J. T. B. H., Boersma, J., van Koten, G., *Angew. Chem. Int. Ed.* **2000**, *39*, 176-178.
12. Bergbreiter, D. E., Furyk, S., *Green Chem.* **2004**, *6*, 280-285.
13. Suijkerbuijk, B. M. J. M., Shu, L., Klein Gebbink, R. J. M., Schlueter, A. D., van Koten, G., *Organometallics* **2003**, *22*, 4175-4177.
14. Slagt, M. Q., Jastrzebski, J. T. B. H., Klein Gebbink, R. J. M., van Ramesdonk, H. J., Verhoeven, J. W., Ellis, D. D., Spek, A. L., van Koten, G., *Eur. J. Org. Chem.* **2003**, 1692-1703; Kleij, A. W., Klein Gebbink, R. J. M., van den Nieuwenhuijzen, P. A. J., Kooijman, H., Lutz, M., Spek, A. L., van Koten, G., *Organometallics* **2001**, *20*, 634-647; Kleij, A. W., Gossage, R. A., Klein Gebbink, R. J. M., Brinkmann, N., Reijerse, E. J., Kragl, U., Lutz, M., Spek, A. L., van Koten, G., *J. Am. Chem. Soc.* **2000**, *122*, 12112-12124.
15. Dijkstra, H. P., Kruithof, C. A., Ronde, N., van de Coevering, R., Ramon, D. J., Vogt, D., van Klink, G. P. M., van Koten, G., *J. Org. Chem.* **2003**, *68*, 675-685; Dijkstra, H. P., Ronde, N., van Klink, G. P. M., Vogt, D., van Koten, G., *Adv. Synth. Catal.* **2003**, *345*, 364-369; Dijkstra, H. P., van Klink, G. P. M., van Koten, G., *Acc. Chem. Res.* **2002**, *35*, 798-810.
16. van de Coevering, R., Alfers, A. P., Meeldijk, J. D., Martinez-Viviente, E., Pregosin, P. S., Klein Gebbink, R. J. M., van Koten, G., *J. Am. Chem. Soc.* **2006**, *128*, 12700-12713; van de Coevering, R., Kuil, M., Klein Gebbink, R. J. M., van Koten, G., *Chem. Commun.* **2002**, 1636-1637.
17. Bergbreiter, D. E., *Chem. Rev.* **2002**, *102*, 3345-3384; Bergbreiter, D. E., Osburn, P. L., Frels, J. D., *J. Am. Chem. Soc.* **2001**, *123*, 11105-11106.
18. Mehendale, N. C., Bezemer, C., van Walree, C. A., Klein Gebbink, R. J. M., van Koten, G., *J. Mol. Catal. A* **2006**, *257*, 167-175.
19. Gimenez, R., Swager, T. M., *J. Mol. Catal. A* **2001**, *166*, 265-273.
20. Yu, K., Sommer, W., Richardson, J. M., Weck, M., Jones, C. W., *Adv. Synth. Catal.* **2005**, *347*, 161-171; Sommer, W., Yu, K., Sears, J. S., Ji, Y., Zheng, X., Davis, R. J., Sherrill, C. D., Jones, C. W., Weck, M., *Organometallics* **2005**, *24*, 4351-4361; Yu, K., Sommer, W., Weck, M., Jones, C. W., *J. Catal.* **2004**, *226*, 101-110; Chanthateyanonth, R., Alper, H., *Adv. Synth. Catal.* **2004**, *346*, 1375-1384; Chanthateyanonth, R., Alper, H., *J. Mol. Catal. A* **2003**, *201*, 23-31.
21. Mehendale, N. C., Havenith, R. W. A., Lutz, M., Spek, A. L., Klein Gebbink, R. J. M., van Koten, G., *manuscript in prep.*
22. Mehendale, N. C., Lutz, M., Spek, A. L., Klein Gebbink, R. J. M., van Koten, G., *manuscript in prep.*
23. Mehendale, N. C., Lutz, M., Spek, A. L., Klein Gebbink, R. J. M., van Koten, G., *manuscript in prep.*
24. Kresge, C. T., Leonowicz, M. E., Roth, W. J., Vartuli, J. C., Beck, J. S., *Nature* **1992**, *359*, 710-712.
25. Zhao, D., Feng, J., Huo, Q., Melosh, N., Fredrickson, G. H., Chmelka, B. F., Stucky, G. D., *Science* **1998**, *279*, 548-552.
26. Sietsma, J. R. A., Meeldijk, J. D., Den Breejen, J. P., Versluijs-Helder, M., Van Dillen, A. J., De Jongh, P. E., De Jong, K. P., *Angew. Chem. Int. Ed.* **2007**, *46*, 4547-4549; Sakthivel, A., Zhao, J., Hanzlik, M., Chiang, A. S. T.,

Herrmann, W. A., Kuehn, F. E., *Adv. Synth. Catal.* **2005**, *347*, 473-483; Raj, N. K. K., Deshpande, S. S., Ingle, R. H., Raja, T., Manikandan, P., *Catal. Lett.* **2004**, *98*, 217-224; Ayala, V., Corma, A., Iglesias, M., Sanchez, F., *J. Mol. Catal. A* **2004**, *221*, 201-208; Nguyen, J. V., Jones, C. W., *Macromolecules* **2004**, *37*, 1190-1203; Ma, H., He, J., Evans, D. G., Duan, X., *J. Mol. Catal. B* **2004**, *30*, 209-217; González-Arellano, C., Corma, A., Iglesias, M., Sánchez, F., *Adv. Synth. Catal.* **2004**, *346*, 1316-1328; Liu, P. N., Gu, P. M., Wang, F., Tu, Y. Q., *Org. Lett.* **2004**, *6*, 169-172; Stepnicka, P., Demel, J., Cejka, J., *J. Mol. Catal. A* **2004**, *224*, 161-169; Kim, J.-H., Kim, G.-J., *Catal. Lett.* **2004**, *92*, 123-130.

27. Maschmeyer, T., Rey, F., Sankar, G., Thomas, J. M., *Nature* **1995**, *378*, 159-162.
28. Jaroniec, M.; Kruk, M.; Olivier, J.P.; Koch, S. *Stud. Surf. Sci. Catal.* **2000**, *128*, 71-80.
29. Lippens, B.C.; De Boer, J.H. *J. Catal.* **1965**, *4*, 319-323.
30. McKittrick, M. W., Jones, C. W., *J. Catal.* **2004**, *227*, 186-201.

# 8

# Summary and concluding remarks

Catalysts are indispensable to modern-day society because of their prominent role in petroleum refining, bulk and fine chemical processing, and reduction of environmental pollution. The catalytically active component usually consists of small metal (oxide) particles. High surface-to-volume ratios are often important for these particles since catalytic processes take place at the surface. Therefore, supports such as $SiO_2$ and $\gamma$-$Al_2O_3$ are generally used to obtain small and thermally stable particles. The most widely used method to obtain supported catalysts is based on impregnation of the support with a precursor-containing solution, followed by drying. Subsequent thermal treatment in air, referred to as calcination, is applied to convert the precursor into the respective metal oxide, or metal in question when followed by high-temperature reduction.

The choice of precursor and type of experimental conditions applied during each step in the preparation largely affect the final dispersion of the metal (oxide) particles. Hence, fundamental understanding of the involved physico-chemical processes is a prerequisite for improving the performance of catalysts. However, fundamental studies are often hampered by the heterogeneity of conventional supports that make it difficult to disentangle the effects of the individual preparation steps on the final dispersion. To overcome these problems, we decided to employ ordered mesoporous SBA-15 as model support system. Because of the hexagonal arrangement of pores with uniform sizes, detailed information on the size and distribution of active phase or its precursor possibly could be obtained with electron microscopy and $N_2$-physisorption. Hence, the work described in this thesis concentrated on gaining insight on the impact of each step in the preparation on the final dispersion of the active component and the implications thereof for catalysis. As Ni and Co are amongst the most widely applied metals in catalysis and preparation of these catalysts using metal nitrate precursors is attractive, but generally cumbersome as low metal dispersions are obtained, we took up the challenging task to address this problem.

In **chapter 2** we described the results obtained for our study of the impregnation and drying of ordered mesoporous supports. It has been observed that ordered mesoporous supported metal (oxide) catalysts prepared by the impregnation and drying method displayed a non-uniform filling of the pores with the active component. Our research was carried out using SBA-15 and aqueous $[Ni(OH_2)_6](NO_3)_2$ precursor solution. With cryo-HAADF-STEM the distribution of precursor solution inside the pores was imaged and, it was shown that the non-uniform filling of pores originates from the impregnation step as many empty pores were observed. In addition, precursor solution was found at the exterior of the support particles. It was argued that this is associated with inadequate contact between precursor solution and all the pore mouths, which might be related to the relatively low hydroxyl density of ordered mesoporous supports. Investigation of the drying step showed that the non-uniform filling of the pores with precursor was retained, but precursor was no longer found outside the pores. The formed $Ni_3(NO_3)_2(OH)_4$ precursor had an average crystal size of 9 nm, which was in good agreement with the pore diameter

(9 nm) and suggested confinement. We propose that the absence of large precursor particles outside of the mesopores was due to transport of extra-porous precursor into the filled pores upon drying, resulting in an increase of the amount of species inside these pores. It was demonstrated that based on the proposed mechanism, filling of virtually all the pores could be accomplished by offering a volume of precursor solution to SBA-15 that was more than twice the pore volume without the formation of large precursor particles outside the mesopores after drying.

In **chapter 3** we looked into the cause of the poor final metal dispersion of $Ni/SiO_2$ *ex* nitrate catalysts when prepared by impregnation and drying. The thermal treatments usually applied to bring about the Ni metal phase were investigated in detail using SBA-15 support and starting from a dried impregnate that contained exclusively well-dispersed $Ni_3(NO_3)_2(OH)_4$ crystals of 9 nm inside the pores. It turned out that calcination in air was the most detrimental treatment as severe sintering and redistribution took place, resulting in large NiO particles outside the pores and confined rodlike NiO particles with a diameter of 9 nm inside the pores. The degree of sintering and redistribution showed to depend on the partial pressure of the gaseous $NO_2$, $N_2O$, $H_2O$ and $O_2$ decomposition products. High concentrations of in particular $NO_2/O_2$ showed to favour migration out of the pores resulting in large NiO particles up to 90 nm in size at the exterior of the SBA-15 support particles. Using an $H_2$-containing gas atmosphere it was demonstrated that when formation of $NO_2/O_2$ is prevented, no sintering and redistribution took place. Moreover, we showed that the decomposition of $Ni_3(NO_3)_2(OH)_4$ in the presence of $H_2$ was moderated and yielded NiO prior to the formation of Ni metal. Hence, it was proposed that the beneficial role of $H_2$ relates to its impact on the decomposition of the nitrate precursor and consequently the type of gaseous products formed rather than direct reduction of the nitrate into Ni metal phase.

In **chapter 4** it was shown that thermal decomposition of supported nitrate impregnate in a diluted stream of NO prevented sintering and redistribution. NiO and $Co_3O_4$ particles of 3 to 5 nm were obtained at loadings op to 37 and 23 wt%, respectively, depending on the type of support used. This new thermal treatment demonstrated to be applicable to both ordered mesoporous silica support and conventional silica gel. Moreover, similar results were obtained with carbon nanofibers supports, which demonstrated the versatility of the method. The concentration of NO needed to obtain highly dispersed NiO on $SiO_2$ at a loading of 24 wt% depended on the gas-hourly-space-velocity (GHSV). When a high GHSV of 24,500 $h^{-1}$ was applied, a NO concentration of 0.1 vol% in He did suffice. By increasing the amount of NO to 1 vol%, the GHSV could be lowered to 6,800 $h^{-1}$ without loss of dispersion and also at lower GHSV values the NiO crystals were smaller than obtained with pure He. Finally, catalytic testing of silica gel supported Ni metal catalysts in the hydrogenation of soybean oil showed that the NO/He treatment led to a more active catalyst as the required hydrogenation time was reduced by 30% compared to the catalyst prepared via traditional calcination in an air flow.

The research in **chapter 5** was conducted to propose an explanation for the role

of NO/He flow in preventing sintering and redistribution as observed in air flow and in He flow. Firstly, the impact of each gas atmosphere on the morphology of the NiO particles formed inside the pores of SBA-15 was addressed. The combination of electron tomography, $N_2$-physisorption and XRD provided structural insight into the NiO phase inside the pores. The use of air and pure He flows resulted primarily in the formation of rodlike NiO particles with a diameter similar to that of the pores (9 nm). However, in the He treated sample pores containing smaller NiO particles were identified too. The NO/He atmosphere led to exclusive formation of well-distributed NiO particles in the filled pores with a volume weighted maximum of 4 nm. Secondly, it was shown that NO/He moderated the rate of decomposition resulting in more gradual evolvement of $NO_2$, $N_2O$ and $H_2O$ gaseous products and the $Ni_3(NO_3)_2(OH)_4$ decomposition rate was much lower than in air. In situ XRD showed that$Ni_3(NO_3)_2(OH)_4$ decomposition in NO/He followed zero-order kinetics, whereas in air an 'auto-catalytic' type of decomposition was observed. DSC results indicated that decomposition in NO/He was less endothermic and proceeded over a much wider temperature range than in air. It was proposed that this might be related to the exothermic scavenging of oxygen radicals emerging from the nitrate decomposition by NO. This hypothesis was in line with MS results that indicated that $O_2$ was not present amongst the gaseous decomposition products when $Ni_3(NO_3)_2(OH)_4$ was decomposed in NO/He contrarily to treatment in inert atmosphere. Based on these results and those obtained in chapter 3 it was concluded that thermal decomposition of supported nickel nitrate in a gas atmosphere containing an oxygen scavenger such as NO, $H_2$, $N_2O$ or CO is crucial for obtaining small NiO particles.

It was demonstrated in chapter 4 that silica gel supported $Co_3O_4$ particles of 3 to 5 nm at a Co metal loading of 18 wt% could be obtained with the NO/He method. Hence, in **chapter 6** the promising properties of the catalyst obtained after high-temperature reduction in the Fischer-Tropsch synthesis were investigated. The results that were described in this chapter dealt with catalytic results of the 18 wt% Co metal on silica gel in which the nitrate decomposition step into $Co_3O_4$ was done in air flow, in $H_2$/He flow or in NO/He flow. It was shown that the activity of catalysts that were prepared using the NO/He treatment was more than a factor of two higher than that of the air treated ones. The activity of the catalyst prepared using $H_2$/He treatment was even lower than the air calcined catalysts. The latter finding might be explained by formation of relatively large quantities of Co phyllosilicates instead of Co metal. Although the NO/He treated catalyst displayed a high activity, the catalyst required a reduction temperature of 550 °C to obtain the maximum activity, supposedly due to the more difficult reduction of highly dispersed $Co_3O_4$ particles. Adding 0.05 wt% of Pt reduction promoter to the catalyst allowed lowering of the reduction temperature to 450 °C without significant loss of activity. The $C_{5+}$ selectivity of the NO/He treated catalysts was lower than that of the air calcined ones. This could be explained by literature observations that reported a decrease in $C_{5+}$ selectivity upon increase of the Co metal dispersion. Moreover, the higher $C_{5+}$ selectivity of the air calcined catalysts could be related to the breaking-up of the relatively large

$Co_3O_4$ particles into Co metal during reduction, which recently has been reported to improve the $C_{5+}$ selectivity.

Finally, the results described in **chapter 7** showed that ordered mesoporous silicas MCM-41 and SBA-15 are interesting host materials for homogeneous PCP and SCS-pincer Pd-complexes. The complexes were covalently attached to the support via a trialkoxysilane moiety without causing significant damage to the ordered structure of the supports. The catalytic activity of the immobilised complexes was tested in the aldol condensation reaction between methyl isocyanoacetate and benzaldehyde. It was demonstrated that the SBA-15 supported PCP-pincer Pd-catalyst showed stability up to 5 runs. Control experiments demonstrated the true heterogeneous nature of this catalyst and hence the successful immobilisation of the homogeneous pincer catalyst.

# Samenvatting en conclusies

Een katalysator is een stof die een chemische omzetting versnelt door het verlagen van de activeringsenergie zonder daarbij substantieel te worden verbruikt. Katalysatoren vervullen een belangrijke rol in de raffinage van aardolie, de productie van chemicaliën en de vermindering van de uitstoot van milieuonvriendelijke stoffen. De katalytisch actieve fase bestaat veelal uit metaal(oxide) deeltjes. Aangezien katalyse plaatsvindt aan het oppervlak van deze deeltjes is het doorgaans belangrijk dat de deeltjes klein zijn om een hoog specifiek oppervlak te creëren, ofwel een hoge dispersie te bereiken. Om deze kleine deeltjes thermisch stabiel te maken wordt gebruik gemaakt van dragermaterialen zoals $SiO_2$ en $Al_2O_3$. De meest gebruikte manier om gedragen metaal(oxide)-katalysatoren te verkrijgen is gebaseerd op het impregneren van de drager met een waterige oplossing van een metaalzout, gevolgd door een droogstap om depositie van het zout op de drager te bewerkstelligen. Vervolgens wordt het metaalzout via thermische ontleding omgezet in het gewenste metaaloxide door het gedroogde product te verhitten in lucht tot hoge temperaturen (300 tot 500 °C), hetgeen calcineren genoemd wordt. Indien het metaal de actieve component is wordt deze stap gevolgd door een reductiestap bij hoge temperatuur met waterstof ($H_2$).

Het type metaalzout, dat gebruikt wordt als precursor voor het metaal(oxide), bepaalt tezamen met de experimentele condities waaronder elke bereidingsstap wordt uitgevoerd, in grote mate de uiteindelijke dispersie van de actieve fase en zijn verdeling over het oppervlak van de drager. Het is dan ook belangrijk inzicht te verkrijgen in het effect van de fysisch-chemische processen die plaatsvinden tijdens elke bereidingsstap op de uiteindelijke werking van de katalysator. Fundamentele studies hiernaar worden veelal gehinderd door de relatief slecht gedefinieerde eigenschappen van conventionele dragermaterialen die het bestuderen van het materiaal verkregen na elke bereidingsstap bemoeilijken. Door gebruik te maken van geordend mesoporeuze dragers als modelsystemen kunnen deze problemen grotendeels voorkomen worden. In het onderzoek beschreven in dit proefschrift is er voornamelijk gebruik gemaakt van geordend mesoporeus silica met als aanduiding SBA-15. SBA-15 bevat uniforme poriën die geordend zijn in een honingraatstructuur waardoor er met gebruik van elektronenmicroscopie en $N_2$-fysisorptie veel informatie verkregen kan worden over de grootte en locatie van de actieve fase of zijn precursor na elke bereidingsstap.

Gedragen nikkel- en kobalt-katalysatoren behoren tot de meest gebruikte in de katalyse en de bereiding van deze katalysatoren via nitraatzouten biedt veel voordelen aangezien hoge beladingen bereikt kunnen worden door hun goede oplosbaarheid in water en de thermische ontleding ervan zuivere metaaloxides opleveren. Helaas worden de aldus verkregen katalysatoren veelal gekenmerkt door lage metaal(oxide) dispersies. Het onderzoek beschreven in dit proefschrift heeft zich voornamelijk gericht op het gebruik van SBA-15 als modelsysteem om inzicht te verkrijgen in de redenen hiervoor.

Een veel voorkomende bijkomstigheid van het gebruik van geordend mesoporeuze dragers zoals MCM-41 en SBA-15 is dat niet al de poriën gevuld zijn met

metaal(oxide) wanneer de techniek van impregneren en drogen gebruikt wordt. In **hoofdstuk 2** zijn de resultaten van het onderzoek beschreven dat is uitgevoerd om dit fenomeen te bestuderen. Het onderzoek is verricht door gebruik te maken van SBA-15 en een waterige oplossing van nikkelnitraat. Cryo-HAADF-STEM karakterisering van het product verkregen na impregneren liet zien dat de verdeling van de precursoroplossing niet uniform was over alle poriën en velen bleken niet (volledig) gevuld te zijn. Daarnaast werden er ook aanwijzingen gevonden dat er precursoroplossing buiten de poriën aanwezig was. Het incompleet vullen van alle poriën heeft waarschijnlijk te maken met het niet bevochtigen van alle poriemonden en houdt mogelijk verband met het relatief hydrofobe karakter van SBA-15 door de betrekkelijk lage dichtheid van silanolgroepen. Uit het bestuderen van de droogstap werd duidelijk dat tijdens drogen bij 120 °C nikkelnitraathydroxide ($Ni_3(NO_3)_2(OH)_4$) uitsluitend in de poriën aanwezig was met een gemiddelde kristallietgrootte van 9 nanometer (nm). De overeenkomst tussen de kristallietgrootte en de diameter van de mesoporiën (9 nm) doet vermoeden dat de $Ni_3(NO_3)_2(OH)_4$ fase beperkt werd in grootte tijdens de groei. Na drogen werden er geen $Ni_3(NO_3)_2(OH)_4$ deeltjes op het buitenoppervlak van de SBA-15 dragerdeeltjes gevonden hetgeen verklaard kan worden door transport van nikkelnitraat precursor dat aanwezig was op het buitenoppervlak in poriën waarmee de precursor in contact stond tijdens het drogen. Resultaten behaald met een impregnatie waarbij ruim meer nikkelnitraat oplossing werd geïmpregneerd dan het porievolume van SBA-15 bevestigden deze hypothese. Na drogen bleef de $Ni_3(NO_3)_2(OH)_4$ kristallietgrootte namelijk onveranderd en werd er eveneens geen $Ni_3(NO_3)_2(OH)_4$ gevonden buiten de mesoporiën.

Het onderzoek dat is beschreven in **hoofdstuk 3** behandelt de lage nikkeldispersie die over het algemeen verkregen wordt bij de bereiding van $Ni/SiO_2$ katalysatoren met gebruik van een waterige impregnatieoplossing van nikkelnitraat. Als uitgangspunt werd gebruik gemaakt van een geïmpregneerd en gedroogd preparaat van $Ni_3(NO_3)_2(OH)_4$/SBA-15 waarbij precursor uitsluitend in de mesoporiën aanwezig was. De resultaten lieten zien dat de thermische ontleding van de nitraatprecursor in lucht om nikkeloxide (NiO) te verkrijgen gepaard gaat met sinteren en transport uit de poriën wat resulteerde in grote NiO-deeltjes op het buitenoppervlak van de deeltjes van SBA-15 en cylindervormige NiO-deeltjes in de mesoporiën. De mate van precursortransport tijdens ontleding van het nitraat bleek afhankelijk te zijn van de concentratie van de $NO_2$, $N_2O$, $H_2O$ en $O_2$ gassen die vrijkomen tijdens de nitraatontleding. Hoge concentraties van in het bijzonder $NO_2/O_2$ bleek migratie van precursor uit de poriën naar het buitenoppervlak te bevorderen resulterend in NiO-deeltjes met groottes tot 90 nm. Door de thermische ontleding uit te voeren in aanwezigheid van $H_2$ werd de vorming van $NO_2/O_2$ ontledingsproducten voorkomen en werd er geen precursormigratie uit de poriën waargenomen. De resultaten lieten zien dat $H_2$ de ontleding van $Ni_3(NO_3)_2(OH)_4$ in NiO langzamer doet verlopen en er na de vorming van NiO pas metallisch nikkel ontstaat. Het wordt dan ook voorgesteld dat de rol van $H_2$ gerelateerd is aan het direct beïnvloeden van de ontleding van het nitraat, resulterend in een verandering van de type ontledingsproducten die

gevormd worden en niet gerelateerd is aan de directe reductie van het nitraat tot metallisch nikkel.

**Hoofdstuk 4** laat zien dat thermische ontleding van gedragen $Ni_3(NO_3)_2(OH)_4$ in een NO bevattende inerte (He) atmosfeer in plaats van in lucht sinteren en migratie van de precursor voorkomt en de bereiding van NiO deeltjes van 3 tot 5 nm mogelijk maakt bij een gewichtsbelading van 37%. Deze methode bleek geschikt te zijn voor zowel meerdere overgangsmetalen (Ni, Co en wellicht Fe en Cu) als meerdere dragermaterialen, te weten geordend mesoporeuze silica, conventionele silicagel en koolstofnanovezels. De hoeveelheid NO die nodig is om kleine NiO deeltjes te verkrijgen bij een belading van 24 gewichtsprocent NiO is afhankelijk van de verversingssnelheid van het reactorbed tijdens de NO/He behandeling, ofwel de gas-hourly-space-velocity (GHSV). Bij een belading van 24 gewichtsprocent NiO en een GHSV van 24.500 $h^{-1}$ bleek een NO concentratie van 0.1 volumeprocent voldoende te zijn terwijl bij een NO concentratie van 1 volumeprocent een GHSV van 6,800 $h^{-1}$ genoeg was. Ook bij lagere waarden van de GHSV leverde het gebruik van een concentratie van 1 volumeprocent NO/He kleinere NiO kristallen dan met zuiver He verkregen werd. Tenslotte werd de invloed van de NO/He methode op de uiteindelijke werking van de $Ni/SiO_2$ katalysatoren onderzocht door de activiteit in de hydrogenatie van sojaolie van de NO/He behandelde katalysatoren te vergelijken met die van katalysatoren bereidt via calcineren in lucht. De resultaten lieten zien dat gebruik van de NO/He methode resulteerde in veel actievere katalysator aangezien de benodigde tijd voor hydrogenatie afnam met 30%.

Het onderzoek beschreven in **hoofdstuk 5** is uitgevoerd om een verklaring te vinden voor de rol van NO op het voorkomen van sinteren en migreren van precursor tijdens de thermische ontleding van nikkelnitraat zoals waargenomen in lucht en He. Allereerst is de invloed van de gasatmosfeer op de uiteindelijke morfologie van de verkregen NiO-deeltjes onderzocht. Door elektronentomografie te combineren met $N_2$-fysisorptie en poederdiffractie werd er inzicht verkregen in de structuur van de NiO-deeltjes aanwezig in de mesoporiën van SBA-15. In lucht en He werden voornamelijk cylindrische NiO-deeltjes gevormd met een diameter gelijk aan die van de mesoporiën (9 nm). In het in He behandelde preparaat werden ook poriën gevonden die kleinere deeltjes bevatten. In de poriën van het preparaat, verkregen na de NO/He methode, werden uitsluitend kleine en homogeen verdeelde NiO deeltjes met een volumegewogen gemiddelde grootte van 4 nm gevonden. Verder liet het onderzoek zien dat NO/He de ontledingssnelheid van het $Ni_3(NO_3)_2(OH)_4$ in NiO verlaagt, resulterend in een meer geleidelijke vorming van $NO_2$, $N_2O$ en $H_2O$. *In situ* poederdiffractie experimenten lieten zien dat de ontleding van $Ni_3(NO_3)_2(OH)_4$ in NO/He een nulde orde kinetiek volgde terwijl de kinetiek in lucht autokatalytisch bleek te zijn. Differentiële Scanning Calorimetrie (DSC) resultaten demonstreerden dat de ontleding in NO/He meer endotherm is dan in lucht. Het wordt dan ook betoogd dat dit gerelateerd is aan de exotherme interactie van NO met zuurstofatomen van het nitraat. Deze hypothese wordt ondersteund door massaspectrometrie resultaten die lieten zien dat $O_2$ niet als ontledingsproduct

gedetecteerd werd wanneer de ontleding in NO/He uitgevoerd werd. Op basis van deze resultaten en die beschreven in hoofdstuk 3 is er dan ook geconcludeerd dat de aanwezigheid van gassen die interactie aan kunnen gaan met zuurstofatomen, zoals NO, $H_2$, $N_2O$ en CO, tijdens thermische ontleding van gedragen nikkelnitraat voordelig is voor het verkrijgen van kleine NiO deeltjes.

De resultaten uit hoofdstuk 4 demonstreerden dat via de NO/He methode silica gedragen $Co_3O_4$ deeltjes van 3 tot 5 nm met een 18% gewichtsbelading kobaltmetaal (Co) verkregen kunnen worden. In **hoofdstuk 6** zijn de eigenschappen van deze katalysator (na *in situ* reductie tot Co) in de Fischer-Tropschsynthese onderzocht en vergeleken met katalysatoren waarbij de nitraatontledingsstap uitgevoerd werd in lucht of $H_2$/He gas. De activiteit van de katalysator verkregen via de NO/He methode bleek meer dan een factor twee hoger dan die van de in lucht behandelde katalysatoren. De activiteit van de in $H_2$/He behandelde katalysator was het laagst van allen hetgeen mogelijk verklaard kan worden door de vorming van relatief grote hoeveelheden (inactief) kobaltsilicaat in plaats van metallisch kobalt tijdens de nitraatontledingsstap. De resultaten lieten zien dat de maximale activiteit van de katalysator verworven via de NO/He methode verkregen werd na reductie bij 550 °C. Het wordt betoogd dat dit het gevolg is van de hoge $Co_3O_4$ dispersie van deze katalysator. Na toevoegen van 0.05 gewichtsprocent Pt reductiepromoter aan de katalysator kon de reductietemperatuur met 100 °C verlaagd worden naar 450 °C. Productanalyse demonstreerde dat de $C_{5+}$-selectiviteit van de in NO/He geprepareerde katalysatoren lager was dan die van de in lucht gecalcineerde katalysator. Dit kan verklaard worden door gerapporteerde waarnemingen dat de $C_{5+}$-selectiviteit afneemt bij een toename van de Co-dispersie. Bovendien kan de hogere $C_{5+}$-selectiviteit van de in lucht gecalcineerde katalysatoren gerelateerd zijn aan de vorming van clusters van deeltjes door het opbreken van de relatief grote $Co_3O_4$ deeltjes in kleinere Co-deeltjes tijdens reductie zoals recentelijk is gerapporteerd.

Tenslotte laten de resultaten in **hoofdstuk 7** zien dat geordend mesoporeuze materialen MCM-41 en SBA-15 goede dragers zijn om homogene PCP en SCS-tang palladiumcomplexen te immobiliseren. In dit onderzoek werden de complexen covalent gebonden aan de drager door gebruik te maken van trialkylsilaan-gefunctionaliseerde moleculen. Het werd gedemonstreerd dat het SBA-15 gedragen PCP-tang palladiumcomplex stabiliteit vertoonde tijdens minstens 5 katalytische testen zonder verlies van activiteit. Controle experimenten bevestigden de heterogene aard van de katalysator in deze reactie.

# List of Publications and Presentations

**Patent applications**

*Modified Heat Treatment of Impregnated Metal Nitrate Catalysts*
J.R.A. Sietsma, A.J. van Dillen, P.E. de Jongh and K.P. de Jong, GB0617529.3 **2006**.

*Metal Nitrate Conversion Method*
J.R.A. Sietsma, A.J. van Dillen, P.E. de Jongh and K.P. de Jong, WO 2007/071899 **2007**.

**Publications**

*Application of Ordered Mesoporous Materials as Model Supports to Study Catalyst Preparation by Impregnation and Drying*
J.R.A. Sietsma, A.J. van Dillen, P.E. de Jongh and K.P. de Jong, *Stud. Surf. Sci. Catal.* **2006**, *162*, 95-102.

*Preparation of Supported NiO and $Co_3O_4$ Nanoparticles by Controlled Thermal Decomposition of Nitrates using NO*
J.R.A. Sietsma, J.D. Meeldijk, J.P. den Breejen, M. Versluijs-Helder, A.J. van Dillen, P.E. de Jongh and K.P. de Jong, *Angew. Chem. Int. Ed.* **2007**, *46*, 4547-4549.

*Highly Active Cobalt-on-Silica Catalysts for the Fischer-Tropsch Synthesis obtained via a Novel Calcination Procedure*
J.R.A. Sietsma, J.P. den Breejen, P.E. de Jongh, A.J. van Dillen, J.H. Bitter and K.P. de Jong, *Stud. Surf. Sci. Catal.* **2007**, *167*, 55-60.

*Measuring Location, Size, Distribution and Loading of NiO Crystallites in Individual SBA-15 Pores by Electron Tomography*
H. Friedrich, J.R.A. Sietsma, P.E. de Jongh and K.P. de Jong, *J. Am. Chem. Soc.* **2007**, *129*, 10249-10254.

*How Nitric Oxide Affects the Thermal Decomposition of Nickel Nitrate to Form Uniform NiO Nanoparticles*
J.R.A. Sietsma, H. Friedrich, A. Broersma, M. Versluijs-Helder, A.J. van Dillen, P.E. de Jongh and K.P. de Jong, **2007**, *submitted.*

*Ordered Mesoporous Silica to Study the Preparation of $Ni/SiO_2$ ex Nitrate Catalysts: Impregnation, Drying and Thermal Treatments*
J.R.A. Sietsma, J.H. Meeldijk, M. Versluijs-Helder, A. Broersma, A.J. van Dillen, P.E. de Jongh and K.P. de Jong, **2007**, *submitted*.

*PCP- and SCS-Pincer Palladium Complexes Immobilized on Mesoporous Silica: Application in C–C Bond Formation Reactions*
N.C. Mehendale, J.R.A. Sietsma, K.P. de Jong, C.A. van Walree, R.J.M. Klein Gebbink and G. van Koten, **2007**, *submitted.*

**Oral presentations**

*Fundamental Study on Catalyst Preparation using Mesoporous Support Materials*
J.R.A. Sietsma, A.J. van Dillen and K.P. de Jong
Annual meeting of the section Powder Diffraction of the Nederlandse Vereniging voor Kristallografie
Leiden, the Netherlands, December 2004

*Fundamental Study on Catalyst Preparation using SBA-15 as Model Support System*
J.R.A. Sietsma, A.J. van Dillen and K.P. de Jong
Netherlands' Catalysis and Chemistry Conference
Noordwijkerhout, the Netherlands, March 2005

*Application of Ordered Mesoporous Supports as Model Systems for Studying the Effects of Catalyst Preparation on the Ultimate Metal Particle Size*
J.R.A. Sietsma, P.E. de Jongh, A.J. van Dillen and K.P. de Jong
European Materials Research Society Meeting
Warsaw, Poland, September 2006

*Ordered Mesoporous Supports as Model Systems for Studying Catalyst Preparation*
J.R.A. Sietsma, H. Friedrich, P.E. de Jongh, A.J. van Dillen and K.P. de Jong
9th International Symposium on Scientific Bases for the Preparation of Heterogeneous Catalysts
Louvain-la-Neuve, Belgium, September 2006

*Ordered Mesoporous Supports as Model Systems for Studying Catalyst Preparation: on the Preparation of Highly Dispersed Cobalt and Nickel on Silica Catalysts using Nitrates as Precursor Salts*
J.R.A. Sietsma, H. Friedrich, P.E. de Jongh, A.J. van Dillen and K.P. de Jong
4th Asia Pacific Congress on Catalysis
Singapore, December 2006

*Ordered Mesoporous Supports as Model Systems for Studying the Preparation of Cobalt and Nickel Catalysts by Impregnation and Drying*
J.R.A. Sietsma, H. Friedrich, J.P. den Breejen, P.E. de Jongh, A.J. van Dillen and K.P. de Jong
Netherlands' Catalysis and Chemistry Conferences
Noordwijkerhout, the Netherlands, March 2007

**Poster presentations**

*Fundamental Studies on Catalyst Preparation using Ordered Mesoporous Silica as a Model Support*
J.R.A. Sietsma, P.E. de Jongh, A.J. van Dillen and K.P. de Jong
Catalytic Processes on Advanced Micro- and Mesoporous Materials Symposium
Nessebar, Bulgaria, September 2005

*Ordered Mesoporous Model Supports as a Tool to Study Catalyst Preparation*
J.R.A. Sietsma, P.E. de Jongh, A.J. van Dillen and K.P. de Jong
Netherlands' Catalysis and Chemistry Conference
Noordwijkerhout, the Netherlands, March 2006

*Ordered Mesoporous Model Supports as a Tool to Study Catalyst Preparation*
J.R.A. Sietsma, P.E. de Jongh, A.J. van Dillen and K.P. de Jong
11th Roermond Conference on Catalysis
Kerkrade, the Netherlands, June 2006

*Ordered Mesoporous Model Supports as a Tool to Study Catalyst Preparation*
J.R.A. Sietsma, P.E. de Jongh, A.J. van Dillen and K.P. de Jong
5th Tokyo Conference on Advanced Catalytic Science and Technology
Tokyo, Japan, July 2006

*A Novel Calcination Method to obtain Highly Active FT Catalysts from a Cobalt Nitrate Precursor*
J.R.A. Sietsma, J.P. den Breejen, P.E. de Jongh, A.J. van Dillen, J.H. Bitter and K.P. de Jong
8th Natural Gas Conversion Symposium
Natal, Brasil, May 2007

# Dankwoord

Het laatste stuk dat ik zal schrijven voor het proefschrift is dit dankwoord. Het AIO-schap zit er nu dan toch echt bijna op. Een periode die voorbij is gevlogen en waar ik met veel plezier op terugkijk. Ik wil dan ook iedereen bedanken die daar aan bijgedragen heeft, en vanaf deze plaats een aantal personen in het bijzonder aanspreken.

Krijn, ik wil je bedanken voor de mogelijkheid die je mij gegeven hebt om in jouw groep te promoveren. Door je enthousiasme, hartelijkheid en het gegeven dat je vrijwel altijd even tijd had om over de laatste resultaten te discussiëren heb ik de samenwerking met je als zeer prettig ervaren. Daarnaast heb ik de grote vrijheid die je mij binnen het onderzoek gaf zeer gewaardeerd evenals de snelheid waarmee je de hoofdstukken en papers bestudeerde. Ik heb de afgelopen vier jaar veel van je geleerd, waarvoor mijn dank.

Jos, hoewel je uiteindelijk niet als co-promotor op de keerzijde van het titelblad terechtgekomen bent heb je een essentiële rol tijdens mijn promotie gespeeld. Helaas zat het je, nadat je met vervroegd pensioen ging, niet mee en kon je vanwege ziekte lange tijd niet echt meer betrokken zijn bij het onderzoek. Ik heb altijd erg genoten van de discussies die we over het onderzoek hadden en je kennis, inzichten en ideeën zijn vaak van groot belang gebleken. Mijn dank hiervoor.

Petra, wat begon met 'vrijblijvende' gesprekken over de synthese van geordend mesoporeuze materialen draaide uit op een co-promotorschap voor jou. Mede vanwege je wetenschappelijke nieuwsgierigheid, enthousiasme en kritische blik heb ik het leuk gevonden met je samen te werken, hoewel het aantal ideeën waarmee ik met regelmaat bij je wegliep na een bespreking soms frustrerend hoog was aangezien een promotie maar vier jaar duurt... Ik wil je bedanken voor de samenwerking en de snelheid en veelal nauwkeurigheid waarmee je door mijn manuscripten stoof.

Tijdens de promotie heb ik een aantal studenten mogen begeleiden. Timmo, bedankt voor je scriptie over SBA-15. Mariska, jij hielp mij tijdens je bachelor met het verkennen van het belang van de experimentele condities tijdens de synthese van SBA-15. Ik vind het leuk dat jij nu het stokje van mij overgenomen hebt en verder gaat met het ontrafelen van de nitraat-chemie. Veel succes met je promotie en ik kijk uit naar je (toekomstige) bevindingen! Hoofdvakstudent Christian, bedankt voor je inzet en ik wens je veel succes met je carrière.

Chia-Min Yang from the Max-Planck Institute in Müllheim is thanked for his time and effort to explain to me some of the ins and outs of the SBA-15 synthesis.

I thank Johnson Matthey Catalysts for their sincere interest in the research that I carried out during my PhD-research and their support. John Casci, Martin Lok, Barbara Iacono and Bart Zwijnenburg are thanked for their valuable discussions and

assistance with experiments. I really enjoyed the meetings, and visits in Billingham and Emmerich. I also want to thank Johan Ridland for his fast and precise writing of the patent applications. Rudolf Mollema, Els Verdonck and Daniel Roedolf van TA Instruments wil ik bedanken voor de hulp bij de calorimetrie metingen. Herre Talsma en Mies van Steenbergen van farmaceutische wetenschappen wil ik bedanken voor het beschikbaar stellen van de apparatuur hiervoor.

Heiner, I really enjoyed looking at the electron tomography results that you generated of some of my NiO/SBA-15 samples. I thank you for our fruitful collaboration on putting together a quantitative model and I enjoyed the discussions that we had during interpretation of the ET results. I wish you best of luck in finishing your thesis. Johan, jou dank ik voor je hulp bij het katalytische testen van kobalt katalysatoren zoals beschreven in hoofdstuk 6 en ik heb onze samenwerking als erg plezierig ervaren. Ik wens je veel succes met je onderzoek. Dear Nilesh, the research that we conducted together was not only interesting since we tried to combine some of the best of the homogeneous and heterogeneous worlds, but also much fun to me. I have learnt much from your 'homogeneous-perspective' and I am happy that our friendship has continued.

Tijdens mijn promotie heb ik assistentie gekregen van o.a. de technische staf die mij hielpen om de in dit proefschrift beschreven resultaten te verkrijgen. Hans, hoeveel uur je wel niet met mij achter de TEM gezeten hebt weet ik niet, maar veel zijn het er in ieder geval wel! Je betrokkenheid, gezelligheid en welwillendheid om zelfs om half acht 's ochtends al te beginnen heb ik zeer gewaardeerd en ik ben je hier dan ook zeer erkentelijk voor. Prof. Geus, ook met u heb ik veel achter de TEM gezeten. Ik heb de gesprekken met u altijd erg interessant gevonden en dank u voor uw hulp en interesse in het onderzoek. Ad$^{M}$ wil ik bedanken voor zijn prettige samenwerking. In het bijzonder op het gebied van $N_2$-fysisorptie was je hulp om de apparatuur werkend te krijgen/houden onontbeerlijk voor mij. Marjan wil ik bedanken voor haar hulp met SEM en *in situ* XRD analyse. Het samen met je langsgaan bij fabrikanten opzoek naar een nieuwe XRD was leerzaam, gezellig en is eveneens uiterst zinvol gebleken voor mijn onderzoek (zie hoofdstuk 3 en 5). Verder wil ik Vincent (TPR), Fred (TGA/MS), de glasblazerij en natuurlijk Dymph en Monique van het secretariaat bedanken voor hun assistentie.

Dan natuurlijk een woord voor mijn kamergenoten, Kees en Alwies met wie ik drie jaar in werkkast N213 heb gezeten. Ik heb onze diepgaande discussies over actualiteiten uit de Eykelbergh, muziek en politiek altijd een erg mooie afwisseling gevonden van de science. Alwies, ik zal je smartlappen-muziek en Vitamine F geur niet echt gaan missen, maar wel als kamergenoot. Ik wens je veel succes met jouw laatste loodjes. Kees, alsnog bedankt voor je mooie kaart uit Berlijn! Ik zal ook jou als kamergenoot op 'de zaak' gaan missen. Ik vind het leuk dat je mijn paranimf wilt zijn en wens je succes met het afronden van je alanaten-werk. Verder wil ik alle (oud) AIO's en andere collega's bedanken voor de gezelligheid tijdens de voetbal toernooien, BBQs, LIIT's, kerstdiners, vakgroepsuitjes en borrels.

Tenslotte wil ik een aantal mensen bedanken die niet direct betrokken waren bij het onderzoek, maar wel belangrijk voor mij waren de afgelopen jaren. Chris, we kennen elkaar inmiddels al heel wat jaren en de vele avondjes Battlefielden of gewoon een filmpje kijken waren een gezellige afwisseling. Ik vind het leuk dat je 24 september naast mij staat. Natuurlijk wil ik ook de (oud)-atleten noemen waarmee ik altijd zoveel plezier heb gehad tijdens het hardlopen en wielrennen. Ralph, hoewel je een tijd als sprinter door het leven ging heb je op tijd ingezien dat duursporten toch veel mooier is. Ik zal onze vele beulsritten door de Alpen, Ardennen en de Veluwe niet snel vergeten. Vooral het colaatje boven op de Alpe na het finishen van La Marmotte staat mij nog helder voor de geest! Dolf, ook wij hebben samen veel kilometers gemaakt op de fiets. Ik heb genoten van onze fiets-vakanties bij de Mont Ventoux, in de dolomieten en in de Alpen. Binnenkort maar weer eens kop-over-kop de flevopolder door? Arnoud en Rob, het gezamenlijk hardlopen is al even niet meer, maar dat maakt het er niet minder gezellig op! Dank ook aan Linda, Ronald, Dorien, Susanne, Rik en Marijn voor de gezellige feesten en (ski)-vakanties de afgelopen jaren. Ook wil ik mijn naaste familie bedanken. Mijn broer en zus, Alies, Jan Erik en nichtje Donner, Ben en Ineke en natuurlijk mijn ouders die mij de steun gegeven hebben om mij volledig te kunnen ontplooien.

De laatste woorden zijn voor jou Laurien, mijn levensgezel. Je liefde, steun en begrip betekende veel voor mij. Hopelijk mogen we met elkaar nog lang van het leven genieten!

*Jelle*

# Curriculum Vitae

Jelle Sietsma werd geboren op 14 juni 1978 te Laren. In 1996 behaalde hij het HAVO-diploma aan het Sprengeloo te Apeldoorn en ging in datzelfde jaar Analytische Chemie studeren aan de Saxion Hogeschool in Deventer. Na deze studie in 2000 afgerond te hebben startte hij in hetzelfde jaar met de studie Scheikunde aan de Universiteit Utrecht. Februari 2003 studeerde hij met genoegen af bij de sectie Anorganische Chemie en Katalyse (Dr. M. Tromp en Prof. Dr. Ir. D.C. Koningsberger). Vanaf april 2003 was hij werkzaam als assistent in opleiding in de sectie Anorganische Chemie en Katalyse van de Universiteit Utrecht. Het promotieonderzoek werd uitgevoerd onder supervisie van Prof. Dr. Ir. K.P. de Jong, Dr. A.J. van Dillen en Dr. P.E. de Jongh. De resultaten van het onderzoek zijn beschreven in dit proefschrift en werden eveneens gepresenteerd op diverse internationale congressen. Tijdens het 8e Netherlands' Catalysis and Chemistry Conference (NCCC) in maart 2007 ontving de schrijver van dit proefschrift de NRSCC prijs voor de beste lezing door een promovendus. Vanaf 1 oktober 2007 zal hij werkzaam zijn als onderzoeker bij Shell Global Solutions te Amsterdam.

*Jelle Sietsma was born on the 14th of June 1978 in Laren. In 1996 he received his diploma of the secondary school Sprengeloo in Apeldoorn and started in the same year with an Analytical Chemistry study at the Saxion College of Technology in Deventer. After finishing the study in 2000, he started in the same year with his Chemistry study at Utrecht University. February 2003 he obtained his master's degree with credit and a specialisation in Inorganic Chemistry and Catalysis (Dr. M. Tromp and Prof. Dr. Ir. D.C. Koningsberger). Since april 2003 he worked as a PhD-student under supervision of Prof. Dr. Ir. K.P. de Jong, Dr. A.J. van Dillen and Dr. P.E. de Jongh in the Inorganic Chemistry and Catalysis group at Utrecht University. The research obtained during this period are described in this thesis and were presented during several international congresses. During the 8th Netherlands' Catalysis and Chemistry Conference (NCCC) in maart 2007 he received the NRSCC prize for the best presentation by a PhD-student. Starting 1st of October 2007, he will work as a research scientist at Shell Global Solutions in Amsterdam.*